THE UNIVERSITY *of* EDINBURGH

The Effect of Guest Uptake and High Pressure on Zn- and Zr-Metal-Organic Frameworks

Claire L. Hobday

A thesis submitted in fulfilment of the requirements for the degree of

Doctor of Philosophy to the School of Chemistry,

University of Edinburgh

2016

Declaration

I declare that this Thesis has been written by me and that the work carried out is my own, or I have made a substantial contribution towards it except where specific reference is made to another. This work has not been submitted for another degree or professional qualification.

Abstract

Porous materials are essential to our everyday lives, for example as an effective catalyst in the cracking of crude oil, or as water softeners in washing powder. When developing novel functional porous materials, it is necessary to fully understand their structure-property relationships to maximise their ability to be used in industrially relevant settings. This thesis aims to understand the mechanical and adsorption properties of a class of porous solids metal-organic frameworks (or MOFs), which have many potential applications owing to their tuneable structures. Due to the inherent 3-D crystalline structure of MOFs, a wide range crystallographic techniques were used to determine structure-property relationships. To achieve maximum in-depth structural knowledge, both classical and quantum theoretical approaches were also applied to complement the understanding of both the energetics and structural details.

Chapters One and Two begin with an overview of the state of the art studies carried out on MOFs, focusing on the use of high-pressure crystallography to understand their properties. In addition, there is emphasise on the importance of complementary computational methods that are used in the characterisation of MOFs.

In Chapter Three, an isostructural series of MOFs (zeolitic imidazolate frameworks, or ZIFs) were studied for methanol adsorption by employing both experimental and molecular simulation techniques. These frameworks are gating materials, where the imidazole linker rotates upon adsorption of guest, and it was found that through ligand substitution the gate opening

angle and onset pressure to gating could be tuned. By using high-pressure X-ray crystallography the structure of the ZIFs were studied upon the uptake of guest and the degree of ring rotation quantified. In combination with periodic DFT and grand canonical Monte Carlo simulations the energy barrier to rotation and energies of adsorption could be calculated, respectively.

Chapter Four focuses on one ZIF in particular, ZIF-8 ($(Zn_6(MeIm)_{12}$, MeIm = 2-methylimidazole) and details the adsorption of a selection of gases into the pores. The experimental method of cryogenic gas loading into a diamond anvil cell in this chapter is novel to MOFs. This method, in combination with molecular crystallography, is used to determine the structural response of the framework to guest-uptake as well as the crystallographic positions of the adsorption sites. In combination with *in silico* methods, the adsorption energies of guest-sites could be calculated, detailing which interactions drive the gating behaviour. The method of cryogenic loading highlighted how extreme conditions can be used to extract useful information about structural behaviour of MOFs on uptake of gas molecules into the pores, and when used in combination with computational methods, we have a powerful tool to analyse both positions and energies of adsorption sites. With this information, progress can be made in developing MOFs to maximize favourable interactions and lead to the development of MOFs with better selective gas storage properties.

Chapter Five focuses on the synthesis and characterisation of the physical properties of a series of Zr-containing MOFs, called UiO-MOFs. The high valency of Zr(IV) and 12-fold coordination of the metal cluster in these

materials, are associated with high shear and bulk moduli, which surpass those of other MOFs. A combination of single-crystal nano-indentation, high-pressure X-ray diffraction studies, density functional theory (DFT) calculations, and first-principles molecular dynamics (MD) simulations were used to determine the compressibility, elasticity and hardness of these materials, whose mechanical robustness was correlated to their different structural features, in-particular, how using non-linear linkers between the metal clusters stabilises the framework to compression.

Chapter Six expands upon the series of Zr-MOFs in Chapter Five, and looks at how the mechanical properties of these MOFs are affected upon increasing the linker length. The experimentally determined elastics modulus of one of the frameworks, UiO-sdc ($Zr_6O_4(OH)_4(sdc)_6$ where sdc =4,4'-stillbene dicarboxylate), was found to lie above those of other highly porous MOFs. In addition, the elastic modulus was found to decrease linearly as a function of increasing the linker length, extending the structure-property relationships determined in Chapter Five.

Dedication

For Thomas,

The quiet man.

Acknowledgments

This space is not long enough to thank everyone who helped me during the last three years in Edinburgh, but I'll try anyway. Of course, I must begin with three supervisors who I've enjoyed so much working with and have shaped me into the researcher I am today. Firstly, Stephen, you are best supervisor anyone could ask for. Thank you for all your support over the years. I really have learned a lot from you, and for that I am grateful. Thank you for sending me all over the world – to Canada, France, Germany & the USA– sorry for blowing your travel budget…

To Carole, thank you for being so patient throughout my PhD, when I come knocking on the door with silly questions. I am very grateful for all the time you have spent teaching me all the ins and outs of quantum chemistry. And of course, to Tina. Thank you for all your engineering expertise, discussions and tolerance in teaching me *via* Skype. Thank you for your open door during my visit to Bath, I feel the time I spent there strengthened this thesis. I look forward to many more fruitful discussions and collaborations.

Furthermore, I would like to thank Simon. I appreciate all the time and effort you spent teaching me crystallographic theory. To Chris, for being so very patient and helping me with many experiments and writing. To Alex, thank you for being my first synchrotron night-shift buddy.

To the lads in the office, Scott, Jorge, Andy, Jack & Charlie, thank you all for your warm welcome and great company, and to Gary for many interesting conversations over lunch or le café, as well as crystallographic help. To the new guys that joined: Nico, Jacob, Jonny and Matt, thank you.

To my great collaborators Tom, Big Ross, Wee Ross, Matt & F-X, thank you for all your expertise and vision. To my first project student Mark, and those that

followed: Becky, Jurgita, Emily, Steph, Angela, Sam, Hannah & Ryte, thank you. To Alan and Michael for being so supportive and encouraging me to take the path of research.

To all my friends here in KB, especially to the Larnold and Brechins groups and in particular to Priy, Markéta, Joy, Jamie, James, Mary, Helen, Emily, Fern, thank you.

To my family, Mum, Dad, Alex, Gran & of course, Granda. Thank you for all your support and although you might not fully understand what I've been up to, thanks for being so supportive. Last, but certainly not least to Max, my partner in crime. Thank you for your encouragement and support over the last wee while, you have made this thesis possible.

List of publications

"A computational and experimental approach linking disorder, high-pressure behavior, and mechanical properties in UiO frameworks "Hobday, C. L.; Marshall, R. J.; Murphie, C. F.; Sotelo, J.; Richards, T.; Allan, D. R.; Duren, T.; Coudert, F.-X.; Forgan, R. S.; Morrison, C. A.; Moggach, S. A.; Bennett, T. D., *Angew. Chem. Int. Ed.* 2016, **55** (7), 2401.

"Amino acids as highly efficient modulators for single crystals of zirconium and hafnium metal-organic frameworks" Marshall, R. J.; Richards, T.; Hobday, C. L.; Murphie, C. F.; Wilson, C.; Moggach, S. A.; Bennett, T. D.; Forgan, R. S., *Dalton Trans.* 2016, **45** (10), 4132.

"Postsynthetic bromination of UiO-66 analogues: altering linker flexibility and mechanical compliance" Marshall, R. J.; Hobday, C. L.; Murphie, C. F.; Griffin, S. L.; Morrison, C. A.; Moggach, S. A.; Forgan, R. S., *J. Mater. Chem. A.* 2016, **4**, 6955.

"Hidden negative linear compressibility in lithium l-tartrate" Yeung, H. H.-M.; Kilmurray, R.; Hobday, C. L.; McKellar, S. C.; Cheetham, A. K.; Allan, D. A.; Moggach, S. A., *Phys. Chem. Chem. Phys.* 2017, **19** (5), 3544.

""Ag(i) bipyridyl coordination polymers containing functional anions" Dodds, C. A.; Hobday, C. L.; Kennedy, A. R.; McKellar, S. C.; Smillie, K.; Walls, A., *New J. Chem.* 2017, **41** (4), 1574.

List of Abbreviations

abdc	4,4′-azobenzenedicarboxylate
AIMD	*Ab initio* molecular dynamics
AP	Ambient-pressure
bddb	4,4′-(buta-1,3-diyne-1,4-diyl)dibenzoate
BFGS	Broyden-Fletcher-Goldfarb-Shanno
BLYP	Becke-Lee-Yang- Parr
bpdc	biphenyldicarboxylate
CCD	Charged-coupled device
CSD	Cambridge structural database
DAC	Diamond anvil cell
DMF	dimethylformamide
DFT	Density functional theory
E	Elastic or Young's Modulus
edb	4,4′-ethynylenedibenzoate
EoS	Equation of state
GCMC	Grand canonical Monte Carlo
G_{min}	Shear modulus
H	Hardness
HKUST	Hong Kong University of Science and Technology
HP	High-pressure
HYPO	Hypothetical
ICA	Imidazole-2-carboxaldehyde
K	Bulk modulus
LJ	Lennard Jones
MeIm	2-methyl imidazole
MIL	Matériaux de l'Institut Lavoisier
MOF	Metal-organic framework
NO_2Im	2-nitro imidazole
PBE	Perdew-Burke-Ernzerhof
PTM	Pressure transmitting medium

SAV	Solvent accessible volume
SCF	Self-consistent field
sdc	4,4'-stillbene dicarboxylate
UiO	University of Oslo
ZIF	Zeolitic imidazolate framework

Table of Contents

-Chapter One-
Introduction

1.1 Metal-organic frameworks

For the past twenty years, metal-organic frameworks (MOFs) have sparked the interest of many researchers from varying areas of science. Combining supramolecular chemistry, crystallography, computational chemistry, mechanical and chemical engineering, materials science and many more disciplines, the science of MOFs has become an exciting and diverse area of research. The sheer volume of work on MOFs can be characterised by the number of research papers produced, with over a thousand per year (or more impressively at a rate of five MOF papers per day). Additionally, there are over 75,000 MOF structures in the Cambridge Structural Database (CSD, November 2016), representing a staggering 6% of the entire CSD.[2, 3] MOFs attract so much attention from different research backgrounds due to the broad range of structures that can be synthesised, leading to tuneable functional materials for a variety of industrial applications. These applications include, but are not limited to, gas storage, gas separation, piezoelectric devices, proton conductors, sensing and catalytic processes.[4-8]

Due to the wide-ranging efforts by researchers in the field of MOF chemistry, many potential definitions for MOFs have been suggested. Cheetham *et al.* have defined them as a subgroup of the family of solid materials known as *hybrid inorganic organic frameworks*, whereas other groups prefer the name *coordination polymer* or even *nanoporous hybrid frameworks*.[10] To simplify the terminology of the field, IUPAC set up a task group to recommend a unified definition for MOFs.[11] In this review, a *coordination polymer* was defined as "a coordination compound with repeating coordination entities extending in one, two or three dimensions" and the subgroup of *coordination network* as "a

coordination compound extending, through repeating entities in one dimension but with cross-links between two or more individual chains, loops or spiro-links, or a coordination compound extending through repeating coordination entities in two or three dimensions". These recommendations led to *metal-organic frameworks* (MOFs) being defined as "a coordination network with organic ligands containing potential voids".[11]

More generally, MOFs are compounds which contain metal nodes (usually metal ions or clusters) connected by organic struts to form framework architectures which tend to be porous and crystalline. Such examples include the archetypal MOF-5 ($[Zn_4(\mu4\text{-}O)(BDC)_3]$, BDC = benzene-1,4-dicarboxylate) and HKUST-1 ($[Cu_3(BTC)_2]$, BTC = benzene-1,3,5-tricarboxylate) where Zn and Cu clusters are connected by organic linkers to form 3-dimensional porous frameworks (**Figure 1.1**).[12, 13]

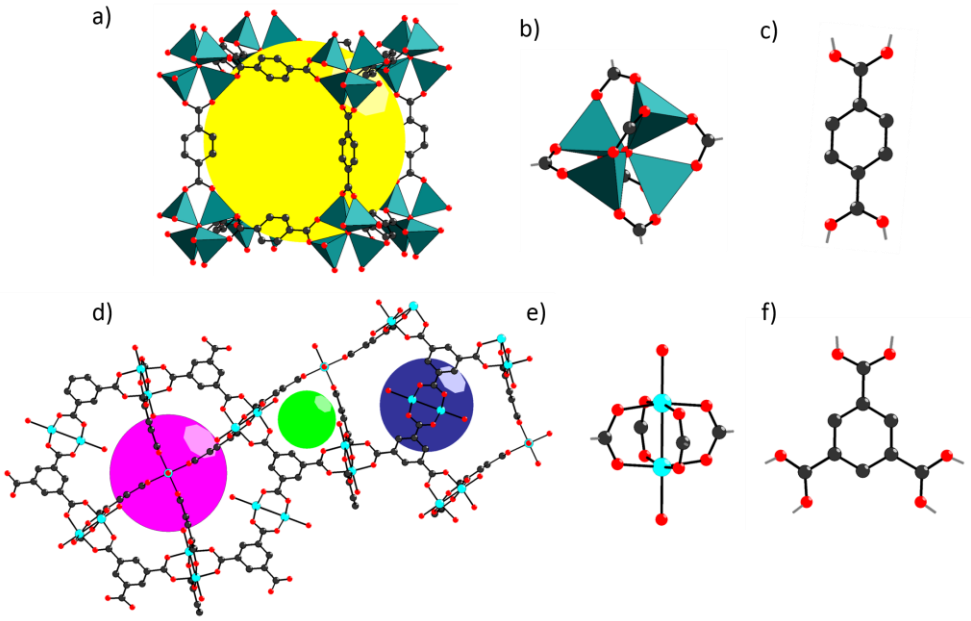

Figure 1.1: a) MOF-5, b) Zn_4O_{13} cluster, c) BDC linker, d) HKUST-1, e) Cu paddlewheel Cu_2O_{10}, f) BTC linker. ZnO_4 tetrahedra – teal, copper – light blue, oxygen – red, carbon – black. H atoms are omitted for clarity. Yellow, magenta, green and indigo spheres in (a) and (d) represent the different types of pores present in the HKUST-1 and MOF-5 frameworks.

MOF-5 is also known as IRMOF-1, where IR stands for isoreticular. Isoreticular chemistry is an approach used to tune the functionality and size of the framework pores in a systematic way, in doing so vast libraries of frameworks can be created. In 2002, Eddaoudi and co-workers pioneered this area of isoreticular MOF research with the IRMOF family, where all frameworks were based on the Zn_4(μ4-O) cluster with the same framework topology, however, the BDC linker was replaced by a number of ligands. These were altered by either functionalising the BDC, for example with–Br, -NH_2, or -OC_3H_7 (IRMOF-2 through -4), or by replacing BDC with longer units such as, tetrahydropyrenedicarboxylate, pyrenedicarboxylate or, perphenyldicarboxylate (IRMOF-9 through -11).[14] These modifications can fundamentally change the properties of the frameworks. The introduction of

amino functionalities, for example, has been shown to increase CO_2 capturing capabilities, while the addition of electronegative groups has been shown to increase the mechanical resistance of the framework. In addition, the pore size and shape of the MOFs can be controlled.[15, 16] Today, this isoreticular approach to synthesising new MOFs is commonplace, with many families of MOFs now expanded using this approach. Two ground-breaking examples include the Universitat of Oslo (UiO) MOFs based on $Zr_6O_4(OH)_4$ clusters linked with a series of dicarboxylate ligands, and the Matériaux de l'Institut Lavoisier structures (MILs) based on tri-valent metal nodes such as V(III), Cr(III) or Fe(III), linked with dicarboxylic ligands.[17-19]

With such libraries of novel MOF materials, there is now a plethora of books and reviews highlighting the potential applications of MOFs, including catalysis, sensing, biomimicry, separation and storage.[20-23] Despite the promising prospects of MOFs, there are still many challenges that need addressing. Poor chemical and mechanical stability is one of the biggest practical problems associated with MOFs, especially when compared to zeolites which have been well established in industrial processes such as molecular sieving, catalysis and ion-exchange. Zeolites, are porous aluminium silicates which have high degradation temperatures, are resistant to high pressures, non-soluble and are resistant to oxidation, making them ideal for industrial processes.[24] If MOFs could be optimised to have similar stabilities and retain their breadth of functionalities, then they could surpass the use of zeolites in industry. Recently, the first commercialisation of a MOF has been brought to fruition in the food industry. The MOF slowly releases 1-methylcyclopropene onto harvested fruit and vegetables preventing the fruit from producing ethylene which causes the food to ripen and decompose

quickly.[25] This represents a huge step forward for the field, and is promising for other industrial uses of MOFs.

One such functionality that certain MOFs possess, which previous porous materials such as zeolites could not achieve, is a degree of flexibility. MOFs of this flexible nature have been named "soft porous crystals".[26] These are materials which can undergo significant structural changes when exposed to varying temperatures, pressures and upon the uptake of guest molecules inside the pores. This usually results in an expansion or contraction in volume (sometimes of over 100 %) and negative linear compressibility.[27-33] Negative linear compressibility is defined as when the total volume of a material decreases under hydrostatic compression, however, one cell axis (or two, to give negative area compressibility) actually expand. This phenomenon was first thought be rare, however, it is more widespread than first thought in MOFs.[34]

In this thesis, in order to better understand structure-property relationships in MOFs, and how the components of the MOF affect both the mechanical and adsorption properties, several techniques have been used, including nanoindentation, computational studies (including first principles and classical simulations) and diffraction. The majority of MOFs are inherently crystalline, as a result of the highly ordered repeating 3-D lattice, making X-ray and neutron diffraction the main characterisation technique in determining the structure of MOFs. One area of increasing growth, is *in situ* diffraction methods, where MOFs are investigated under direct compression or at varying pressures and on uptake of guest molecules whilst

simultaneously collecting X-ray or neutron diffraction data. From these *in situ* measurements, direct observation of structural changes of MOFs in these environments gives insight into the mechanical properties and adsorption mechanisms.

This thesis aims to explore the mechanical and adsorption behaviour in MOFs by utilising both experimental and computational techniques. The first half of this thesis concerns the adsorption of liquids and gases into MOFs, using high-pressure crystallography, density functional theory and classical molecular simulation to provide an in-depth analysis of the adsorption process. The second half of this thesis concerns the mechanical properties and response of MOFs, through techniques such as high-pressure X-ray diffraction, nanoindentation and *ab initio* molecular dynamics. Chapter Two provides more details on all experimental and computational techniques used.

1.2 MOFs under pressure

Non-ambient crystallography is a well-established field, allowing insight into the influence of temperature or pressure on crystalline materials. The field began in the 1930s, only three decades after the pioneering work on the discovery of X-ray crystallography as a technique to understand the structure of crystalline materials by Max von Laue and the Braggs. There have been major advances in both X-ray sources, detectors, low temperature and high pressure equipment over the last 80 years. Over the last 20 years, there have been numerous studies of MOFs at varying temperatures and pressures, including gas sorption and high-pressure crystallographic studies.[35, 36] This introduction will encompass a brief review of some of the well-studied MOFs at high-pressure (in excess of 1000 atm), and how theoretical calculations can

be used in concert, to fully understand the properties of framework materials, in particular, focussing on MOF-5 (IRMOF-1), HKUST-1 (CuBTC), STAM-1 and MIL-53(Fe).

1.2.1 MOF-5

First synthesised by Yaghi *et al.* in 1999, MOF-5 is composed of $[Zn_4(\mu_4\text{-}O)]^{6+}$ units linked by BDC ligands to yield a high symmetry cubic framework (space group $Fm\bar{3}m$).[12] The window diameter measures ~ 7.6 Å in size and the pore diameter (the largest sphere that can be placed in the pore, without overlapping the van der Waals radii of the framework atoms) is 12 Å (**Figure 1.1a**). As one of the pioneering frameworks of MOF chemistry, it has been one of the most studied, due to the fact it was one of the first MOFs to retain permanent porosity in the absence of guest molecules, a significant barrier that was overcome in the development of MOFs for application. Upon desolvation, the density of MOF-5 is 0.59 g cm^{-1}, an exceptionally low value for a MOF at that time, and the material has been intensely studied for gas sorption properties. *In situ* single-crystal and powder X-ray and neutron diffraction experiments have been performed under atmospheres of H_2, D_2, N_2, Ar and CD_4.[37-41] These studies revealed that the adsorption was a multi-layer process, with up to eight symmetry independent adsorption sites, split into five sites in close interaction to the framework and three sites forming a secondary layer. Temperature control in these studies gave insight into the order of preferential adsorption sites. In the case of N_2 and Ar, at room temperature (293 K) only diffuse electron density could be located in the pores, and upon cooling to 30 K (below the freezing point of both gases) the adsorption sites and occupancies could be clearly located, with the most populated sites located at the metal centres, and less preferential sites were observed along the edge of the

aromatic ring on the BDC ligand.[41] This highlights one of the difficulties with *in-situ* methods at atmospheric pressures and elevated temperatures; although the situation is more comparable to the temperature at which separation and storage applications take place, decreased uptake is observed crystallographically. To overcome this problem, higher pressures of gases can be used to observe adsorption sites.

Diamond anvil cells (DACs) have allowed high-pressure crystallography to be carried out on MOF-5 at more extreme pressures (up to 3.25 GPa, 32,500 times atmospheric pressure).[1] Using diethylformamide (DEF) as a pressure transmitting medium (PTM) for MOF-5 within the DAC (more details on the methodology for high-pressure crystallography can be found in **Chapter Two**), Graham *et al.* highlighted that the PTM could penetrate into the crystal and explained how the structure responded to the uptake of DEF in the pores and in fact the inclusion of DEF in MOF-5 stabilised the framework to compression. Hu *et al.* carried out pressure induced amorphisation experiments of MOF-5 by means of a round anvil press, which created non-hydrostatic conditions and the framework amorphised at 0.0035 GPa (35 bar).[42] This demonstrates that inclusion of guests in the framework in a hydrostatic environment stabilised the framework from amorphisation by a factor of 1000 over non-hydrostatic conditions.

To further understand how pore-filling affects the compression of MOF-5, Graham *et al.* employed solid state DFT to simulate the direct compression of MOF-5 at increasing external hydrostatic pressures, without the influence of guest.[1] The comparison (**Figure 1.2**) highlighted that the DEF PTM could

penetrate the framework. When forced inside the pores, this causes an initial expansion of the unit cell at low pressures (0.08 GPa), and is followed by a gradual compression of the unit cell. In contrast, the *ab initio* (labelled EVAC in **Figure 1.2**) compression study showed no expansion, and has a greater compressibility, demonstrating how pore-filling of these porous materials can alter their compressibilities.

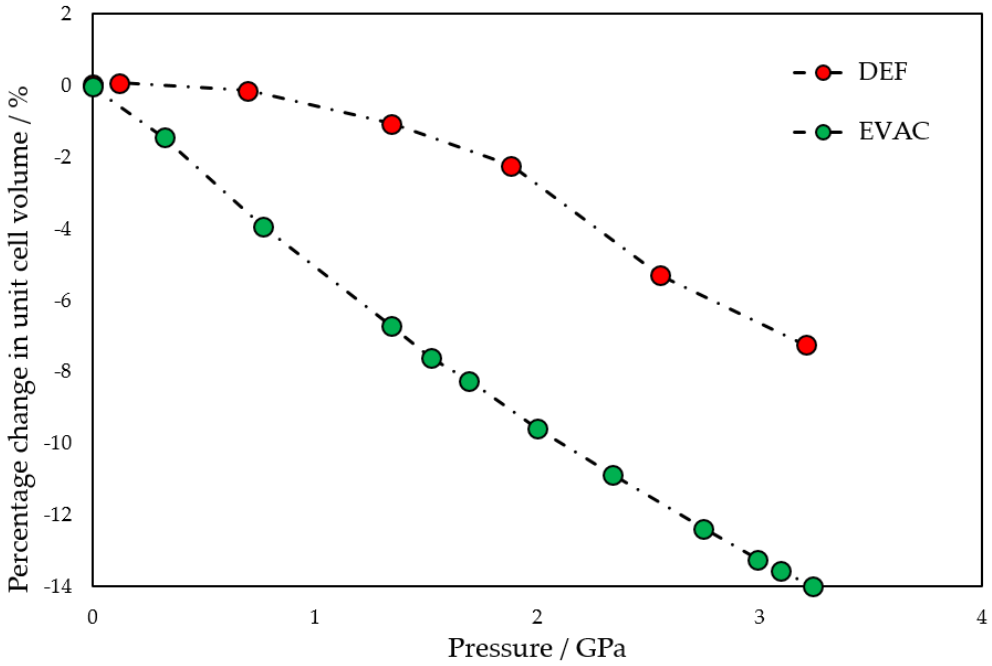

Figure 1.2: Compressibility of MOF-5-DEF (red circles) and MOF-5-EVAC (green circles). Adapted from Graham et al.[1]

1.2.2 HKUST-1

HKUST-1 (also known as Cu-BTC) (**Figure 1.1d**) has also been the subject of many *in-situ* adsorption experiments from as early as 2006, with neutron powder diffraction (NPD) studies with D_2 gas. Here interestingly, Peterson *et al.* were able to show that upon increasing the loading of the gas, the refined

occupancies of the symmetry independent sites increased, demonstrating a progressive filling of the adsorption sites. This study was followed over the next decade with CD_4, CO_2, CO, Ar, Kr and Xe.[43-48] The labile axial water ligands of the Cu paddlewheel can be removed to create open metal sites in HKUST-1. Neutron diffraction studies on the different gases helped to elucidate the role that these open metal sites had upon the adsorption of different gases. Open metal sites were found to be important for the uptake of gases with strong electrostatics such as CO_2, whereas the noble gases tended not to interact with those open metal sites.[47, 48]

Like in the case of MOF-5, hydrostatic high-pressure experiments proved important in understanding the pore-filling mechanism of HKUST-1. High-pressure powder X-ray diffraction (PXRD) experiments were carried out by Chapman *et al*., and demonstrated for the first time (by using PTM of increasing size; methanol:ethanol:water (MEW), iso-propyl alcohol (IPA) and fluorinert FC-70 (a bulky, perfluorinated amine)) that the compressibility of the MOF was strongly dependent on the PTM.[49] In both MEW and IPA, there is a two-step compression with an initial "hard" regime, where the bulk modulus, *K*, measures ~118 GPa and a secondary "soft" regime where K ~ 30 GPa, occurring at 2.2 and 0.8 GPa for MEW and IPA, respectively. This transition was attributed to a change from hyperfilling to a pore emptying mechanism. In comparison, in the non-penetrating FC-70 media, direct compression occurred and the sample became amorphous at significantly lower pressures than with the penetrating media (**Figure 1.3**). The pressures at which HKUST-1 becomes amorphous is also dependent on the size of the PTM, where MEW allows the framework to retain its crystallinity until 7.5 GPa, IPA until 4.2 GPa and FC-70 until 2 GPa.

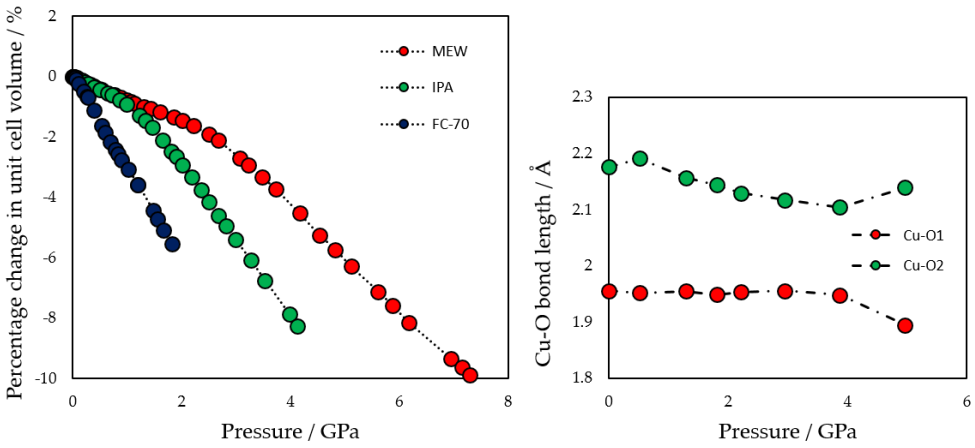

Figure 1.3: (Left) Compressibility of HKUST-1 in MEW (red circles), IPA (green circles) and FC-70 (dark blue circles). (Right) Cu-O1 (equatorial) and Cu-O2 (axial) bond lengths upon compression in MEW.[9]

Since the high-pressure PXRD study did not report any structural data, Graham *et al.* carried out a comparable single-crystal high-pressure X-ray diffraction experiment with MEW to clarify the exact nature of the structural transitions between the hard and soft regions.[9] In agreement with Chapman *et al.*, it was confirmed that the pores of HKUST-1 filled up until 3.9 GPa.[50] After 3.9 GPa, the electron density in the pores decreased which coupled with a change in the Cu-O bond lengths (**Figure 1.3**). Cu-O1 equatorial bonds decreased in length, while the axial Cu-O2 bonds elongated. This shows that the pore emptying mechanism was associated with compression of the equatorial Cu-O1 bonds, resulting in the reduction in volume during the pore emptying transition. It is worth mentioning that the difference in pressures of the transition seen in powder compared to single-crystal data could be

ascribed to particle size effects, something which is known to exist in framework materials, most notably in the adsorption properties of ZIF-8.[51]

1.2.3 STAM-1

Related to HKUST-1, STAM-1 $[Cu_3O_{21}C_{30}H_{24}]_n.5n(H_2O)$, is synthesised from the same starting materials of $Cu(NO_3)_2.3H_2O$ and benzene-1,3,5-tricarboxylic acid (H_3BTC).[52] Using ethanol as a solvent in hydrothermal conditions produced HKUST-1, however, if the solvent is exchanged for a 50:50 mixture of water:methanol, STAM-1 is produced. This is due to H_3BTC undergoing a selective monoesterification during synthesis and producing monomethyl-esterified BTC ligands linking five-coordinate Cu paddlewheels. These dimeric Cu tetracarboxylate units form four symmetry equivalent equatorial Cu-O bonds of ~1.96 Å and an axial Jahn-Teller distorted Cu-O bond of ~2.15 Å to a coordinated water molecule. This results in the framework forming interwoven layers of two types of channel: one lined by ester groups (hydrophobic) and the other lined by axial water molecules (hydrophilic), creating one hydrophobic and two hydrophilic pores per unit cell (**Figure 1.4**).

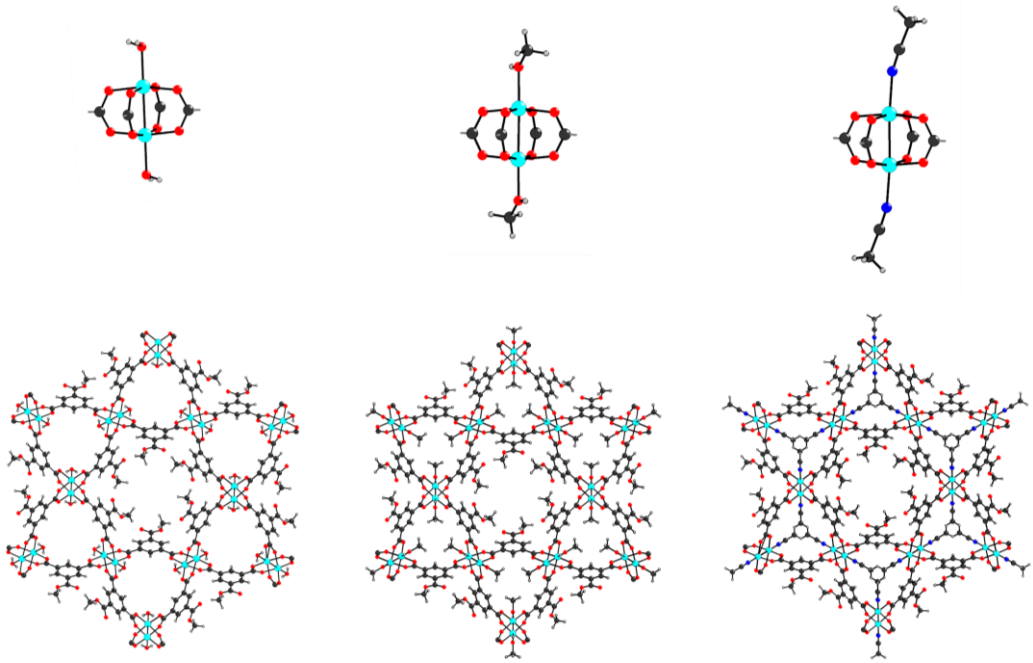

Figure 1.4: (Top) Paddlewheel units of STAM-1, STAM-1-MeOH, STAM-1-MeCN. (Bottom) STAM-1 with central hydrophobic pore surrounded by hydrophilic pores. STAM-1-MeOH, STAM-1-MeCN (shown with the three possible coordination sites of MeCN.

In situ single crystal experiments were carried out on STAM-1, in this case, looking at the lability of the water molecule located on the of axial Jahn-Teller axis, and through these experiments the first example of post-synthetic dative modification of a MOF at pressure was presented.[53] Post synthetic modification (PSM) in the MOF community is a field in its own right, and is the subject of numerous reviews.[54-56] By carrying out PSM on MOFs, synthesis of new MOFs (which are impossible to make via direct synthesis) is achievable, opening up new avenues of chemistry and potential applications for MOFs. Some examples include the single-crystal to single-crystal metalation of a chelating linker in a framework. For example UiO-67-bipy $[Zr_6O_4(OH)_4(bipy)_6]$ (bipy = 2,2-bipyridine-4,4'-dicarboxylate) was exposed to either vapours or

solutions of CuCl, $CuCl_2$, $CoCl_2$, $FeBr_2$ and $Cr(CO)_6$ to produce almost quantitative post synthetic metalation.[57] This idea of metalation was then further explored by Lin *et al.*, metalating UiO-67-bipy with $[Ir(COD)_2]BF_4$ (COD = 1,5-cyclooctadiene) with only 10% occupancy, however ,even at low levels of inclusion, the metal complex rendered the MOF an efficient and recyclable catalyst for borylations of a number of arene precursors.[58]

In the case of STAM-1, when soaked in methanol under ambient conditions, it undergoes a single-crystal transition where methanol exchanges with the axial H_2O ligand (referred to as STAM-1_{MeOH}).[53] This causes the once open hydrophilic channels to become isolated hydrophobic pores, due to the penetration of methyl groups into the channel (**Figure 1.4**). This result is quite interesting, considering that methanol is used as one of the original reaction solvents, suggesting that this PSM approach is the only route to producing the methanol-modified framework. McKellar *et al*. went on to explore many other transformations using high-pressure crystallography within a DAC on STAM-1, including methanol, isopropyl alcohol, ethanol, acetonitrile, and acetaldehyde as PTMs and found that there was a strict dependence on the molecular size of the solvent to undergo PSM. Using methanol, STAM-1 was stable to 5.7 GPa as methanol fills the small hydrophilic channel (and exchanges with the axial water molecule) as well as super filling the large hydrophobic channel. Using IPA, a larger alcohol, caused STAM-1 to be stable to 2.4 GPa, and ethanol caused the sample to turn polycrystalline upon immersion at 0.1 GPa. The authors hypothesise that the collapse of the single crystal is due to an analogous ligand exchange occurring, but due to the larger size, of ethanol compared to methanol, the exchange causes a strain-induced breakdown of the crystal. This was confirmed when acetonitrile (similar size

to ethanol) was used as PTM. No ligand exchange occurred at ambient conditions, however at 0.3 GPa the axial water exchanged with acetonitrile to yield STAM-1$_{MeCN}$ (**Figure 1.4**). However, the exchange was not complete as only one in three water molecules exchanged, this part-exchange caused little steric strain between adjacent ligands, and therefore the framework did not collapse. Given the variety of structural responses observed in STAM-1 with various solvents, this is a demonstration of how pressure is a useful tool to probe the susceptibility of certain types of framework to PSM and facilitate the discovery of new materials.

1.2.4 MILs

MILs (*Matériaux de l'Institut Lavoisier*) are a family of materials which have a wide range of topologies and functions. Some of the most interesting are what Kitagawa *et al*. named third-generation MOFs, or can also be termed as "soft porous crystals" *i.e*. those which show breathing and flexibility in a reversible fashion.[59] One central example is MIL-53 [M(OH)(BDC)], (M=Fe(III), Al(III), Cr(III), V(III), Ga(III), In(III), or Sc(III)) which can expand and contract due to hinge-like movement in the BDC linkers, working much like a compliant wine rack. MILs are the most studied subgroup in terms of their adsorption behaviour, which can be attributed to its increased thermal stability compared to other MOFs.[60] Many i*n-situ* diffraction studies have been performed on MIL-53 to fully understand the adsorption processes associated with gases such as CO_2, H_2, CH_4, as well as the separation of branched aromatic molecules such as xylenes.[61-66] In addition, the behaviour has been studied as a function of the metal cation.[18]

To understand the breathing behaviour of MIL-53(Sc) in CO_2, Chen *et al.*, carried out combined *ab initio* MD (AIMD) simulations and *in situ* high-pressure X-ray powder diffraction experiments.[62] This study demonstrated how MIL-53(Sc) transformed upon uptake of CO_2 at various temperatures and pressures. The simulations were able to accurately describe the closure of MIL-53(Sc) upon solvent removal through an intermediate phase. This involved the transformation of MIL-53(Sc)-DMF (where DMF = dimethylformamide) to the intermediate phase MIL-53(Sc)-cp followed by MIL-53(Sc)-vnp (where cp = closed pore and vnp =very narrow pore) at higher temperatures (**Figure 1.5**). This cp-vnp transition at increased temperatures caused a change in space group of *P*21/*c* to *C*2/*c*, showing that the simulations account for entropic as well as enthalpic effects.

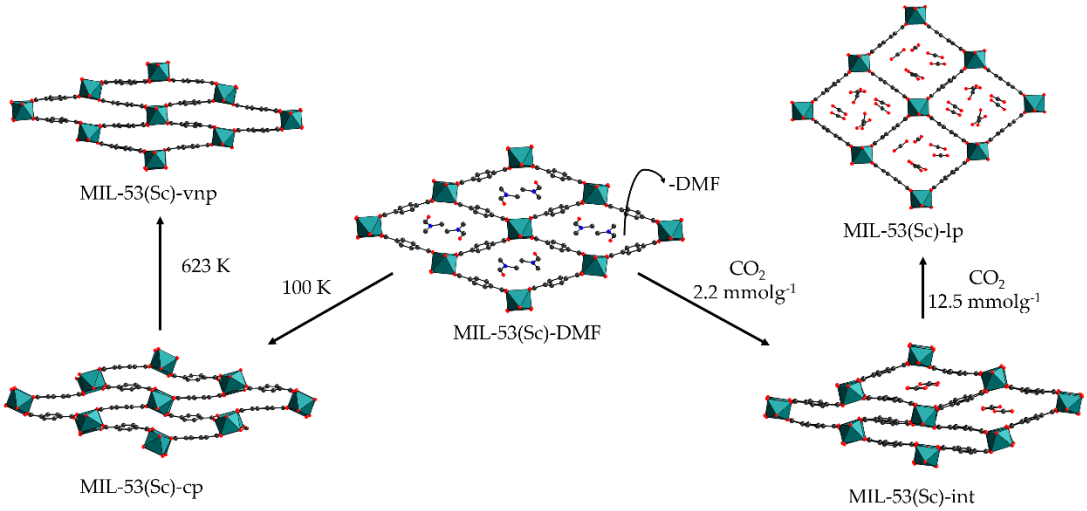

Figure 1.5: Breathing behaviour of MIL-53(Sc) upon evacuation of solvent and CO_2 loading.

In addition, AIMD was employed to mimic CO_2 adsorption of MIL-53(Sc) *in silico* by allowing the MIL-53(Sc) framework to evolve freely in response to CO_2 loadings corresponding to the two steps in the experimental adsorption isotherm. The resulting AIMD structures enabled the structure determination

of the two CO_2-containing intermediate and large-pore phases observed by experimental synchrotron X-ray diffraction studies with increasing CO_2 pressure. This would not have been possible, for the intermediate structure, *via* conventional methods because of diffraction peak broadening. These simulations illustrate the power of the AIMD method for the prediction and understanding of the behaviour of flexible microporous solids. In addition, when combined with experiment, a complete picture of how these flexible materials behave can be achieved.

1.3 Outline of Thesis

The combination of both experimental and theoretical methods is something which resonates throughout this thesis. This thesis aims to explore the mechanical and adsorption behaviour in MOFs by utilising both experimental and computational techniques. After a description of the methods used throughout this thesis, for example, classical or *ab initio* simulations in tandem with experimental methods, such as, non-ambient X-ray crystallography and nanoindentation in the following chapter, four chapters will comprehensively cover an understanding of the physical, mechanical and adsorption properties of certain families of MOFs.

1.4 References

1. A. J. Graham, D. R. Allan, A. Muszkiewicz, C. A. Morrison and S. A. Moggach, *Angew. Chem. Int. Ed.*, 2011, **50**, 11138-11141.
2. N. R. Champness, *Dalton Trans.*, 2011, **40**, 10311-10315.
3. C. F. Macrae, I. J. Bruno, J. A. Chisholm, P. R. Edgington, P. McCabe, E. Pidcock, L. Rodriguez-Monge, R. Taylor, J. van de Streek and P. A. Wood, *J. Appl. Crystallogr.*, 2008, **41**, 466-470.
4. S. Q. Ma and H. C. Zhou, *Chem. Commun.*, 2010, **46**, 44-53.
5. S. Tominaka, F. X. Coudert, T. D. Dao, T. Nagao and A. K. Cheetham, *J. Am. Chem. Soc.*, 2015, **137**, 6428-6431.
6. W. Wang, L. Q. Yan, J. Z. Cong, Y. L. Zhao, F. Wang, S. P. Shen, T. Zou, D. Zhang, S. G. Wang, X. F. Han and Y. Sun, *Sci. Rep.*, 2013, **3**, 1-5.
7. Z. C. Hu, B. J. Deibert and J. Li, *Chem. Soc. Rev.*, 2014, **43**, 5815-5840.
8. J. W. Liu, L. F. Chen, H. Cui, J. Y. Zhang, L. Zhang and C. Y. Su, *Chem. Soc. Rev.*, 2014, **43**, 6011-6061.
9. A. J. Graham, J. C. Tan, D. R. Allan and S. A. Moggach, *Chem. Commun.*, 2012, **48**, 1535-1537.
10. A. K. Cheetham, C. N. R. Rao and R. K. Feller, *Chem. Commun.*, 2006, 4780-4795.
11. S. R. Batten, Champness, N. R., Chen, X-M., Garcia-Martinez, J., Kitagawa, S., Ohrstrom, L., O'Keeffe, M., Suh, M. P., Reedilj, J., *Pure Appl. Chem.*, 2013, **85**, 1715-1724.
12. H. Li, M. Eddaoudi, M. O'Keeffe and O. M. Yaghi, *Nature*, 1999, **402**, 276-279.
13. S. S. Y. Chui, S. M. F. Lo, J. P. H. Charmant, A. G. Orpen and I. D. Williams, *Science*, 1999, **283**, 1148-1150.
14. M. Eddaoudi, J. Kim, N. Rosi, D. Vodak, J. Wachter, M. O'Keeffe and O. M. Yaghi, *Science*, 2002, **295**, 469-472.
15. X. R. Wang, H. Q. Li and X. J. Hou, *J. Phys. Chem. C*, 2012, **116**, 19814-19821.
16. B. Van de Voorde, I. Stassen, B. Bueken, F. Vermoortele, D. De Vos, R. Ameloot, J. C. Tan and T. D. Bennett, *J. Mater. Chem. A*, 2015, **3**, 1737-1742.
17. F. Millange, C. Serre and G. Ferey, *Chem. Commun.*, 2002, 822-823.
18. C. Serre, F. Millange, C. Thouvenot, M. Nogues, G. Marsolier, D. Louer and G. Ferey, *J. Am. Chem. Soc.*, 2002, **124**, 13519-13526.
19. J. H. Cavka, S. Jakobsen, U. Olsbye, N. Guillou, C. Lamberti, S. Bordiga and K. P. Lillerud, *J. Am. Chem. Soc.*, 2008, **130**, 13850-13851.
20. H. Furukawa, K. E. Cordova, M. O'Keeffe and O. M. Yaghi, *Science*, 2013, **341**, 974-986.
21. L. R. MacGillivray, *Metal-Organic Frameworks: Design and Application*, John Wiley & Sons, Inc., 2010.
22. H.-C. Zhou, J. R. Long and O. M. Yaghi, *Chem. Rev.*, 2012, **112**, 673-674.
23. H. C. Zhou and S. Kitagawa, *Chem. Soc. Rev.*, 2014, **43**, 5415-5418.
24. B. M. Weckhuysen and J. Yu, *Chem. Soc. Rev.*, 2015, **44**, 7022-7024.
25. J. Urquhart, *World's first commercial MOF keeps fruit fresh*, https://www.chemistryworld.com/news/worlds-first-commercial-mof-keeps-fruit-fresh/1017469.article, Accessed 19/10/16, 2016.
26. S. Horike, S. Shimomura and S. Kitagawa, *Nat. Chem.*, 2009, **1**, 695-704.
27. S. A. Hodgson, J. Adamson, S. J. Hunt, M. J. Cliffe, A. B. Cairns, A. L. Thompson, M. G. Tucker, N. P. Funnell and A. L. Goodwin, *Chem. Commun.*, 2014, **50**, 5264-5266.
28. A. B. Cairns, J. Catafesta, C. Levelut, J. Rouquette, A. van der Lee, L. Peters, A. L. Thompson, V. Dmitriev, J. Haines and A. L. Goodwin, *Nat. Mater.*, 2013, **12**, 212-216.
29. W. Cai and A. Katrusiak, *Nat. Commun.*, 2014, **5**, 4337.

30. P. Serra-Crespo, A. Dikhtiarenko, E. Stavitski, J. Juan-Alcaniz, F. Kapteijn, F. X. Coudert and J. Gascon, *CrystEngComm*, 2015, **17**, 276-280.
31. F. X. Coudert, *Chem. Mater.*, 2015, **27**, 1905-1916.
32. W. Li, M. R. Probert, M. Kosa, T. D. Bennett, A. Thirumurugan, R. P. Burwood, M. Parinello, J. A. K. Howard and A. K. Cheetham, *J. Am. Chem. Soc.*, 2012, **134**, 11940-11943.
33. R. Lyndon, K. Konstas, B. P. Ladewig, P. D. Southon, P. C. Kepert and M. R. Hill, *Angew. Chem. Int. Ed.*, 2013, **52**, 3695-3698.
34. T. D. Bennett, A. K. Cheetham, A. H. Fuchs and F. X. Coudert, *Nat Chem*, 2016, **9**, 11-16.
35. E. J. Carrington, I. J. Vitorica-Yrezabal and L. Brammer, *Acta Crystallogr. Sect. B-Struct. Sci.*, 2014, **70**, 404-422.
36. S. C. McKellar and S. A. Moggach, *Acta Crystallogr. Sect. B-Struct. Sci.*, 2015, **71**, 587-607.
37. E. C. Spencer, J. A. Howard, G. J. McIntyre, J. L. Rowsell and O. M. Yaghi, *Chem. Commun.*, 2006, 278-280.
38. S. Yang, J. Sun, A. J. Ramirez-Cuesta, S. K. Callear, W. I. David, D. P. Anderson, R. Newby, A. J. Blake, J. E. Parker, C. C. Tang and M. Schroder, *Nat. Chem.*, 2012, **4**, 887-894.
39. N. Lock, M. Christensen, C. J. Kepert and B. B. Iversen, *Chem. Commun.*, 2013, **49**, 789-791.
40. H. Wu, W. Zhou and T. Yildirim, *J. Phys. Chem. C*, 2009, **113**, 3029-3035.
41. J. L. Rowsell, E. C. Spencer, J. Eckert, J. A. Howard and O. M. Yaghi, *Science*, 2005, **309**, 1350-1354.
42. Y. H. Hu and L. Zhang, *Phys. Rev. B*, 2010, **81**, 174103-174103.
43. V. K. Peterson, Y. Liu, C. M. Brown and C. J. Kepert, *J. Am. Chem. Soc.*, 2006, **128**, 15578-15579.
44. V. K. Peterson, C. M. Brown, Y. Liu and C. J. Kepert, *J. Phys. Chem. C*, 2011, **115**, 8851-8857.
45. J. Getzschmann, I. Senkovska, D. Wallacher, M. Tovar, D. Fairen-Jimenez, T. Duren, J. M. van Baten, R. Krishna and S. Kaskel, *Microporous Mesoporous Mater.*, 2010, **136**, 50-58.
46. H. Wu, J. M. Simmons, Y. Liu, C. M. Brown, X. S. Wang, S. Ma, V. K. Peterson, P. D. Southon, C. J. Kepert, H. C. Zhou, T. Yildirim and W. Zhou, *Chem. Eur. J.*, 2010, **16**, 5205-5214.
47. Z. Hulvey, K. V. Lawler, Z. W. Qiao, J. Zhou, D. Fairen-Jimenez, R. Q. Snurr, S. V. Ushakov, A. Navrotsky, C. M. Brown and P. M. Forster, *J. Phys. Chem. C*, 2013, **117**, 20116-20126.
48. H. Wu, J. M. Simmons, G. Srinivas, W. Zhou and T. Yildirim, *J. Phys. Chem. Lett.*, 2010, **1**, 1946-1951.
49. K. W. Chapman, G. J. Halder and P. J. Chupas, *J. Am. Chem. Soc.*, 2008, **130**, 10524-+.
50. A. L. Spek, *J. Appl. Crystallogr.*, 2003, **36**, 7-13.
51. C. Zhang, J. A. Gee, D. S. Sholl and R. P. Lively, *J. Phys. Chem. C*, 2014, **118**, 20727-20733.
52. M. I. H. Mohideen, B. Xiao, P. S. Wheatley, A. C. McKinlay, Y. Li, A. M. Z. Slawin, D. W. Aldous, N. F. Cessford, T. Duren, X. B. Zhao, R. Gill, K. M. Thomas, J. M. Griffin, S. E. Ashbrook and R. E. Morris, *Nat. Chem.*, 2011, **3**, 304-310.
53. S. C. McKellar, A. J. Graham, D. R. Allan, M. I. H. Mohideen, R. E. Morris and S. A. Moggach, *Nanoscale*, 2014, **6**, 4163-4173.

54. S. M. Cohen, *Chem. Sci.*, 2010, **1**, 32-36.
55. K. K. Tanabe and S. M. Cohen, *Chem. Soc. Rev.*, 2011, **40**, 498-519.
56. Z. Q. Wang and S. M. Cohen, *Chem. Soc. Rev.*, 2009, **38**, 1315-1329.
57. M. I. Gonzalez, E. D. Bloch, J. A. Mason, S. J. Teat and J. R. Long, *Inorg. Chem.*, 2015, **54**, 2995-3005.
58. K. Manna, T. Zhang and W. B. Lin, *J. Am. Chem. Soc.*, 2014, **136**, 6566-6569.
59. S. Kitagawa and M. Kondo, *Bull. Chem. Soc. Jpn.*, 1998, **71**, 1739-1753.
60. T. Loiseau, C. Serre, C. Huguenard, G. Fink, F. Taulelle, M. Henry, T. Bataille and G. Ferey, *Chem. Eur. J.*, 2004, **10**, 1373-1382.
61. C. Serre, S. Bourrelly, A. Vimont, N. A. Ramsahye, G. Maurin, P. L. Llewellyn, M. Daturi, Y. Filinchuk, O. Leynaud, P. Barnes and G. Ferey, *Adv. Mater.*, 2007, **19**, 2246-2251.
62. L. J. Chen, J. P. S. Mowat, D. Fairen-Jimenez, C. A. Morrison, S. P. Thompson, P. A. Wright and T. Duren, *J. Am. Chem. Soc.*, 2013, **135**, 15763-15773.
63. T. Devic, F. Salles, S. Bourrelly, B. Moulin, G. Maurin, P. Horcajada, C. Serre, A. Vimont, J. C. Lavalley, H. Leclerc, G. Clet, M. Daturi, P. L. Llewellyn, Y. Filinchuk and G. Ferey, *J. Mater. Chem.*, 2012, **22**, 10266-10273.
64. L. Hamon, P. L. Llewellyn, T. Devic, A. Ghoufi, G. Clet, V. Guillerm, G. D. Pirngruber, G. Maurin, C. Serre, G. Driver, W. van Beek, E. Jolimaitre, A. Vimont, M. Daturi and G. Ferey, *J. Am. Chem. Soc.*, 2009, **131**, 17490-17499.
65. L. Hamon, A. Vimont, C. Serre, T. Devic, A. Ghoufi, G. Maurin, T. Loiseau, F. Millange, M. Daturi, G. Ferey and G. De Weireld, *Study of Hydrogen Sulphide Adsorption on Mil-47(V) and Mil-53(Al, Cr, Fe) Metal-Organic Frameworks by Isotherms Measurements and in-Situ Ir Experiments*, Royal Society of Chemistry, 2009.
66. R. El Osta, A. Carlin-Sinclair, N. Guillou, R. I. Walton, F. Vermoortele, M. Maes, D. de Vos and F. Millange, *Chem. Mater.*, 2012, **24**, 2781-2791.

-Chapter Two-
Experimental and Computational Methods

2.1 Synopsis

This chapter provides an overview of the methodologies which underpin the work in this thesis. The chapter is split into two sections, with the first covering the experimental methods, namely high-pressure X-ray diffraction and nanoindentation, along with how the mechanical properties can be extracted from these measurements. The second section covers the computational methodologies, which in this thesis cover both classical Newtonian physics (molecular mechanics) and quantum mechanics (QM).

2.2 Experimental methods

2.2.1 High-pressure crystallography

High pressure crystallography can be a powerful tool to understand the structure-property relationship of a material. High pressure diffraction was first attempted soon after the discovery of X-rays to determine crystal structures, with Cohn *et al*. carrying out high pressure powder diffraction in 1933.[1] The apparatus designed for creating pressure on the sample consisted of a steel pressure bomb, which allowed for compression of gas (usually helium) and the sample. The cell was equipped with two beryllium windows to allow the incident and diffracted beams to pass through. These first experiments yielded poor data due to the primitive equipment. The data were poor as the diffraction angle was limited by the design of the windows and the reflections had to be strong enough to register against the noisy background arising from the pressure cell itself. The pressures apparatus could obtain were also quite modest (≈ 0.1 GPa or 1000 bar). Since these first investigations, great improvements to the apparatus have been made, with the most notable being the development of diamond anvil based pressure cells. First introduced

in 1958 at the National Institute of Standards and Technology (NIST) as an apparatus for high pressure Raman spectroscopy, it was quickly realised that the cell lent itself well to X-ray diffraction due to its compact size (resulting in an easy fit onto goniometer heads and the fact that the diamond windows resulted in 180° optical transmission.[4, 5] Today, diamond anvil cells (or DACs) are the work horse in many branches of high-pressure science, including geosciences, biology, condensed matter physics as well as chemistry. The original design of the cell has been modified to increase the quality of data produced.[6, 7] The schematic diagram in **Figure 2.1** shows the components of the modified Merril-Bassett DAC used for the experiments in this thesis. The cell is composed of two steel plates which have a conical hole at the centre, with a half opening angle of 40 °, to permit optical viewing of the sample and diffraction pattern. The two plates house tungsten carbide backing seats that hold the opposing diamond anvils in place. A metal gasket, made from materials such as tungsten or Inconel (which has a cylindrical hole drilled through it of 200-300 μm in diameter) is placed between flat-faced 'culet' diamond anvils in order to create a cylindrical sample chamber. The pressure inside the sample chamber is increased by forcing the diamond faces closer together, which is achieved by tightening the three Allen screws which force the steel plates together.

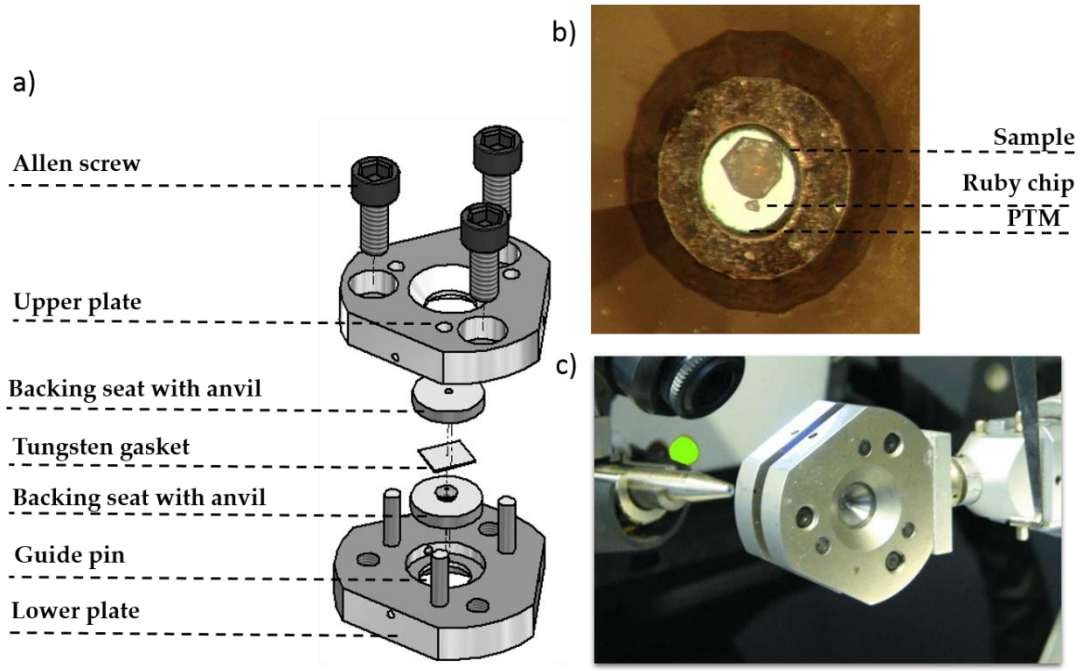

Figure 2.1:(a) Exploded view of a Merril-Basset DAC used for single-crystal X-ray diffraction.[7] (b) View of sample chamber containing single crystal sample, ruby chip and PTM. (c) Picture of DAC mounted on diffractometer.

The sample chamber usually contains a single crystal (or powder) surrounded by a small amount of pressure transmitting medium (PTM), which is used to apply pressure hydrostatically (that is, isotropically) to the sample when the two diamonds are brought together. The cell loading depends on the PTM of choice, which can either be a liquid, gas or even a soft solid. Liquid media are simply pipetted into the chamber, whilst gases can be loaded using more complex methodologies such as gas loading or cryoloading (see **Chapter 4**). Along with the sample, a ruby chip is also placed inside the chamber (**Figure 2.1**) which serves as a pressure calibrant through the well-established ruby fluorescence method, as the fluorescence transition of ruby is dependent on the pressure applied.

The high-pressure diffraction experiments described in this thesis were either carried out on a Bruker APEX-II diffractometer with a CCD detector, or on station I19 using EH1 with a Huber 4-circle goniometer with a Rigaku Saturn 724 CCD detector. In both cases a modified data collection strategy is required to account for the shading of the body of the cell and to optimise data collection times. Based on the work by Dawson *et. al.* a typical data collection is outlined in **Table 2.1** , where eight runs of 0.3° ω scans are performed at different values of ϕ and 2θ to ensure the angle between the incident beam and the cell axis is less than 40° and less than 80% of the detector is shaded.[2]

Table 2.1: Typical run list of a high-pressure diffraction experiment.[2]

Run	2θ / °	ϕ / °	ω range / °
1	-28	90	-10 to -40
2	28	90	40 to -25
3	-28	90	-155 to -220
4	28	90	-140 to -170
5	-28	270	-155 to -220
6	28	270	-140 to -170
7	-28	270	-10 to -40
8	28	270	40 to -25

In addition to a modified data collection, the processing of high-pressure single crystal data is non-standard compared to routine single-crystal diffraction experiments. Firstly, in order to index the sample, the harvested reflections need to be "cleaned up", as it is not only sample reflections that are present on the CCD detector. The images also contain powder rings from the

tungsten carbide (WC) backing seats, intense reflections from the diamond anvil and also the ruby chip, which all must be subtracted from the data pertaining to the sample. Once indexed, the sample data must be integrated with dynamic masks, which allow for areas of the images that are shaded by the body of the cell to be excluded from the integration of the reflections. Once all reflections have been integrated, those which are poorly measured due to partial shading of the cell or overlap with diamond reflections must be omitted. This is carried out using the program SHADE, which automatically omits reflections with a poor profile correlation coefficient that are within 2° from the cell opening angle (i.e. between 38-42°).[8]

With well diffracting, high-symmetry systems the data quality obtained from high-pressure data is comparable to data obtained under ambient conditions, with comparable errors on structural parameters. Cases where data quality still proves challenging are low-symmetry systems and weakly diffracting samples.

Further to understanding the atomistic structure at pressure, this thesis also aims to characterise bulk mechanical properties of materials, specifically hardness, elasticity and bulk compressibility.

2.2.2 Bulk modulus

The bulk modulus (denoted by K in this thesis, although sometimes given the symbol B) is a measure of resistance of a material to uniform (hydrostatic) compression and can be measured by means of high-pressure X-ray diffraction experiments. More formally, the bulk modulus of a material characterises the

variation of the volume of a solid with increasing pressure at constant temperature and is defined as:

$$\boldsymbol{K = -V\left(\frac{\partial P}{\partial V}\right)_T}$$

Equation 2.1

where V = volume, P = pressure and T = temperature. K can be determined by fitting an ideal equation of state (EoS) to pressure-volume data. Several forms of EoS exist; in this thesis the Birch-Murnaghan (B-M) EoS has been utilised, as it is one of the most commonly used. B-M theory is based on a Taylor expansion series, whereby adding increasing derivative truncation order terms allows more complex behaviour to be ascertained.[9] Usually, only 2nd or 3rd order B-M EoS are used, with 1 or 3 parameters being refined, respectively. This thesis uses 2nd order B-M EoS, to be able to compare with previous literature on mechanical properties of porous solids. [10]

2.2.3 Nanoindentation

One technique used widely in materials science to measure uniaxial compression and the hardness of materials is nanoindentation. This technique consists of pressing a tip made of a very hard material (usually diamond, of a few hundred nanometers in diameter) onto a single crystal of the material of interest. The elastic behaviour of porous materials can be highly anisotropic, thus the indentation data is dependent upon the direction of indentation.[11] In order to know which crystallographic face is being indented, and the direction of compressions directly within the crystal structure, the crystals need to be pre-face indexed. By measuring the load placed on the tip against the

displacement, the load-displacement curve is obtained, from which the mechanical properties of the crystal are extracted. (**Figure 2.2**). This includes the hardness and elastic modulus, which is calculated in this thesis by the Oliver and Pharr method.[3]

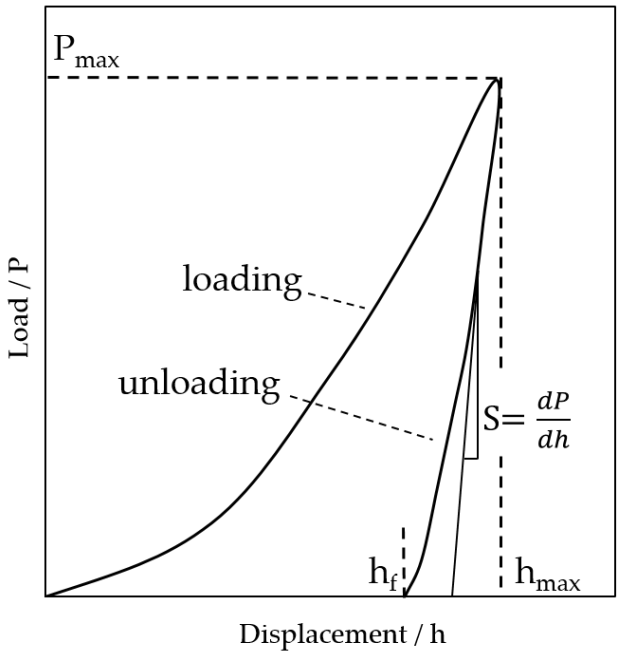

Figure 2.2: Example of a load displacement curve. In this case S represents the stiffness of the sample being indented, h_{max} is the maximum displacement, h_f is the final depth and P_{max} the maximum load. Modified from Oliver and Pharr.[3]

2.2.4 Hardness

The hardness (H) of a material can be estimated from the following relationship:

$$H = \frac{P_{max}}{A}$$

Equation 2.2

where P_{max} is the maximum load and A is the contact area. The contact area can be obtained by using an area function $F(d)$ that describes the projected area of the indenter at a distance d.[3] This can be done as the shade of the tip is accurately known (usually a Berkovich triangular pyramid), as well as its tensile strength.

2.2.5 Young's modulus

The Young's (or sometimes Elastic) modulus provides a measure of the resistance of a materials to deform elastically when a linear force is applied to it. The effective Young's modulus (E_{eff}) is related to the slope of the curve (**Figure 2.2**) upon unloading – the stiffness (S) by:

$$\boldsymbol{S = \beta \frac{2}{\sqrt{\pi}} E_{eff} \sqrt{A}}$$

Equation 2.3

where, β is a dimensionless constant, usually unity, and A is again the contact area at a known indentation depth. E_{eff} refers to the elastic modulus of both the indented material and the tip used for indentation. To deconvolute the elastic modulus of the material in question, E, the equation below can be solved:

$$\boldsymbol{\frac{1}{Eeff} = \frac{1 - v^2}{E} + \frac{1 - v_i^2}{E_i}}$$

Equation 2.4

where E_i and v_i are the Young's modulus and Poisson's ratio, respectively, of the indenting tip, and E and v are the Young's modulus and Poisson's ratio, respectively, of the indented material.

2.3 *Computational methods*

As previously mentioned, this thesis involves the combination of both classical and *ab initio* methods in order to fully understand the systems of study. Classical methods fall under molecular mechanics, where a force-field from empirical data is used for simulation purposes. The assumption for classical simulations is that the atoms can be treated as classical objects, i.e. modelled as spheres (atoms) connected by springs (bonds). Electrons are not modelled and are ignored. The force field empirically represents both the bonded (intramolecular) and non-bonded (intermolecular) interactions: the bonded terms takes into account bond stretching, bending and torsional motions, whereas the non-bonded terms include van der Waals and electrostatic interactions. Advantages of running classical simulations are that they are quick to compute and large systems can be modelled with modest computing resources. The other modelling method employed in this work was quantum mechanics, where electrons are explicitly modelled. The structure in question is expressed using a wavefunction, Ψ, which is a function of the coordinates of all elementary particles. The simplest form of the Schrödinger equation describes the behaviour of a system using the wave function as follows:

$$\hat{H}\Psi = E\Psi$$

Equation 2.5

where, $\hat{H}$ is the Hamiltonian operator, and E is the total energy of the system. Such an equation can be solved exactly only for very simple cases, such as the particle in a box example. Thus the N-electron Schrödinger equation needs to be approximated to be solved; density functional theory (DFT) provides such an approximate framework for determining the (approximate) ground state electronic structure. DFT expresses the total energy as a function of the electron distribution that in turn is a spatially dependent function for the

electron density. Since the electrons are modelled explicitly, QM methods allow for calculations of any molecular properties of interest (in principle). This, however, comes at a cost: QM calculations are computationally much more demanding than their force-field-based counterparts.

2.3.1 Classical molecular simulation

2.3.1.1 Statistical mechanics

Statistical mechanics allows the study of many-body systems by applying mathematical tools to relate microscopic and macroscopic properties of a system.[12] In this thesis, this can be applied to the study of adsorption in porous materials, where a microstate is described by microscopic properties *i.e.* the instantaneous positions and velocities of the adsorbate in a pore.[13] As the molecules move around the pores, the system passes through numerous instantaneous microstates. On the macroscopic level the same system at equilibrium is described using pressure, temperature and volume, i.e. a macrostate.

For a given macrostate there are a large number of possible microstates. One of the underlying principles of statistical mechanics is that over time or phase space, the number of microstates that the system passes through increases. As the time or space sampled approaches infinity, all possible microstates of a system at equilibrium are obtained. This is the ergodic hypothesis. Essentially, this means that average properties determined by averaging over a large number of microstates that are not connected in time (randomly selected i.e. through Monte Carlo), are the same as the average properties of a system obtained by observing the system over time (molecular dynamics). For a desired property, *M*, this means:

$$M_{observed} = \langle M \rangle_{ensemble} = \sum_i M_i \, P_i$$

Equation 2.6

where $M_{observed}$ is the value of M obtained by averaging over time and $\langle M \rangle_{ensemble}$ is obtained by summing the value of M for each microstate in the ensemble Mi, multiplied by the probability of finding that particular microstate in the ensemble, P_i.

Microstates making up an ensemble must share three constant properties. The three which are used in this thesis are:

(i) Grand canonical ensemble: Constant chemical potential (μ), volume (V) and temperature (T).

(ii) Canonical ensemble: Constant number of molecules (N), volume (V) and temperature (T).

(iii) Isobaric-isothermal: Constant number of molecules (N), pressure (P) and temperature (T).

The most appropriate ensemble for the study of adsorption is the grand canonical ensemble, as the volume, temperature and chemical potential of a system are kept constant, while the number of molecules is allowed to change. At equilibrium the chemical potential and temperature in the adsorbed phase must be the same as in the bulk phase reservoir. In order to reach equilibrium, the number of molecules is allowed to change either by removing molecules from the simulation cell or by introducing molecules from the bulk reservoir. This bears a resemblance to an experimental set-up for adsorption where an

adsorbent is in contact with a bulk fluid, and a transfer of molecules from the bulk phase to the adsorbed phase leads to equilibrium.

Comparably, a grand canonical ensemble is made up of microstates all having the same chemical potential, volume and temperature. The partition function, $Q(\mu,V,T)$, of such an ensemble is defined as the sum over of all possible microstates. The microstates at a chosen temperature T can vary in energy, E_k, following a Boltzmann distribution, and also in the number of molecules in the system N consistent with T and μ, which can also be described by the Boltzmann distribution. The partition function takes the form of:

$$Q_{(\mu,V,T)} = \sum_{k,N} \left(e^{-\beta E_k}\right)\left(e^{\beta \mu N}\right)$$

Equations 2.7

where,

$$\beta = \frac{1}{k_B T}$$

Equation 2.8

The probability of encountering a microstate k with N particles and energy E_k in a grand canonical ensemble of microstates is represented as:

$$P_{k,N} = \frac{\left(e^{-\beta E_k}\right)\left(e^{\beta \mu N}\right)}{Q_{(\mu,V,T)}}$$

Equation 2.9

The ensemble average of a desired property, $\langle M \rangle$ can then be determined by summing the value of the property(M) at each microstate k and using $P_{k,N}$ as a weighing factor in order to reflect the likelihood of its occurrence. In classical

mechanics, each microstate is expressed as the positions and momenta of the molecules in the system at a particular point in phase space. So, M can be expressed as an integral across the phase space that is evaluated over all momenta, $\boldsymbol{q}$, and positions, $\boldsymbol{s}$:

$$M = \int M\,(q,s)\,\rho(q,s)dq\,ds$$

Equation 2.10

where, ρ is the probability distribution in classical mechanics. This expression can be simplified by making the assumption that the total energy can be divided into a potential energy term and kinetic energy term, where the first is dependent only on the positions and the latter the momenta. The potential energy, U(s), is a result of intermolecular interactions, and is therefore dependent on the positions of the molecules in the system. The kinetic term is determined using the expression for the kinetic energy of a monoatomic particle:

$$E_k = \frac{V}{\Lambda^3}$$

Equation 2.11

$$\text{where} \qquad \Lambda = \hbar\sqrt{\frac{\beta}{2\pi m}}$$

Equation 2.12

Λ is the de Broglie wavelength of a particle, $\hbar$ is Planck's constant, and m is the mass of the particle. ρ, the classical probability distribution can now be described as:

$$\rho(s^N) = \frac{1}{Q_{(\mu,V,T)}} \frac{V^N}{N!\,\Lambda^{3N}} (e^{\beta\mu N})(e^{-\beta U(s^N)})$$

Equation 2.13

In turn, the classical expression for the ensemble average of a desired property, <*M*> can be expressed and computed much more easily than the quantum expression as:

$$\langle M \rangle_{\mu,V,T} = \frac{1}{Q_{(\mu,V,T)}} \sum_N \frac{V^N}{N!\,\Lambda^{3N}} \int M\,(s^N)\,(e^{\beta\mu N})(e^{-\beta U(s^N)}) ds^N$$

Equation 2.14

2.3.1.2 Grand canonical Monte Carlo (GCMC) method

The Monte Carlo method works by integrating **Equation 2.14**, at a series of randomly chosen points in order to evaluate a macroscopic property, <*M*>. In its simplest form, the algorithm works by randomly, but comprehensively, sampling points across the configuration space, and the contribution of each point to the value of the overall integral is unweighted. The algorithm consists of a random walk through phase space, where the moves generate a so-called Markov chain of configurations. A Markov chain is a "memory-less" sequence of configurations, where the decision to move to a new configuration is only affected by the current configuration, and not by previous configurations. In the grand canonical ensemble, a Markov chain is created by alternating between the following trial moves:

- Inserting a molecule at a random position.
- Deleting a randomly chosen molecule.
- Moving a molecule to a random new position.

Moves are accepted or rejected according to acceptance rules, and detailed balance is conserved.[13] For a trial move where one molecule is randomly moved from one configuration (o) to a new position (n) while the total number of molecules remains the same, the acceptance probability is:

$$acc\left(o \to n\right) = \min(1, exp\{-\beta\big(U(n) - U(o)\big)\})$$

Equation 2.15

The probability of accepting a trial move of randomly inserting a molecule is expressed as:

$$acc\left(o \to n\right) = \min(1, \frac{V}{\Lambda^3(N+1)}(e^{[\beta\left(\mu - U(N+1) + U(N)\right)]}$$

Equation 2.16

where μ, the chemical potential can be expressed as function of fugacity:

$$\mu = \frac{1}{\beta}\ln(\beta f \Lambda^3)$$

Equation 2.17

using an EoS (in this thesis the Peng Robinson EoS was implemented) the fugacity of the bulk phase at a given pressure can be easily determined. For more details on statistical mechanics and the Monte Carlo method, the reader is referred to the textbooks of Frenkel and Smit and Hill.[13] [12]

2.3.1.3 Potentials

Classical simulations make use of force fields to calculate the potential energies of both sorbate-sorbate and sorbate-framework interactions. The total potential energy is summed over all bonded and non-bonded interactions. The

non-bonded interaction are split into van der Waals (dispersion) and Coulombic interactions.

The van der Waals interactions were calculated with a Lennard-Jones (LJ) 12-6 potential, such that:

$$V_{ij} = 4\varepsilon_{ij}\left[\left(\frac{\sigma_{ij}}{r_{ij}}\right)^{12} - \left(\frac{\sigma_{ij}}{r_{ij}}\right)^{6}\right]$$

Equation 2.18

where V_{ij} the intermolecular energy between two LJ spheres, i and j, separated by a distance r_{ij}, ε_{ij} is the depth of the potential well, and σ_{ij} is the LJ sphere diameter. For a pair of molecules separated by a large r_{ij}, the dispersion interaction described by the Lennard-Jones potential is close to zero. As a result such interactions can be considered negligible. In GCMC simulations, a cut-off value is normally assigned for the calculation of dispersion interactions, beyond which all contributions are considered to be null. Such an approach is justified as the Lennard-Jones potential approaches zero at high separation distances.

For polar and quadrupolar fluid molecules, simulations must take into account electrostatic, or Coulombic interactions as well as dispersion. Each LJ interaction centre, whether it is part of the framework, or part of a fluid molecule, is assigned a partial charge. Based on these partial charges, the Coulombic potential energy for the system being modelled is calculated as follows:

$$U_{coulombic} = \sum_{i=1}^{N} \sum_{j=i+1}^{N} \frac{q_i q_j}{4\pi\varepsilon_0 r_{ij}}$$

Equation 2.19

where, q_i and q_j are the partial charges assigned to the spheres *i* and *j*, separated by a distance r_{ij}. *N* is the total number of interaction spheres and ε_0 is the permittivity in vacuum. These long range interactions are summed using the Ewald summation method, as described in Frenkel and Smit.[13]

The force field parameters for MOF atoms are usually taken from generic force fields such as the Universal Force Field (UFF) and the Dreiding force field.[14, 15] This thesis used the UFF force field for the framework atom parameters. The LJ parameters for the fluid molecules were taken from more specialist force fields. N_2, and O_2 were modelled as three-centred LJ spheres using the TraPPE force field, where one dummy sphere is needed to adequately describe the charge distribution within the molecule.[16] Methanol was also modelled using the TraPPE force field, with additional angle bending flexibility integrated into the model.[17]

2.3.2 Quantum mechanical methods

2.3.2.1 Density functional theory

Density functional theory has revolutionised many areas of physical sciences since its beginnings in specialist quantum mechanical theory. It is now widely used in chemistry, physics, materials science and geology. This provides a short introduction to DFT; for a more in-depth review of the subject, see the textbooks by Parr and Yang[18] and Sholl.[19]

The technique stems from two theorems proved by Kohn and Honenberg.[20] One states that: *"the ground-state energy from Schrödinger's equation is a unique functional of the electron density"*[20] which simplifies the Schrödinger equation from a *3N* variable (the wavefunction, where *N* is the number of electrons) to a 3 dimension variable. In practical terms, this means that solving the ground state energy of Schrödinger's equation for only one arm of a framework which is extensively studied in this thesis – $(Zr_6O_4(OH)_4)(O_2CC_6H_4C_6H_4CO_2)_{12}$ - is reduced from 5388 dimensions to only 3. The second theorem states *"the electron density that minimises the energy of the overall functional is the true electron density corresponding to the full solution of the Schrödinger equations."*[20] In theory, this would mean that if the functional was known, the energy of any structure could be solved, by varying the parameters defining the electron density until the energy from the functional is minimized.[20] However in practice, the true functional that provides a 1:1 mapping between the electron density and the energy is not known; the functionals used are burdened by approximations.[21]

Within the formalism of DFT, the total ground state energy of a system, both kinetic and potential energy terms (Hamiltonian operator), can be written as a functional of the electron density:

$$E_{total}[\rho] = T_k[\rho] + V_{ne}[\rho] + V_{nn}[\rho] + V_{ee}[\rho] + E_{XC}[\rho]$$

Equation 2.20

where T_k is the kinetic energy of the electrons, V_{ne} is the potential energy between the nuclei and the electrons, V_{nn} is the potential energy between the nuclei and V_{ee} is the potential energy between the electrons. In this equation, there is no explicit term for the kinetic energy of the nuclei: V_{nn} becomes a constant through application of the Born-Oppenheimmer approximation.[22]

This assumes that the size of the nucleus compared to the electrons is so large that relative to the electrons, the kinetic energy of the nuclei fall to zero. Thus, V_{nn} describes a stationary (constant) Coulombic energy term. $E_{XC}[\rho]$ is the exchange/correlation functional which describes both electron exchange and electron correlation. Electron exchange, is the effect of lowering the energy by the pairing up of electrons of opposite spin in molecular orbitals, and electron correlation is the fact that the movement of one electron will affect all the other electrons. Both terms effectively act to separate the electrons and are thus stabilizing quantities. Current functionals approximate both effects by constructing equations derived from one-electron holes.[21]

2.3.2.2 Functionals

The most commonly used functionals fall into two classes: the local density approximation (LDA) and the generalized gradient approximation (GGA). LDA is based on the uniform electron gas, where the electron density is constant throughout all space. It works by replacing the changing ρ in small regions in space, with a constant ρ. The functional does not cope well with rapidly changing electron density; which is closer to reality in the case of molecular systems. It has found notable success, however, for metallic systems where the crystal packing is closer to the idealized packing of 'hard spheres', such that the variation in electron density is minimal. GGA functionals represent a step forward from LDA in that information on the gradient of the electron density is included as a second component to the equations. These functionals can therefore cope better with the rapidly changing electron density of molecular systems. Examples of functionals of this type include BLYP,[23-25] PW91[26] and PBE.[27]

2.3.2.3 Basis Sets

Electronic wave functions can be expressed as linear functions of atomic orbitals. A set of mathematical equations used to describe the wavefunctions are called basis functions. Basis functions can be atom-centered Gaussian type orbitals (GTO) or delocalized plane wave basis sets. The latter are used in all the DFT calculations reported in this thesis, as they can naturally be applied in conjunction with periodic boundary conditions. The basis set is a summation of plane waves with varying weighting coefficients that represents the molecular wavefunction, and take the form of:

$$\Psi(r) = \sum C_G \exp(iG.r)$$

Equation 2.21

where, $\Psi(r)$ is the molecular wavefunction at position r, C_G is the weighting coefficient and *exp(iG.r)* is the plane wave defined with respect to the reciprocal lattice vectors, *G*. These vectors lie perpendicular to the crystal Miller index planes, and thus define the size and shape of the periodic boundary condition model (which is typically the crystallographic unit cell).

2.3.2.4 Pseudopotentials

When working with large systems, such as MOFs for example, a large number of basis functions are required to describe all molecular orbitals, which comes at a high computational cost. Especially in the case of metals, a large amount of computational power is spent on describing the molecular orbitals of inner core electrons. However, it is the valence electrons that play an important role in bonding interactions and must be defined explicitly. In contrast, the potential energy of the inner core electrons, which are invariant to chemical bonding, can be described using simpler (transferrable) expressions. In order

to reduce the computational demand associated with performing calculations with a large number of basis functions, the inner core electrons of atoms are often described using pseudopotentials, also known as effective core potentials. In this work, the pseudopotentials that were used in this thesis were created 'on the fly' by the CASTEP code.[28]

2.3.2.5 Ab initio Molecular Dynamics

One assumption made in all the classical simulations performed in this work is that the framework is rigid, with the atoms fixed in their crystallographic positions. In reality, atoms have a kinetic energy associated with a finite temperature, and are in constant motion. Their movement can have a large impact on the framework's mechanical properties. By studying the structure as a function of time by molecular dynamics, it is possible to find a more accurate representation of the framework than its crystal structure, which can help explain the mechanical properties observed experimentally.

In order to study the framework dynamics, *ab initio* molecular dynamics (AIMD) simulations were pursued. Like classical MD, the principle still involves integrating Newton's equations of motion to observe the change in atomic positions at a defined temperature over time, which is typically calculated in increments (time steps) on the femtosecond time scale. In classical MD, the potential energy surface is defined using force fields, whereas in AIMD, it comes from first principles. The advantage of AIMD is that there is no need for force field development of novel systems and, most importantly, there is a significant increase in the simulation accuracy.

2.4 References

1. W. M. Cohn, *Phys. Rev.*, 1933, **44**, 326-327.
2. A. Dawson, D. R. Allan, S. Parsons and M. Ruf, *J. Appl. Crystallogr.*, 2004, **37**, 410-416.
3. W. C. Oliver and G. M. Pharr, *J. Mater. Res.*, 2004, **19**, 3-20.
4. G. J. Piermarini, *J. Res. Natl. Stand.*, 2001, **106**, 889-920.
5. C. E. Weir, E. R. Lippincott, A. Vanvalkenburg and E. N. Bunting, *J. Res. Natl. Stand. Sec. A*, 1959, **63**, 55-62.
6. W. A. Bassett, *High. Press. Res.*, 2009, **29**, Cp5-186.
7. S. A. Moggach, D. R. Allan, S. Parsons and J. E. Warren, *J. Appl. Crystallogr.*, 2008, **41**, 249-251.
8. S. Parsons, *SHADE*, University of Edinburgh, Edinburgh, Scotland, 2004.
9. F. Birch, *Phys. Rev.*, 1947, **71**, 809-824.
10. K. W. Chapman, G. J. Halder and P. J. Chupas, *J. Am. Chem. Soc.*, 2008, **130**, 10524-10526.
11. J. C. Tan, T. D. Bennett and A. K. Cheetham, *Proc. Natl. Acad. Sci. U.S.A.*, 2010, **107**, 9938-9943.
12. T. L. Hill, *Statistical mechanics : principles and selected applications*, Dover Publications, New York, 1987.
13. D. Frenkel and B. Smit, *Understanding molecular simulation : from algorithms to applications*, 2nd edn., Academic Press, San Diego, 2002.
14. A. K. Rappe, C. J. Casewit, K. S. Colwell, W. A. Goddard and W. M. Skiff, *J. Am. Chem. Soc.*, 1992, **114**, 10024-10035.
15. S. L. Mayo, B. D. Olafson and W. A. Goddard, *J. Phys. Chem.*, 1990, **94**, 8897-8909.
16. J. J. Potoff and J. I. Siepmann, *AIChE J.*, 2001, **47**, 1676-1682.
17. B. Chen, J. J. Potoff and J. I. Siepmann, *J. Phys. Chem. B*, 2001, **105**, 3093-3104.
18. R. G. Parr and W. Yang, *Density-functional theory of atoms and molecules*, Oxford University Press, Oxford England, 1989.
19. D. S. S. Sholl, J.A., *Density Functional Theory: A Practical Introduction*, John Wiley & Sons Inc., Hoboken, New Jersey, 2009.
20. P. Hohenberg and W. Kohn, *Phys. Rev. B*, 1964, **136**, B864.
21. W. Kohn and L. J. Sham, *Phys. Rev.*, 1965, **140**, 1133.
22. M. Born and R. Oppenheimer, *Ann. Phys. Berlin*, 1927, **84**, 0457-0484.
23. A. D. Becke, *Phys. Rev. A*, 1988, **38**, 3098-3100.
24. C. T. Lee, W. T. Yang and R. G. Parr, *Phys. Rev. B*, 1988, **37**, 785-789.
25. B. Miehlich, A. Savin, H. Stoll and H. Preuss, *Chem. Phys. Lett.*, 1989, **157**, 200-206.
26. J. P. Perdew and Y. Wang, *Phys. Rev. B*, 1992, **46**, 12947-12954.

27. J. P. Perdew, K. Burke and M. Ernzerhof, *Phys. Rev. Lett.*, 1996, **77**, 3865-3868.

28. S. J. Clark, M. D. Segall, C. J. Pickard, P. J. Hasnip, M. J. Probert, K. Refson and M. C. Payne, *Z. Kristallogr.*, 2005, **220**, 567-570.

-Chapter Three-
The Effect of Pressure on Gating ZIFs

3.1 Synopsis

Using a joint computational and high-pressure single-crystal X-ray diffraction study on the isostructural zeolitic imidazolate frameworks (ZIFs) ZIF-8 ($Zn(MeIm)_2$, MeIm = 2-methylimidazole), ZIF-65 ($Zn(NO_2IM)_2$, NO_2Im = 2-nitroimidazolate), and ZIF-90 $(Zn(ICA))_2$, ICA = imidazolate-2-carboxyaldehyde), this chapter investigates their gate-opening mechanisms and finds that through ligand substitution the gate opening angle and onset pressure can be tuned. These isostructural ZIFs have varying polarity and it is this interaction with the guest molecule (in this case, methanol) which is the determining factor in the gating phenomenon. Upon application of pressure, the imidazolate rings rotate in order to increase both the pore volume and content. By using a combination of high-pressure crystallography, periodic density functional theory (DFT) and grand canonical Monte Carlo (GCMC) simulations, a full understanding of the driving force for gate-opening based on functionalisation of the imidazole linker and the guest molecule was reached.

3.2 Introduction

Zeolitic imidazolate frameworks (ZIFs) are a class of chemically stable porous materials.[2] Their structures are based on zeolite topologies, where imidazolate (Im, $C_3H_3N_2^-$) and Zn^{2+}, Co^{2+}, Li^+ or B^{3+} ions replace the oxygen and Al^{3+}/Si^{4+} species, respectively. Due to the greater distance between metal centres in ZIFs compared to zeolites, the pores are much larger and in addition, the imidazolate linker can be modified with relative ease to change the pore size

and pore-surface chemistry.[3] **Figure 3.1** shows a selection of common zeolite structures alongside their ZIF counterpart.

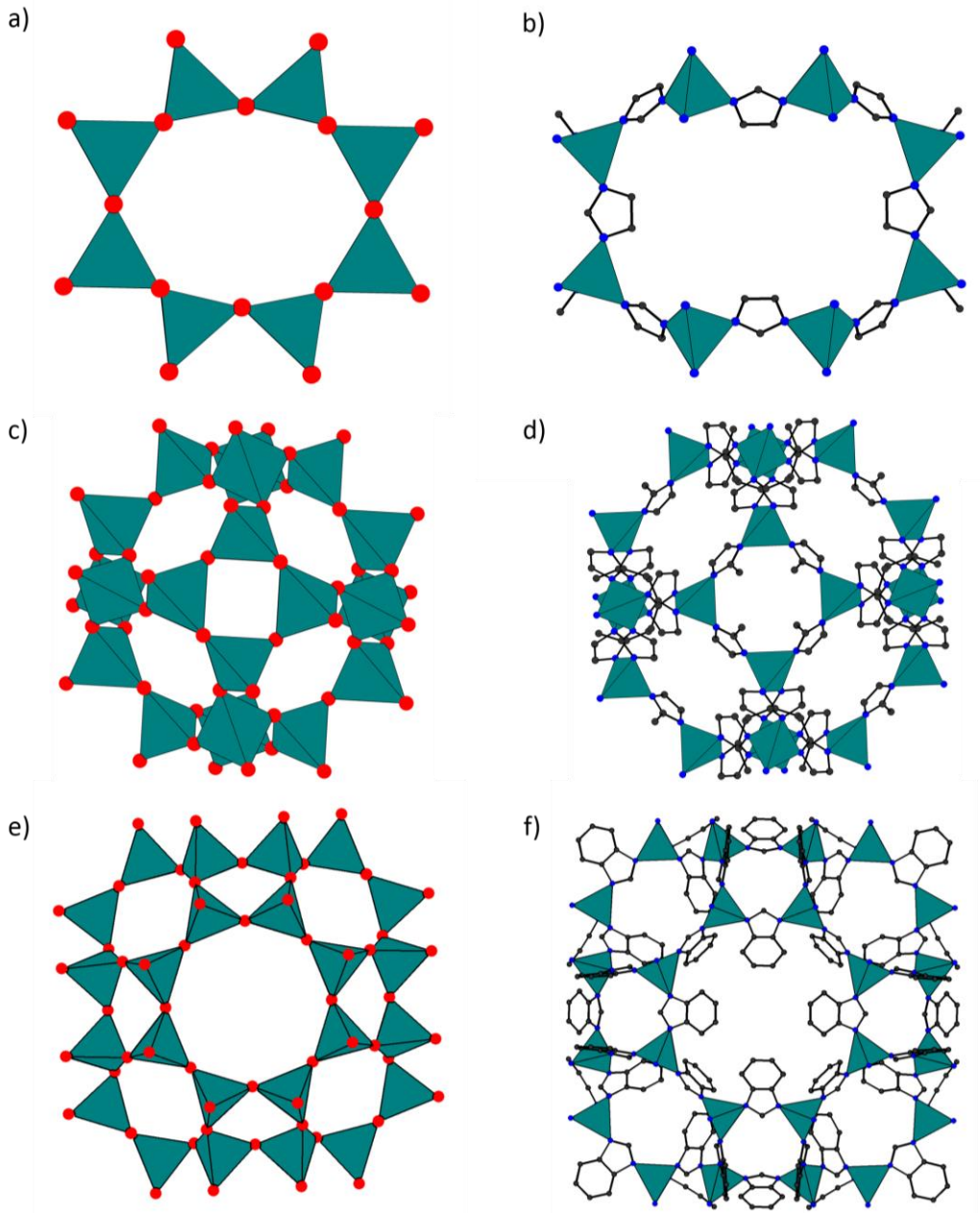

Figure 3.1: Comparison of zeolites and their ZIF topological counterparts for (a) Zeolite-DFT, (b) ZIF-3, (c) Zeolite-SOD, (d) ZIF-8, (e) Zeolite-RHO and (f) ZIF-11. The colour scheme is green tetrahedra: SiO_4, AlO_4 and ZnN_4, red: oxygen, blue: nitrogen, black: carbon. Hydrogen atoms are omitted for clarity.

One of the most well studied ZIFs is ZIF-8 ($Zn(MeIm)_2$, MeIm = 2-methylimidazole), which crystallises in the cubic space group *I*-43*m* (a=16.9856(16) Å, V=4900.5(8) $Å^3$) and has the sodalite topology (**Figure 3.1d**).[1] At ambient pressure and temperature, ZIF-8 contains one central nano-sized pore per unit cell, with a volume of ≈2500 $Å^3$ and pore diameter of 11.6 Å. Connecting these large nanopores are eight six-membered ring (6MR) windows c.a. 3.0 Å in diameter and six smaller four-membered ring (4MR) windows of c.a. 0.8 Å (**Figure 3.2**). Originally, the structure seemed promising for molecular sieving due to the small window diameters, as a 3.0 Å window should be able to selectively adsorb H_2 over CH_4, with kinetic diameters of 2.85 Å and 3.80 Å, respectively. However, in practise Bux *et al.* showed that many molecules with kinetic diameters larger than the 6MR window could permeate through ZIF-8, including O_2, N_2 and CH_4, though the mechanism for how this was possible was not explained.[4]

In 2009, Moggach *et al.* demonstrated in a high-pressure diffraction experiment using a diamond anvil cell (DAC) and a 4:1 methanol:ethanol hydrostatic medium that ZIF-8 undergoes a phase transition. Upon increasing the pressure to 0.18 GPa, the hydrostatic media entered the pores causing the unit cell volume to initially expand, and then the framework compresses to 0.90 GPa.[1] On increasing the pressure further (to 1.47 GPa), a single-crystal to single-crystal phase transition took place (from ZIF-8AP to ZIF-8HP, with AP and HP denoting the ambient and high-pressure phases, respectively). This transition was characterised by a rotation of the MeIm linker, quantified by defining an angle of rotation (θ, defined as the angle between the (100) plane

and the mean plane passing through the MeIm ring), which increases from 64.3° at ambient pressure to 89.7° at 1.47 GPa **(Figure 3.2**).

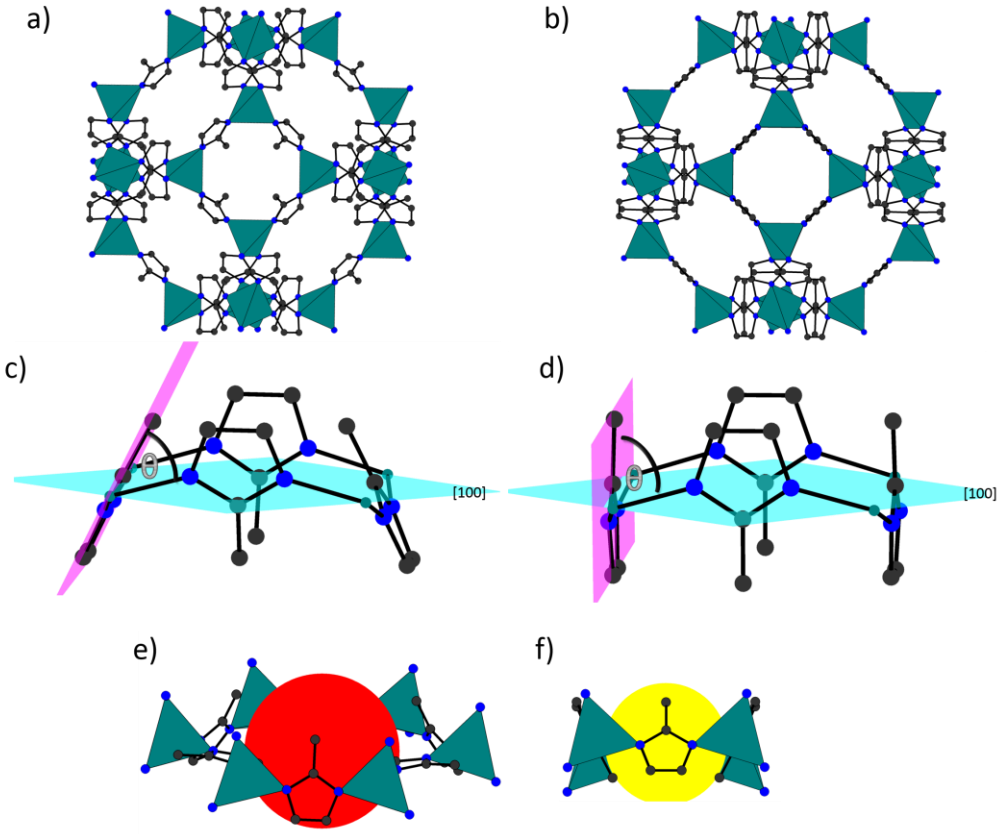

Figure 3.2: Packing arrangement of ZIF-8 at (a) ambient pressure (ZIF-8-AP) and (b) 1.47 GPa (ZIF-8-HP). Definition of the angle of rotation (θ) at (c) 64.30° for ZIF-8-AP and (d) 89.0° for ZIF-8-HP. (e) Six membered ring window (6MR), and (f) four membered ring window (4MR). Colour scheme as in Figure 3.1. H atoms are excluded for clarity. The (100) and the mean plane through the MeIm linker in (c) and (d) are coloured blue and magenta, respectively. The red and yellow spheres in (e) and (f) represent a window diameter of ZIF-8-AP of 3.0 Å and 0.8 Å, respectively.

This linker rotation increased the size of the windows that connect the nanopores in the centre of the unit cell, as the 4MR and 6MR window diameters increased from 0.8 Å to 2.2 Å, and 3.0 Å to 3.6 Å, respectively, which allowed more MeOH and EtOH molecules to enter the pores.[1] In a later study,

Fairen-Jimenez *et al*. used a combination of *in-situ* X-ray powder diffraction and GCMC simulations to demonstrate that the same phase transition took place upon guest adsorption at much lower pressure (for N_2 at 77 K it can be observed at ~0.4 bar).[5] More recently, the phase transition to the HP structure has also been used to explain the uptake of other gases including CO_2 and C1-C4 alkanes.[6] High-pressure crystallographic experiments are therefore an ideal way to probe the potential energy landscape of the framework on uptake of guest species.

ZIFs with an identical network structure to ZIF-8 have been synthesised, where the -CH_3 substituent has been replaced with either -CHO or -NO_2 groups. The resulting isostructural and isosymmetric frameworks are referred to as ZIF-90 $(Zn(ICA))_2$, ICA = imidazolate-2-carboxyaldehyde) and ZIF-65 $(Zn(NO_2IM)_2$, NO_2Im = 2-nitroimidazolate) respectively (**Figure 3.3**). Lattice parameters (*a* = 17.0758(13) Å and 17.3185(2) Å, respectively), and pore volumes (2354 $Å^3$ and 2619 $Å^3$, respectively) for ZIF-90 and ZIF-65 are comparable to ZIF-8 (~2500 $Å^3$). ZIF-65 is slightly larger due to the bulkier pendant -NO_2 group compared to the -CHO group of ZIF-90 that displays site-occupied disorder as the linker is bisected by a mirror plane.

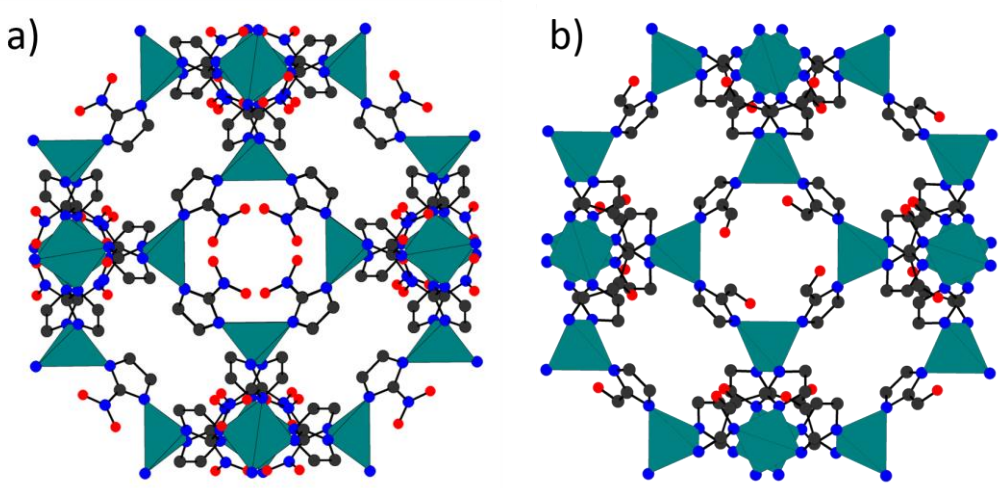

Figure 3.3: Packing arrangement of ZIF-65 (left) and ZIF-90 (right). Colour scheme as in Figure 1. The site-occupied disorder of the carbonyl O-atom in ZIF-90 has been removed for clarity.

Under ambient temperature and pressure ZIF-65 has a smaller θ value of 46.3° *c.f.* 64.3° and 66.5° for ZIF-8 and ZIF-90, respectively, this is reflected in the smaller limiting diameter of the 4MR window for ZIF-65 compared to ZIF-90 (0.8 Å compared to 1.4 Å). The 6MR window is slightly larger for ZIF-65 and ZIF-90 compared to ZIF-8 (see **Table 3.1**). ZIF-65 is of interest for carbon capture as it displays an increased affinity for CO_2, due to the NO_2 functionality, [7, 8] while ZIF-90 can be post-synthetically modified, for example, through the methodology of Caro *et al.*, who imine functionalised the aldehyde group to enhance H_2 selectivity over CO_2.[9] Other research groups have modified the aldehyde group to create heterogeneous catalysts, such as Park *et al*. who prepared F-ZIF-90, a quaternary ammonium iodide functionalised ZIF, which is capable of synthesising cyclic carbonates from CO_2 and epoxides with higher activity than other previously reported catalysts.[10] There are many other examples of transformations of the aldehyde group, for example, into a

thiol (SH), carboxyl (C(O)OH) or amino (NH_2) group, giving a rich variety of functionalities which could be used to help tailor host-guest interactions and tune the gate opening behaviour for separation technologies or catalytic processes.[11, 12]

Table 3.1: Diameter of 4MR and 6MR windows in ZIF-8, ZIF-65 and ZIF-90

ZIF	θ/ °	4MR diameter/ Å	6MR diameter/Å
ZIF-8	64.3	0.8	3.0
ZIF-65	46.3	0.8	3.2
ZIF-90	66.5	1.4	3.2

All diameters calculated in Mercury, with 0.2 Å grid spacing.

Herein, this chapter presents a combined high-pressure single-crystal diffraction and computational study on the isostructural ZIFs; ZIF-8, ZIF-90 and ZIF-65, in order to understand what effect changing the functional group and uptake of guest molecules into the pores has on gate opening behaviour.

3.3 Experimental

3.3.1 Synthesis

Note: the synthesis of ZIF-65 and ZIF-90 were carried out by Dr Thomas D. Bennett and Dr David Fairen-Jimenez of the University of Cambridge, respectively.

Synthesis of ZIF-90. A solid mixture of zinc(II) nitrate hexahydrate (0.07g, 2.10×10^{-5} mol) and imidazole-2-carboxaldehyde ICA; 0.029 g, 3×10^{-5} mol) was dissolved in dimethylformamide (DMF) (3 mL) in a 12 mL Teflon-capped borosilicate vial. The vial was heated at a rate of 200° C h^{-1} to 100 °C, held at this temperature for 18 h, and then cooled at a rate of 1° C h^{-1} to 90 °C, then cooled to room temperature at 5° C h^{-1}. The reaction DMF was exchanged for clean DMF several times. The orange crystals were retained in DMF before being analysed by SCXRD.

Synthesis of ZIF-65. A solid mixture of zinc(II) nitrate hexahydrate (0.03 g, 1×10^{-5} mol) and 2-nitroimidazole NO_2Im; 0.0565 g, 5×10^{-5} mol) was dissolved in DMF (3 mL) in a 12 mL Teflon-capped borosilicate vial. The vial was heated at a rate of 200 °C h^{-1} to 100 °C, held at this temperature for 18 h, and then cooled at a rate of 1 °C h^{-1} to 90 °C, then cooled to room temperature at 5 °C h^{-1}. The reaction DMF was exchanged for clean DMF several times. The crystals were retained in DMF before being analysed by SCXRD.

3.3.1 High-pressure crystallography

Laboratory Data Collection and Reduction. Prior to high pressure (HP) experiments, ambient temperature and pressure diffraction data were collected on a laboratory diffractometer for both ZIF-90 and ZIF-65 in order to compare with the HP studies (which were also collected at room temperature).

A single crystal was mounted onto a MiTiGen Microloops TM and a sphere of data were collected on a Bruker SMART APEX II diffractometer with graphite-monochromated Mo Kα radiation (λ= 0.71073 Å). These data were integrated using the program SAINT and the absorption correction was carried out using the program SADABS. [13, 14]

High-pressure Synchrotron Data Collection and Reduction. A single-crystal of both ZIF-90 and ZIF-65 was then placed in a modified Merrill-basset DAC [15, 16] along with a ruby chip (for pressure calibration)[17] and surrounded by a MeOH:EtOH (4:1) mixture, in two separate experiments. Diffraction data were collected on station I19 at the Diamond Light Source, Rutherford Appleton Laboratory, on a Huber 4-circle goniometer with a Rigaku Saturn 724 CCD detector using synchrotron radiation (wavelength = 0.4895 Å) from 0.14 GPa to 4.77 GPa for ZIF-65 and 0.11 GPa to 2.00 GPa for ZIF-90. Data were collected in ω scans, with a step size and exposure time of 0.3° and 1 s respectively. The data were integrated with the program SAINT using dynamic masks (these mask the regions of the detector which are shaded due to the pressure cell).[13, 18] For ZIF-65, omission of shaded reflections, absorption correction and merging of data were carried out in a three-step process, firstly with the program SHADE, SADABS and finally XPREP.[14, 19, 20] For ZIF-90, as the crystals were twinned, data reduction was carried out using SHADE, TWINABS and XPREP.

Crystal Structure Refinements. Structure refinements were carried out in CRYSTALS.[21] The starting structure for refinement was taken from the ZIF-8 structure deposited in the CSD (refcode VELVOY).[2] All structures were refined anisotropically against F^2.[22] All 1,2 and 1,3 distances for the imidazole linker were restrained (ensuring the aromatic geometry of the ring was not

distorted) whilst all torsion angles and metal – ligand bond distances were allowed to freely refine. Vibrational and thermal similarity restraints were also applied to the organic linker. Hydrogen atoms on the linker were placed geometrically and constrained to ride on their host atoms. The pore volume and electron count per unit cell were calculated using the SQUEEZE algorithm within PLATON using a probe radius and step size of 1.2 Å and 0.7 Å, respectively.[23]

3.4 DFT geometry optimisation and single point energy calculations

These calculations were used to determine the energy barrier to the imidazole ring rotation for each framework. All calculations were performed using the CASTEP (version 5.11) simulation package.[24] The Hamiltonian operator was approximated using the Perdew-Burke-Ernzerhof (PBE) exchange-correlation functional, with the molecular wavefunction description provided by 'on-the-fly' pseudopotentials and a plane wave basis set operating at 650 eV, which gave convergence of the energy to within 4 meV per atom. The electronic structure was sampled at the gamma position only in the Brillouin zone due to the large size of the primitive unit cell (resulting in a k-point sampling grid of no greater than 0.06 $Å^{-1}$). Before carrying out single point energy calculations of the functionalised imidazole ring rotation, the ambient crystal structures of the three frameworks were geometry optimised without any symmetry constraints to allow both the relaxation of the atomic positions and the unit cell parameters. The potential energy surface was searched for energy minima by means of the Broyden-Fletcher-Goldfarb-Shanno (BFGS) algorithm.[25] Structures were considered to be optimised when the energy per atom, maximum force, maximum stress, and maximum atomic displacement

converged to the values of 0.02 meV atom^{-1}, 0.05 eV Å^{-1}, 0.1 GPa, and 0.002 Å, respectively. Once optimised, the co-ordinates of the respective imidazole linker were rotated through five degrees increments from ambient to 30°, at each interval single point energy calculations were carried out at the same level of theory to the geometry optimisation.

The optimised structures confirmed that the functionals used were appropriate as their root mean squared deviation (rmsd) and fluctuations in volume from the original crystal structures were minimal, in addition the geometry of the ligands around the metal centre were sensible (see **Figure 3.4**).

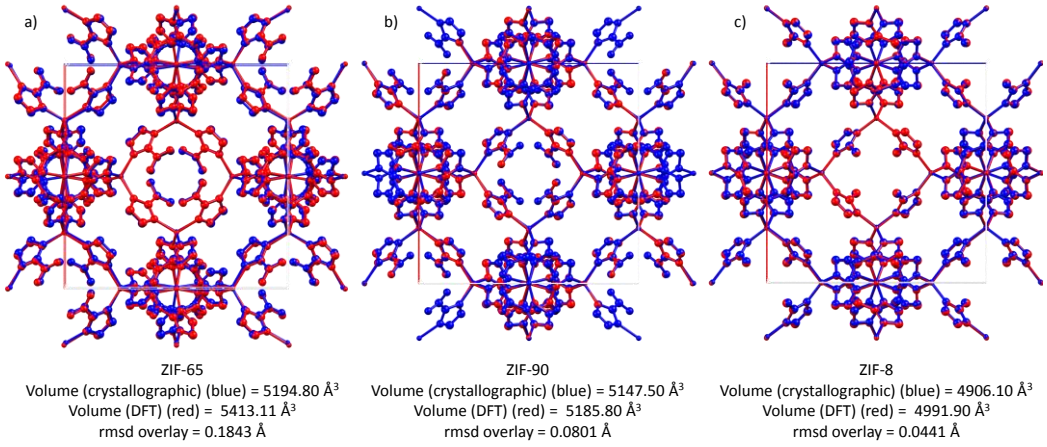

Figure 3.4: Overlays of the crystal structures (blue) with the DFT optimised structures (red) for (a) ZIF-65, (b) ZIF-90 and (c) ZIF-8. Note the small rmsd values and small percentages in volume changes which would be expected from a material with intrinsic flexibility.

3.5 Grand canonical Monte Carlo simulations

Grand canonical Monte Carlo (GCMC)[26] simulations were performed in order to study methanol adsorption in ZIF-8, ZIF-65 and ZIF-90 using the multipurpose code MuSiC.[27] In GCMC simulations, the framework atoms must be fixed at their crystallographic positions. For each ZIF, different

simulations were carried out using high-pressure crystallographic structures to capture the effect of framework rotation with respect to increasing pressure during the adsorption process. Standard Lennard-Jones (LJ) 12-6 potentials were used to model the interatomic interactions between the framework and methanol. Apart from LJ interactions, electrostatic interactions were included between methanol molecules using the Wolf summation.[28] The parameters for the framework atoms were obtained from the UFF force field.[29] Methanol was modelled using the TraPPE potential.[30] The Lorentz-Berthelot mixing rules were employed to calculate fluid/solid parameters. Interactions beyond 15 Å were neglected. 10^7 Monte Carlo steps were performed, the first 40 % of which were used for equilibration, and the remaining steps were used to calculate the ensemble averages. To calculate the gas-phase fugacity the Peng-Robinson equation of state was used.[31]

3.6 *Results and discussion*

3.6.1 *The Response of ZIF-90 and ZIF-65 to high-pressure*

The results of the variation of unit cell volume and the evolution of the angle θ (described in the introduction to this chapter, see **Section 3.1.1**) for both ZIF-65 and ZIF-90 in MeOH:EtOH (4:1) are shown below and compared to the previously collected data for ZIF-8 (see **Figure 3.5**). In addition the resulting pore content (in electrons per unit cell (e-/uc)) and solvent accessible volume for each crystal structure were calculated using the SQUEEZE algorithm within PLATON (**Figure 3.6**).

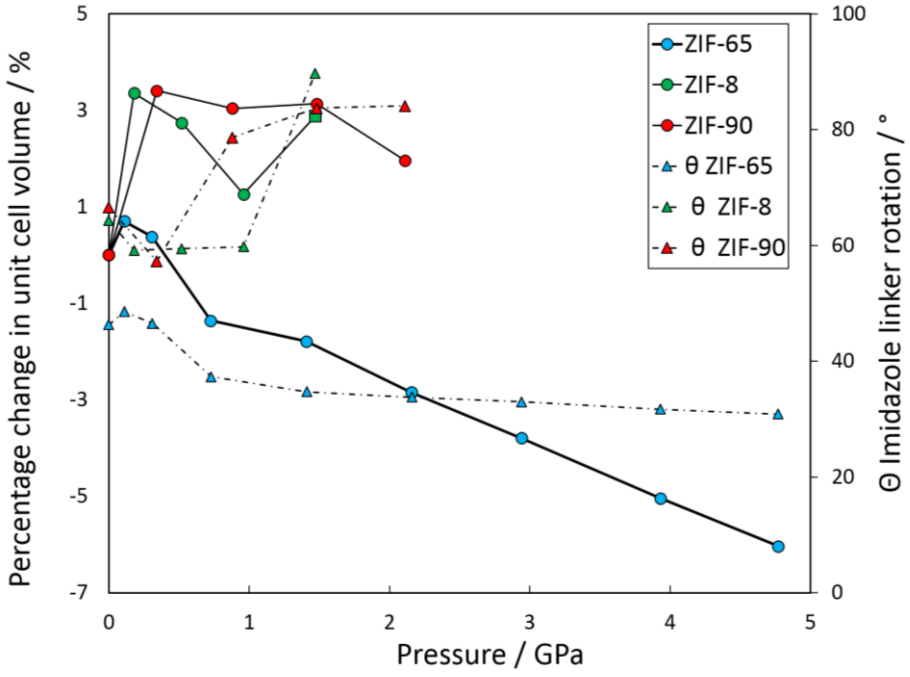

Figure 3.5: Left hand axis (circle markers, bold lines) shows evolution of pressure with volume for ZIF-8 (green), ZIF-90 (red) and ZIF-65 (blue) in MeOH:EtOH (4:1). Right hand (triangle markers, dashed lines) axis shows evolution of θ. ZIF-8 data shown from original study by Moggach *et al.* [1]

For ZIF-90, on increasing pressure to 0.34 GPa, the unit cell volume increased by 3.56%, resulting in an increase in pore size of 300 Å^3 **(Figure 3.6**) while θ decreased by 9.3° (from 66.5° to 57.2°). This small decrease of θ coincided with a decrease in electron density in the pores (from 981 to 238 e-/uc, **Figure 3.6a**). This is probably due to the crystal desolvating between the ambient pressure X-ray measurement and loading into the DAC. Upon increasing pressure further to 0.88 GPa, the unit cell compressed by 0.53%. This coincided with a large increase in θ (from 21.3° to 78.6°), and a transformation to the HP phase (hereafter referred to as ZIF-90HP), as observed previously in ZIF-8. Further increasing pressure to 1.95 GPa, θ continued to increase (to 84.06°), where the pore volume and content reached a maximum, measuring 2612 Å^3 and 1087 e-/uc respectively (**Figure 3.6a**).

In the previous high-pressure study of ZIF-8 when compressed using MeOH:EtOH, θ decreased from 64.3° to 59.1° and then increased to 59.7° when the pressure increased from 0 to 0.18 and then to 0.96 GPa, respectively.[1] Increasing pressure further to 1.47 GPa saw θ increase to 89.7° and coincided with the framework transforming to ZIF-8HP (**Figure 3.2**). The behaviour in ZIF-90 observed here is somewhat similar to ZIF-8 however the increase in pore volume, and consequent pore content, is larger at 1.96 GPa (~300 Å^3 and 1087 e$^-$/uc) compared to 1.47 GPa ZIF-8HP (~100 Å^3, and ~636 e$^-$/uc). The maximum value of θ for ZIF-90HP at 1.96 GPa was also slightly less than that of ZIF-8HP at 1.47 GPa (84.1° compared to 89.7°), however, as the -CHO group lies in the plane of the MeIm linker (unlike the -CH_3 group in ZIF-8), the 4MR window is actually larger in ZIF-90HP than ZIF-8HP (see **Figure 3.7** and **Table 3.2**).

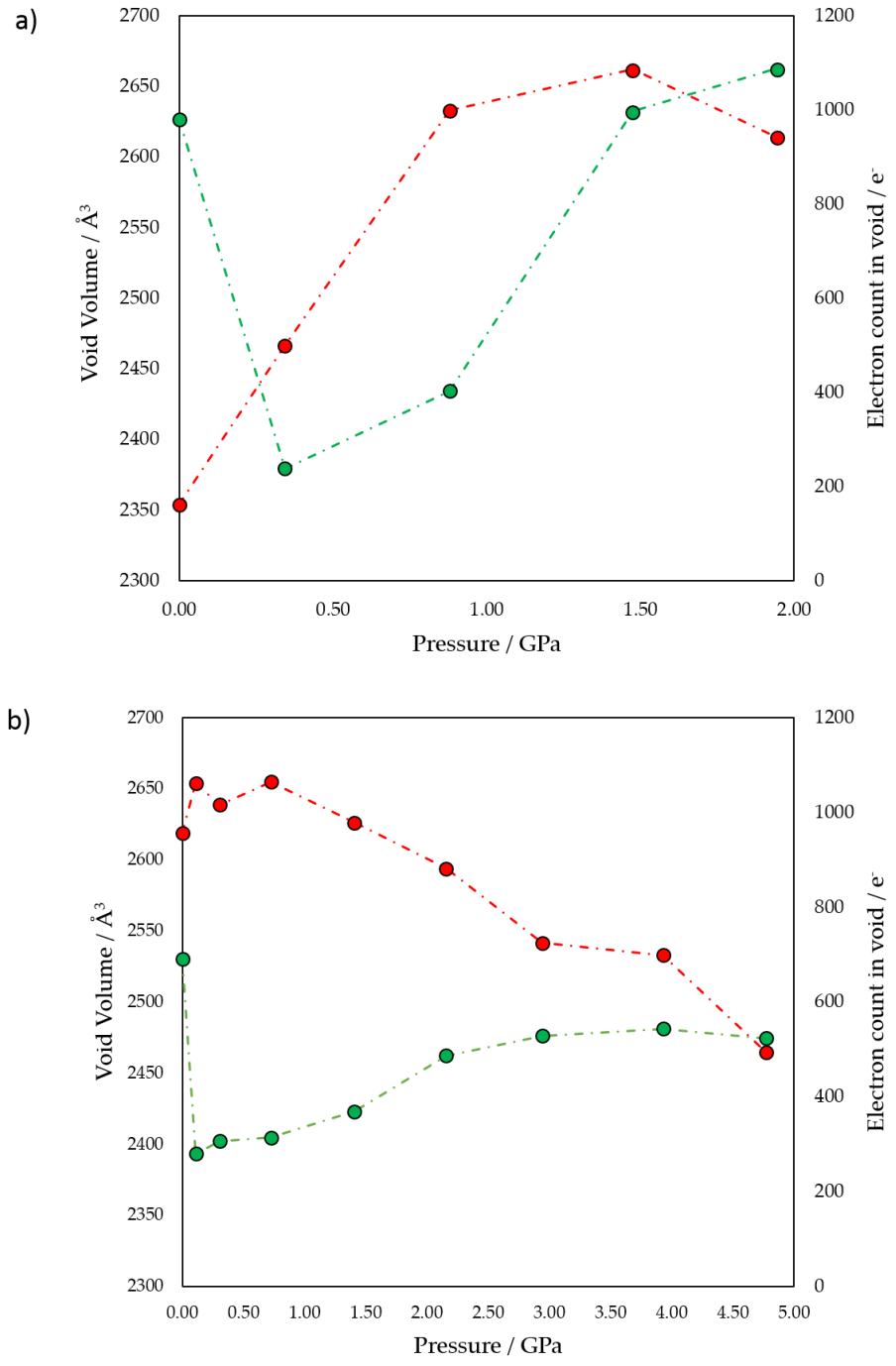

Figure 3.6: PLATON SQUEEZE data showing void volume and pore content for (a) ZIF-90 and (b) ZIF-65 as a function of pressure. Red (left hand axis) shows evolution of void volume, and green (right hand axis) shows electron count in the void (in electrons per unit cell, e-/uc).

For ZIF-65, on increasing pressure to 0.11 GPa, the unit cell volume expands by 0.7% which is indicative of the MeOH:EtOH medium penetrating into the crystal.[32] This increase in electron density in the pores is accompanied by an increase in void volume of ~50 $Å^3$,which occurs due to a rotation of the NO_2Im groups, where θ increased from 46.3° to 48.5° (in contrast to ZIF-8 and ZIF-90 where at similarly low pressures θ decreases). This rotation causing the 4MR window to increase from 0.8 to 1.0 Å, while the 6MR window remains unchanged (**Table 3.2**).

Table 3.2: 4MR and 6MR window diameters of ZIF-8, ZIF-65 and ZIF-90 at pressure.

ZIF-8 in MeOH/EtOH Pressure / GPa	4MR diameter / Å^3	6MR diameter / Å^3	ZIF-65 in MeOH/EtOH Pressure / GPa	4MR diameter / Å^3	6MR diameter / Å^3	ZIF-90 in MeOH/EtOH Pressure / GPa	4MR diameter / Å^3	6MR diameter / Å^3
0	0.8	3.0	0	0.8	3.2	0	1.4	3.2
0.18	0.6	3.0	0.11	1.0	3.2	0.14	1.2	3.2
0.52	0.6	3.0	0.30	1.0	3.2	0.34	1.0	3.2
0.96	0.6	3.0	0.73	0.6	3.6	0.88	2.4	3.4
1.47	2.2	3.6	1.40	0.6	3.6	1.47	2.6	3.6
			2.15	0.4	3.6	1.95	2.4	3.6
			2.94	0.4	3.8			
			3.93	0.4	3.8			
			4.77	0.4	3.8			

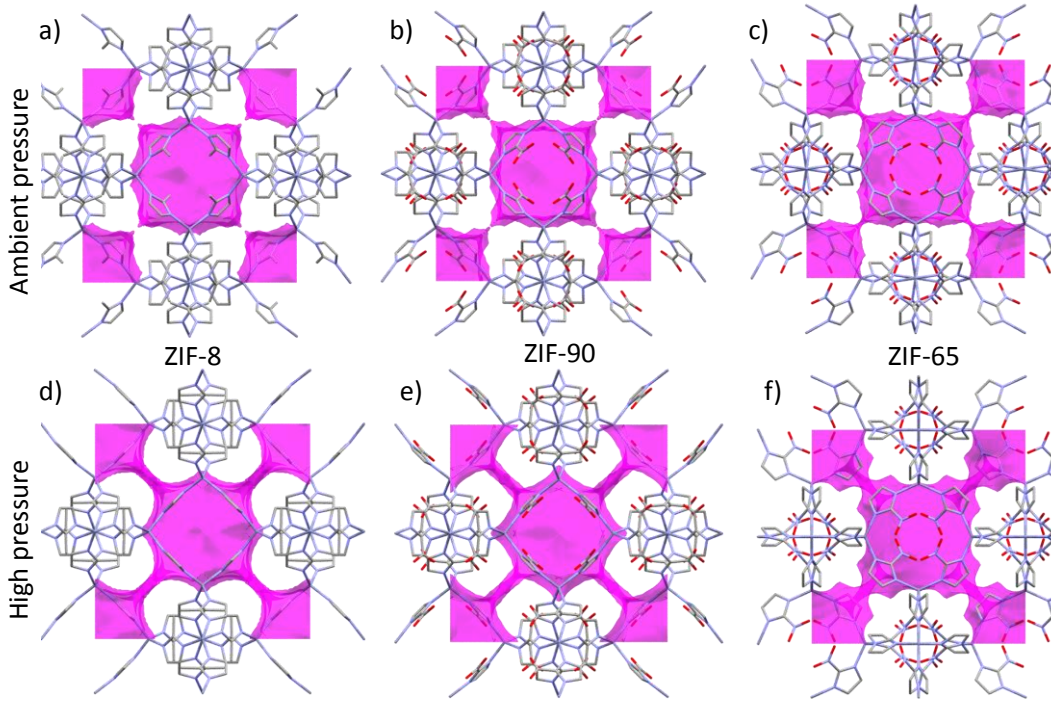

Figure 3.7: Capped stick diagrams for (a) ZIF-8, (b) ZIF-90 and (c) ZIF-65 at ambient pressure and (d) ZIF-8, (e) ZIF-90 and (f) ZIF-65 in their respective HP forms at 1.47 GPa, 1.95 GPa and 4.77 GPa respectively. Purple shading represents the solvent accessible volume calculated with a probe size diameter of 3.4 Å (kinetic diameter of methanol) using Mercury. Note the increase in size of the channels linking the central nanopore through the 6MR windows on undergoing the transition.

On increasing pressure further in ZIF-65, the framework undergoes compression in a two-step process. The first step occurred between 0.11 to 0.73 GPa, where the unit cell volume decreased by 2%, and was accompanied by a large decrease in θ (from 48.6° to 36.9°). This corresponded to a closing of the 4MR windows as the window diameter decreased from 1.0 to 0.6 Å, while the 6MR window diameter increased from 3.2 to 3.6 Å. The second step of

compression occurred between 0.73 and 4.77 GPa, where θ remained approximately constant over the entire pressure range (reflected in the constant 4MR and 6MR window diameters), with the compression of the framework almost linear (**Figure 3.5**). A gradual decrease in void volume occurred between 0.11 to 4.77 GPa, which coincided with a compression of the unit cell volume, however the electron count in the void steadily increased from 0.11 GPa to 3.10 GPa (from 280 to ~ 540 e^-/uc). From 3.10 GPa to 4.77 GPa (which marked the highest pressure point for which diffraction data could be collected and solved (giving rise to the structure hereafter referred to as ZIF-65HP)) the electron density in the pores reached a plateau, whilst the void and unit cell volume slowly decreased (**Figure 3.6**). ZIFs are often observed to become amorphous on direct compression, and have been predicted to be rather unstable on applying pressure.[33, 34] The inclusion of solvent here would appear to stabilise ZIF-65 to external pressure, which has been seen in other MOFs such as CuBTC and MOF-5.[32, 35]

At 4.77 GPa, the structure of ZIF-65HP does not resemble that of ZIF-8HP, as the NO_2Im groups rotate to lower θ values (30.9 ° compared to 89.7 ° in ZIF-8HP).[1] Rotation of the NO_2Im ligands results in the NO_2 groups becoming closer together, reducing the size of the four membered ring window. This is characterised by an ever decreasing θ angle in ZIF-65 with increasing pressure, suggesting strong intermolecular N…O interactions within the framework from the pendant NO_2 groups. This can be quantified by measuring the N…O intermolecular distances (N(1)'…O(1) or N(2)'…O(1), where N(1)' and N(2)' are symmetry related to N(1) and N(2), respectively through the two-fold (x, -y, -z) operation) across the 4MR window (**Table 3.3** and **Figure 3.8**). For example, the N(2)…O(1) distance decreases by 0.577 Å (from 3.568(4) to

2.991(10) Å) between ambient pressure and 4.77 GPa. The intermolecular interaction energy between stacked nitro groups over the distance range 2.4 to 3.4 Å were once thought to be weak or even repulsive, however in certain geometries (usually interactions which include NO_2 groups perpendicular to each other) they can have similar interaction energies comparable to C=O…H-C interactions.[36, 37] Thus it would appear that the application of pressure most likely increases the interaction between the nitro groups, which in turn prevents ZIF-65 from undergoing the high-pressure phase transition as observed in both ZIF-8 and ZIF-90. The net result is a framework that favours the formation of close contacts between the ligands, blocking the 4MR window while the nanopore contracts and the guest molecule concentration increases.

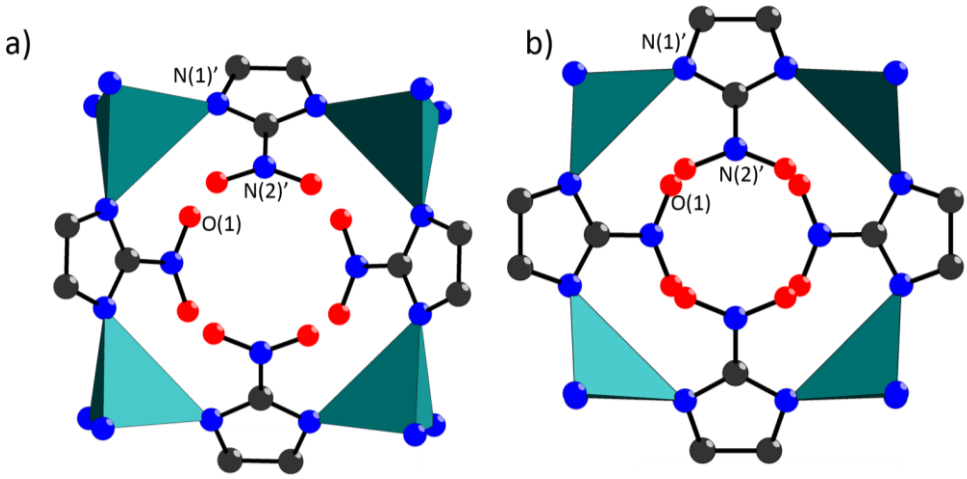

Figure 3.8: 4MR window in ZIF-65 as viewed down the *a*-axis at (a) ambient pressure and (b) 4.77 GPa.

Table 3.3: Selected distances in ZIF-65 crystal structures at pressure.

Pressure (GPa)	O(1) … N(2)′ (x, -y, -z) (Å)	O(1) … N(1)′ (x,-y, -z) (Å)
0	3.568(4)	2.948(4)
0.11	3.655(6)	2.960(5)
0.31	3.575(6)	2.957(5)
0.73	3.205(8)	3.002(7)
1.41	3.151(8)	3.003(8)
2.16	3.088(9)	2.976(9)
2.94	3.039(9)	2.974(9)
3.93	3.024(9)	2.974(9)
4.77		2.976(10)

3.6.2 The effect of pressure and pressure transmitting media on ligand rotation in ZIF-8, ZIF-90 and ZIF-65

In order to determine the role of the pressure transmitting media in the formation of the HP phases and ligand rotation, single point energy calculations were undertaken on guest-free ZIF-8, ZIF-90 and ZIF-65, where after geometry optimisation of the ambient pressure structures using the periodic CASTEP code, the imidazolate linkers were rotated (i.e. θ varied) by 30° (in 5° increments) in both positive and negative directions from the equilibrium structures (**Figure 3.9** and **Table 3.4**). Note, energies are given in $kJmol^{-1}$ per imidazolate linker, and reported as relative values with respect to

the equilibrium structure. The geometry optimised ground state structures gave values of θ comparable to the ambient pressure values, measuring 63.4°, 55.5°, 50.2° for ZIF-8, ZIF-90 and ZIF-65 respectively compared to the ambient crystal structure values of 64.3°, 66.5° and 46.5°. A slight variation for ZIF-90 and ZIF-65 values could be attributed to the presence of solvent in the pores of the experimental MOF data, which could cause the linkers to rotate from their ambient pressure values, whereas the computational model was solvent free and the model had been allowed to fully relax with respect to the electronic structure. In addition, the relatively flat potential energy surfaces revealed by the computational study indicates that barriers to rotation of the linkers around this global minima states are very low.

For ZIF-8 (which had a starting θ of 64.3°), the barrier to rotation of the MeIm linker to the ZIF-8HP phase (where θ = 89.7°) was relatively small (1.8 kJ mol^{-1}), however the same relative rotation of 25° in the opposite direction had a much larger energy penalty, equating to 48 kJ mol^{-1}. The rotation of the linker clearly has a definite preference, and in order for the opposite rotation to occur, the energies of adsorption would have to be very large, much larger than what might be expected for adsorption of MeOH which is usually in the order of tens of kJ mol^{-1}.[38]

For both ZIF-90 and ZIF-65, the potential energy landscape determined was relatively flat in comparison to ZIF-8, with only a small energy penalty of a few kJ mol^{-1} regardless of the direction of rotation. On compressing ZIF-90, the imidazole rings rotated by approximately +20°. This equated to an energy penalty of just 1.5 kJ mol^{-1}. The corresponding backward rotation equated to

1.9 kJ mol^{-1}. Similarly, for ZIF-65, the highest degree of rotation was -20° at 4.77 GPa, which equated to 6.4 kJ mol^{-1}, the corresponding forward rotation was more favourable at 1.4 kJ mol^{-1}. For all three frameworks, positive rotations are favoured in the absence of any guests. The negative rotations observed in the high-pressure experiments for ZIF-65 therefore indicate a much greater guest-host interaction than for ZIF-90 and ZIF-8, and one which becomes even more favourable on increasing pressure. It is well-known that the adsorption sites of ZIFs are located around the linkers and not the metal centres,[39] therefore this data suggests that as the guest molecules in ZIF-65 are pushed closer to the linkers on increasing pressure, more favourable interactions are formed, which are not present in either ZIF-8 or ZIF-90. This also tallies with the long-standing knowledge that the functionality of the imidazolate group can increase the energy of adsorption.[39] Thus the combination of the HP experiments and the DFT modelling work therefore appear to offer an explanation for the differing behaviour of ZIF-65 compared to ZIF-8 and ZIF-90.

Table 3.4: *Results of single point energy calculation of ZIF-8, ZIF-90, ZIF-65 when θ is varied in 5 degree steps to explore the relative rotations from -30 to +30 degrees. Energies are shown in kJmol^{-1}*

ZIF-65			ZIF-90			ZIF-8		
relative rotation (°)	absolute rotation θ (°)*	energy per linker (kJ mol^{-1})	relative rotation (°)	absolute rotation θ (°)*	energy per linker (kJ mol^{-1})	relative rotation (°)	absolute rotation θ (°)*	energy per linker (kJ mol^{-1})
-30	15.1	37.9	-30	25.5	4.4	-30	33.5	93.6
-25	20.1	15.1	-25	30.5	3.0	-25	38.5	41.0
-20	25.1	6.4	-20	35.5	1.9	-20	43.5	14.0
-15	30.1	3.1	-15	40.5	1.0	-15	48.5	4.4
-10	35.1	1.9	-10	45.5	0.5	-10	53.5	1.2
-5	45.1	1.6	-5	50.5	0.1	-5	58.5	0.1
0	50.1	0.0	0	55.5	0.0	0	63.5	0.0
5	55.1	1.6	5	60.5	0.0	5	68.5	0.2
10	60.1	1.5	10	65.5	0.1	10	73.5	0.5
15	65.1	1.4	15	70.5	0.5	15	78.5	0.9
20	70.1	1.4	20	75.5	1.5	20	83.5	1.3
25	75.1	1.5	25	80.5	4.1	25	88.5	1.8
30	80.1	1.9	30	85.5	6.6	30	93.5	2.3

*Absolute rotation refers to the angle θ defined as the angle the 100 hkl plane makes with the Im linker.

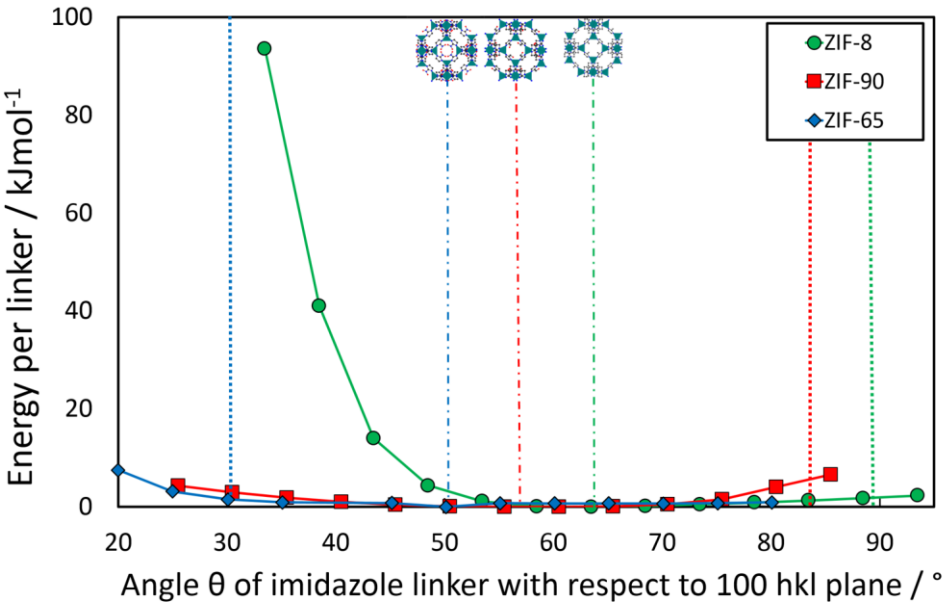

Figure 3.9: Single point energy calculations showing the energy landscape of the rotation of Im ligands for ZIF-8, ZIF-90 and ZIF-65. Dashed lines denote the ambient pressure phase angle of rotation and dotted lines denote the high-pressure angle of rotation.

3.6.3 Grand canonical Monte Carlo simulations of methanol in ZIF-8, ZIF-65 and ZIF-90

In order to locate the position of guest MeOH molecules, and to quantify guest-host interactions for ZIF-8, ZIF-65 and ZIF-90, Grand Canonical Monte Carlo (GCMC) calculations were carried out. As GCMC simulations require the frameworks to be rigid, the high pressure crystallographic structures were used as models in separate GCMC simulations. In this way, the effect of changing the linker orientation on the uptake of methanol into the pores can be directly studied. During the simulations, the energies and positions of the methanol molecules were stored, and from this interaction energy histograms constructed (**Figure 3.10**).

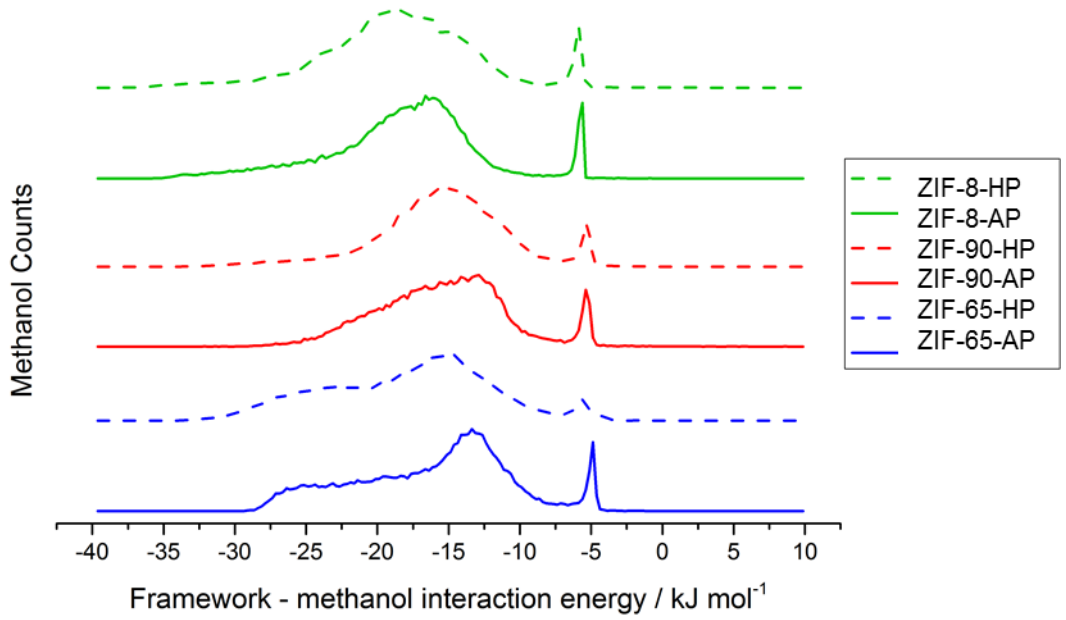

Figure 3.10: Interaction energy histograms obtained from the highest loading of methanol in ZIFs from GCMC simulations. AP (dashed lines) and HP (bold lines) refer to the ambient and high-pressure structures, respectively.

Compared to the AP structures, the guest-host interaction energies for all HP structures decreased, that is, became more favourable. The driving force for the HP phases, for all systems studied, is therefore to maximise the interaction between the framework and the adsorbate. ZIF-65 was also found to have the strongest interaction with methanol (≈-35 kJ mol^{-1} compared to ≈-30 kJ mol^{-1} for ZIF-8 and ZIF-90).

In order to understand the effect that the guest-host interactions had on the direction of rotation, GCMC simulations were also undertaken on hypothetical structures of ZIF-90 and ZIF-65 where the linkers were rotated by the same degree but in the opposite direction to their HP experimental structures. For example, in ZIF-65-HP, the linkers rotate by -20° compared to

the ambient pressure phase, so the linkers in the hypothetical structure (named ZIF-65-HYPO) were rotated by +20°. Likewise, the ICA linkers in ZIF-90-HP rotate by + 25°, so the linkers in ZIF-90-HYPO were rotated by -25°. **Figure 3.11** and **3.12** show the resulting methanol – framework interaction energy histograms for the hypothetical phases as well as for the HP phases of ZIF-65 and ZIF-90, respectively. In addition to the histograms, the centres of mass of each methanol molecule for each energy range is shown (as colour-coded spheres, with respect to interaction energy) within the respective framework.

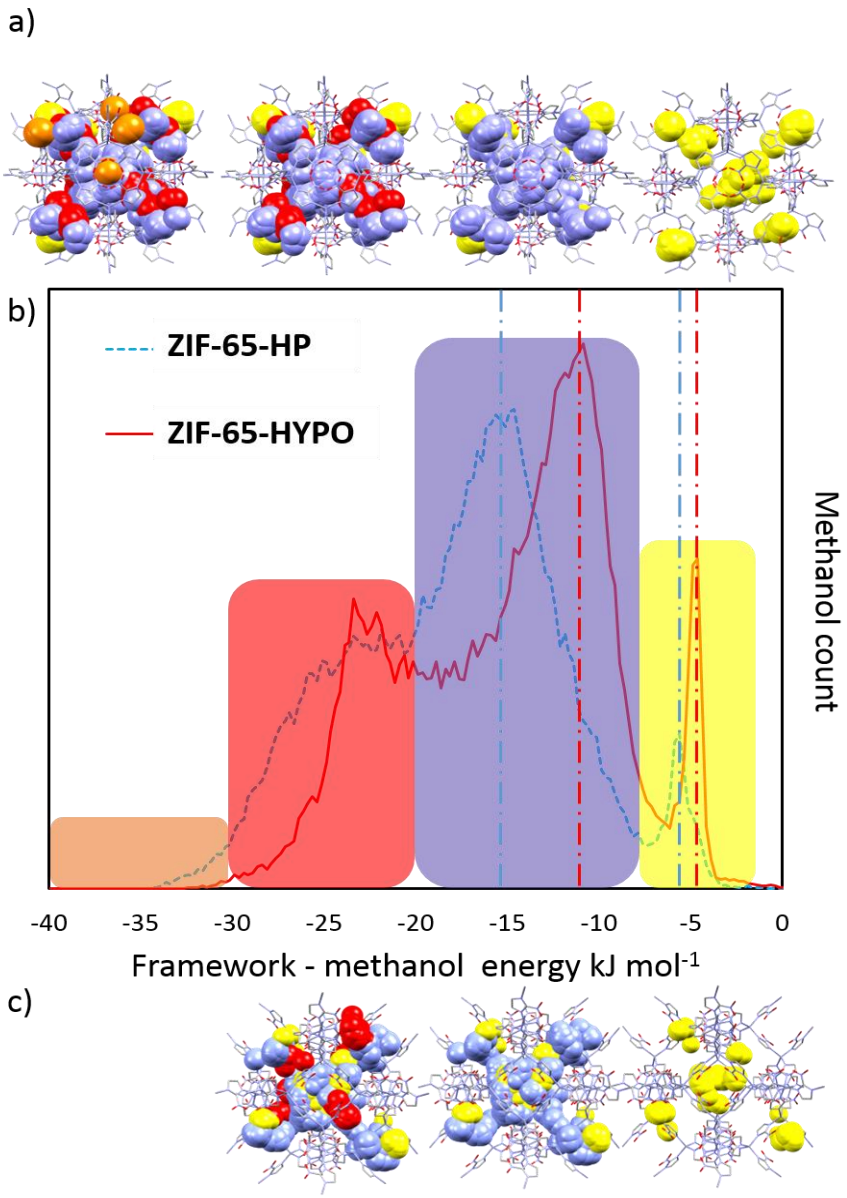

Figure 3.11: (a) ZIF-65-HP model showing centres of mass of methanol as a function of their interaction energy with the framework. (b) Methanol – framework interaction energy histograms for ZIF-65-HP (blue, dashed line) and ZIF-65-HYPO (red, bold line). The section colours correlate with the centre of mass of methanol. Dot dash vertical lines indicate maxima of histogram peaks, where blue = ZIF-65-HP and red = ZIF-65-HYPO. (c) ZIF-65-HYPO models showing the centres of mass of methanol of molecules as a function of their interaction energy with the frameworks. Where orange - -40 to -30 kJ mol^{-1}, red - -30 to -20 kJ mol^{-1}, blue - -20 to -8 kJ mol^{-1}, yellow - -8 to 0 kJ mol^{-1}. Hydrogen atoms are omitted for clarity.

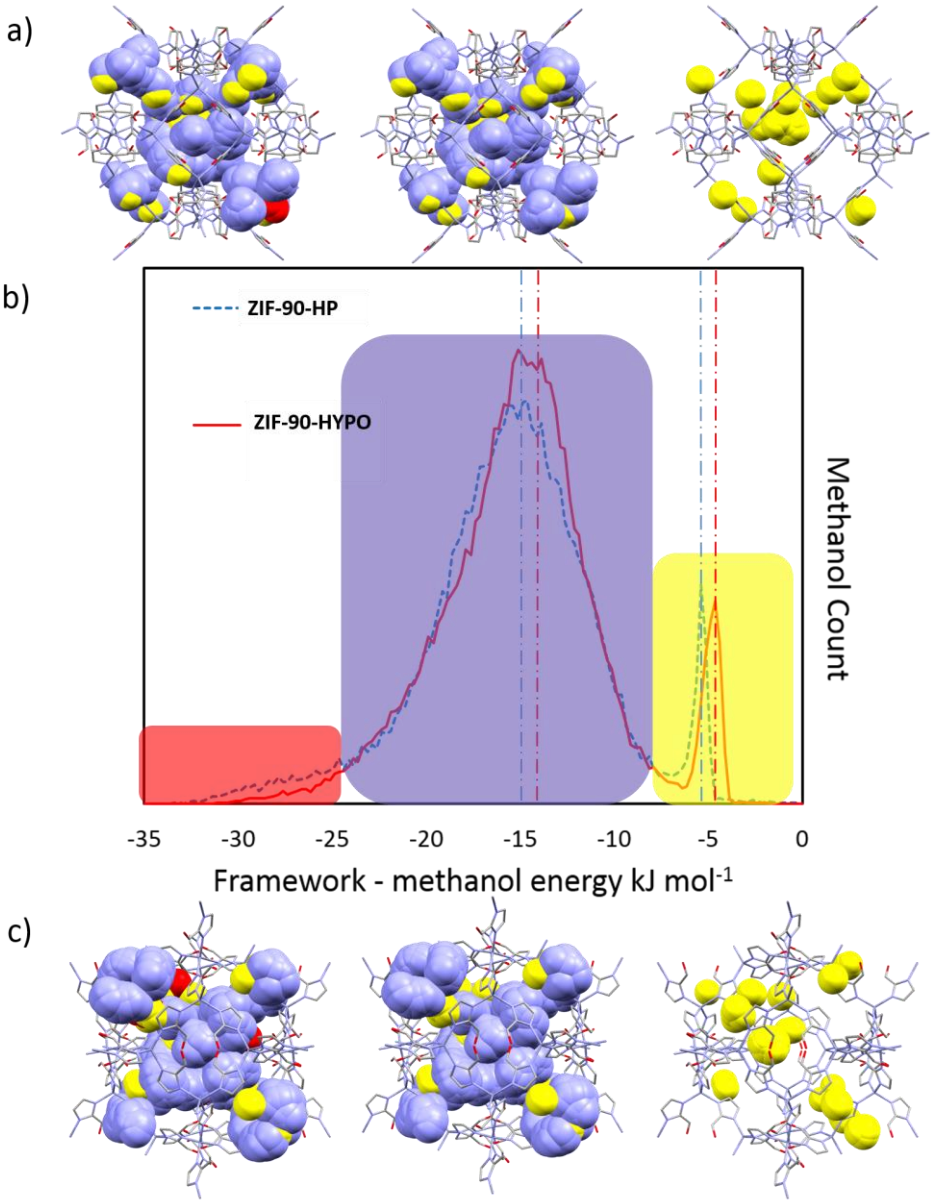

Figure 3.12: (a) ZIF-90-HP models showing the centres of mass of the methanol molecules as a function of their interaction energy with the framework. (b) Methanol – framework interaction energy histogram for ZIF-90-HP (blue, dashed lines) and ZIF-90-HYPO (red, bold line). Dot-dash vertical lines indicate maxima of histogram peaks, where blue = ZIF-90-HP and red = ZIF-90-HYPO. (c) ZIF-90-HYPO models showing the centres of mass of methanol of molecules as a function of their interaction energy with the frameworks. Where red - -35 to -25 kJ mol^{-1}, blue - -25 to -10 kJ mol^{-1}, yellow - -10 to 0 kJ mol^{-1}. Hydrogen atoms are omitted for clarity.

In both ZIF-90-HYPO and ZIF-65-HYPO, the interaction energy between methanol and the framework increases (i.e. becomes less favourable) compared to the experimentally observed structures. Thus it would appear that it is the guess-framework energies that dictate the direction of ligand rotation. Whilst this is much more apparent in ZIF-65 than in ZIF-90, both demonstrate that the framework-guest interaction is very important. As the PES of the framework rotation is very flat, the rotation direction must be dictated by the most favourable interactions i.e. those with the lowest energy (-40 to -25 kJ mol^{-1}).

Analysing the position of the methanol molecules in the pores at each peak of the interaction energy histogram sheds light on the differences of packing within the structures, and why each high-pressure structure was preferred over their hypothetical counterpart. **Figure 3.11a** and **c** and **Figure 3.12a** and **c** show space filling diagrams as a function of increasing energy to highlight the positions of the guests for ZIF-65-HYPO, ZIF-65-HYPO, ZIF-90-HP and ZIF-90-HYPO, respectively, to help interpret the differences in structure. For ZIF65-HP the most favourable interaction of methanol with the framework was located just above the four-membered window, interacting strongly (-40 to -30 kJ mol^{-1}) with the four overlapping NO_2 groups (**Figure 3.11**). The second strongest sites, in red (-30 to -20 kJ mol^{-1}), flowed through the 6MR windows. The third strongest site, in blue (-20 to -10 kJ mol^{-1}), was also present in the 6MR window, along with the red sites and many sites that filled up in the centre of the pore. The final site, in yellow (-10 to 0 kJ mol^{-1}) was found in the central pore, and with no defining interaction with framework accounts for the low interaction energy these methanol molecules experience with ZIF-65.

For ZIF-65-HYPO, there was no methanol –framework interaction energy below -30 kJmol^{-1}, which is most likely due to the orientation of the framework which is now in a gate-opened structure. With the 4MR window open, this orientation would not allow good contact with methanol. This resulted in the most favourable sites having energies in the order of -30 to -20 kJ mol^{-1} (shown in red in **Figure 3.11c**). These sites, like in ZIF-65-HP, sit in the 6MR window thereby connecting the pores throughout the crystal lattice, but with less favourable interaction energies (ca. 5 kJ mol^{-1} less) than in ZIF-65-HP. The second site, blue (-20 to -10 kJ mol^{-1}), was also present in the 6MR window and in the central pore, but the mean interaction energy is again around ~5 kJ mol^{-1} less than ZIF-65-HP. The weakest binding site in ZIF-65-HYPO, yellow (-10 to 0 kJ mol^{-1}) occupied the centre of the pore, and the density was much higher than in ZIF-65-HP. The fact that this site is on average populated more frequently illustrates that the structure of ZIF-65-HYPO is in a less favourable orientation for the uptake of methanol than ZIF-65-HP. In the case of ZIF-90, the hypothetical phase ZIF-90-HYPO also produces less favourable interaction energies with methanol than ZIF-90-HP. However, the interaction energies are much closer (~1 kJ mol^{-1} difference) compared to ZIF-65, where the offset between each phase is ~3 kJ mol^{-1} (**Figure 3.11** and **Figure 3.12**).

From this outcome for both systems, it is evident that the lowest energy sites (~-30 to -20 kJmol^{-1}) dictate the orientation of the framework, as these sites percolate from one pore to another through the 6MR windows. It therefore clear that increasing the limiting pore diameters of these windows is important for adsorption of methanol through the extended pore network. **Figure 3.13** and **Table 3.5** illustrate how ZIF-90-HP (θ = 84 °) has a larger 6MR window diameter than its rotated sister structure ZIF-90-HYPO (θ = 34 °); the case is

identical for ZIF-65-HP and ZIF-65-HYPO. For ZIF-65, understanding the difference in the interaction energy of methanol with each framework helps to explain why the framework would adopt a different geometry at high pressure to that of ZIF-8 and ZIF-90. The highly polar NO_2 four-membered window could form very strong interactions with methanol, which it could not do if it formed a "gate opened" structure like ZIF-8 or ZIF-90, in addition to creating larger channels for the methanol to percolate through the structure.

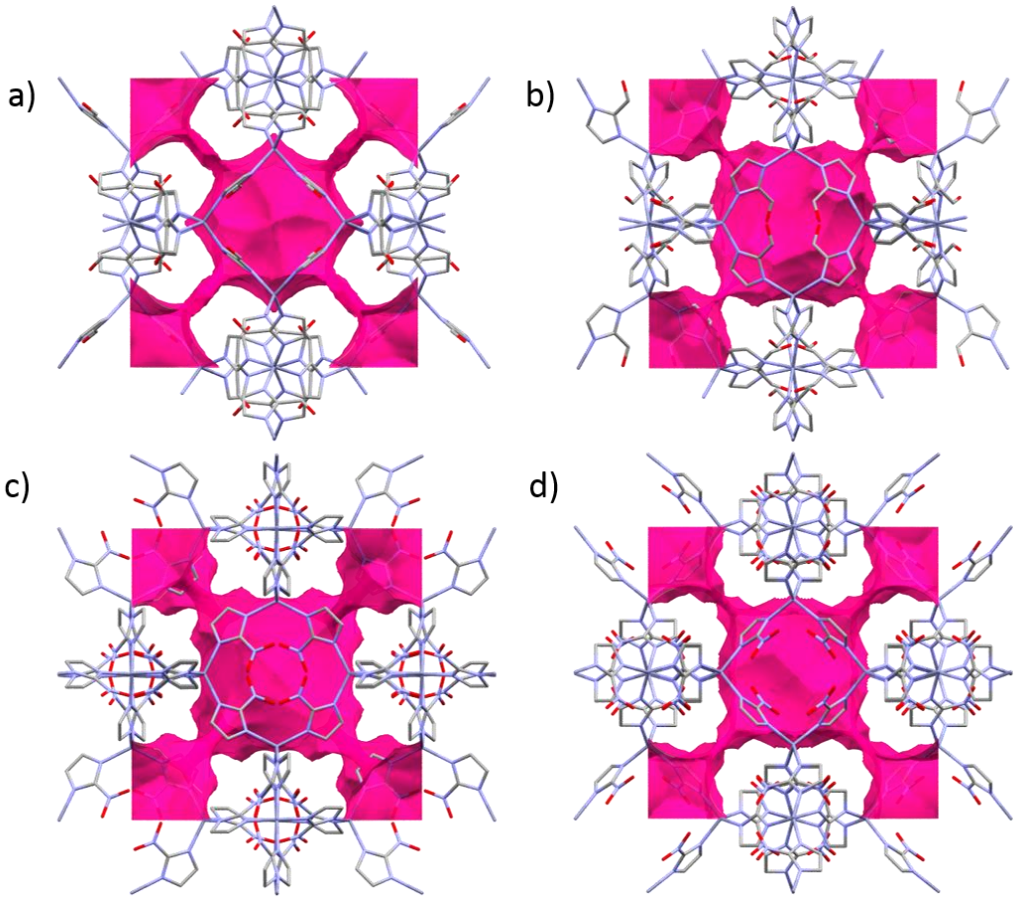

Figure 3.13: (a) ZIF-90-HP, (b) ZIF-90-HYPO, (c) ZIF-65-HP, (d) ZIF-65-HYPO. All viewed down the 100. Note in (b) and (d) the smaller channels in the six membered ring windows .

Table 3.5: Table of limiting pore diameters and θ angles of both HP and HYPO phases of ZIF-90 and ZIF-65.

Framework	θ/ °	4MR window diameter / Å	6MR window diameter/ Å
ZIF-65-HP	30	0.4	3.8
ZIF-65-HYPO	70	2.0	3.6
ZIF-90-HP	84	2.4	3.6
ZIF-90-HYPO	34	0	3.2

3.7 Conclusions

In summary, this chapter has illustrated that the gate-opening nature of ZIFs at high pressure applies to a wide range of functionalised ZIFs. It has been demonstrated that the functionality of the imidazole ring dictates the pressure of the transition to a high-pressure phase, as well as the direction of rotation of the imidazolate linkers. By using an alcohol as the pressure transmitting liquid and by using groups of increasing polarity on the framework, the degree of rotation and the size of pores can be controlled. It has been shown that ZIF-90 undergoes a phase transition to a gate open high-pressure phase, however the degree of rotation of the Im linker is less than that of ZIF-8. In addition, it was demonstrated that ZIF-65 undergoes a transition to a more gate-closed structure upon applying high-pressure. By carrying out DFT simulations of the framework response to ligand rotation, combined with GCMC simulations in the presence of methanol on the high-pressure structures of ZIF-65, ZIF-90 and ZIF-8, and their hypothetical counterparts where the direction of linker rotation is reversed, the guest-host interactions and framework rotation interactions have been deconvoluted. For future work, it would be of interest to investigate what effect the nature of the guest molecules have on rotation of the linkers in high-pressure experiments. For example, if a non-polar solvent, such as pentane, was used as the penetrating pressure transmitting medium, it would be interesting to see how this would affect the adsorption properties of the framework and the gate-opening phenomena.

3.8 References

1. S. A. Moggach, T. D. Bennett and A. K. Cheetham, *Angew. Chem. Int. Ed.*, 2009, **48**, 7087-7089.
2. K. S. Park, Z. Ni, A. P. Cote, J. Y. Choi, R. D. Huang, F. J. Uribe-Romo, H. K. Chae, M. O'Keeffe and O. M. Yaghi, *Proc. Natl. Acad. Sci. U.S.A.*, 2006, **103**, 10186-10191.
3. K. Eum, K. C. Jayachandrababu, F. Rashidi, K. Zhang, J. Leisen, S. Graham, R. P. Lively, R. R. Chance, D. S. Sholl, C. W. Jones and S. Nair, *J. Am. Chem. Soc.*, 2015, **137**, 4191-4197.
4. H. Bux, F. Y. Liang, Y. S. Li, J. Cravillon, M. Wiebcke and J. Caro, *J. Am. Chem. Soc.*, 2009, **131**, 16000-16001.
5. D. Fairen-Jimenez, S. A. Moggach, M. T. Wharmby, P. A. Wright, S. Parsons and T. Düren, *J. Am. Chem. Soc.*, 2011, **133**, 8900-8902.
6. D. Fairen-Jimenez, R. Galvelis, A. Torrisi, A. D. Gellan, M. T. Wharmby, P. A. Wright, C. Mellot-Draznieks and T. Duren, *Dalton Trans.*, 2012, **41**, 10752-10762.
7. W. Morris, C. J. Doonan, H. Furukawa, R. Banerjee and O. M. Yaghi, *J. Am. Chem. Soc.*, 2008, **130**, 12626-12627.
8. R. Banerjee, A. Phan, B. Wang, C. Knobler, H. Furukawa, M. O'Keeffe and O. M. Yaghi, *Science*, 2008, **319**, 939-943.
9. A. S. Huang and J. Caro, *Angew. Chem. Int. Ed.*, 2011, **50**, 4979-4982.
10. T. Jose, Y. Hwang, D. W. Kim, M. I. Kim and D. W. Park, *Catal. Today*, 2015, **245**, 61-67.
11. C. I. Yen, S. M. Liu, W. S. Lo, J. W. Wu, Y. H. Liu, R. J. Chein, R. Q. Yang, K. C. W. Wu, J. R. Hwu, N. H. Ma and F. K. Shieh, *Chem. Eur. J.*, 2016, **22**, 2925-2929.
12. A. S. Huang, Q. Liu, N. Y. Wang and J. Caro, *Microporous Mesoporous Mater.*, 2014, **192**, 18-22.
13. Bruker, ed. SAINT, Madison, Wisconsin, USA, 2007.
14. G. M. Sheldrick, University of Göttingen, Germany., 2008.
15. S. A. Moggach, D. R. Allan, S. Parsons and J. E. Warren, *J. Appl. Crystallogr.*, 2008, **41**, 249-251.
16. G. J. Piermarini, S. Block, J. D. Barnett and R. A. Forman, *J Appl Phys*, 1975, **46**, 2774-2780.
17. R. A. Forman, S. Block, J. D. Barnett and G. J. Piermari, *Science*, 1972, **176**, 284-&.
18. Bruker, ed. ECLIPSE, Madison, Wisconsin, USA, 2006.
19. S. Parsons, in *SHADE*, University of Edinburgh, Edinburgh, Scotland, 2004.
20. Bruker, ed. XPREP, Madison, Wisconsin, USA, 2004.
21. P. W. Betteridge, J. R. Carruthers, R. I. Cooper, K. Prout and D. J. Watkin, *J. Appl. Crystallogr.*, 2003, **36**, 1487-1487.

22. C. F. Macrae, I. J. Bruno, J. A. Chisholm, P. R. Edgington, P. McCabe, E. Pidcock, L. Rodriguez-Monge, R. Taylor, J. van de Streek and P. A. Wood, *J. Appl. Crystallogr.*, 2008, **41**, 466-470.

23. A. L. Spek, *J. Appl. Crystallogr.*, 2003, **36**, 7-13.

24. S. J. Clark, M. D. Segall, C. J. Pickard, P. J. Hasnip, M. I. J. Probert, K. Refson and M. C. Payne, *Z. Kristallogr.*, 2005, **220**, 567-570.

25. D. F. Shanno, *Math. Comput.*, 1970, **24**, 647.

26. D. Frenkel and B. Smit, Academic Press, San Diego, Second edn., 2002, pp. 1-638.

27. A. Gupta, S. Chempath, M. J. Sanborn, L. A. Clark and R. Q. Snurr, *Mol. Simul.*, 2003, **29**, 29-46.

28. D. Wolf, P. Keblinski, S. R. Phillpot and J. Eggebrecht, *J. Chem. Phys.*, 1999, **110**, 8254-8282.

29. A. K. Rappe, C. J. Casewit, K. S. Colwell, W. A. Goddard and W. M. Skiff, *J. Am. Chem. Soc.*, 1992, **114**, 10024-10035.

30. B. Chen, J. J. Potoff and J. I. Siepmann, *J. Phys. Chem. B*, 2001, **105**, 3093-3104.

31. D. Peng and D. B. Robinson, *Ind. Eng. Chem. Fundam.*, 1976, **15**, 59-64.

32. A. J. Graham, D. R. Allan, A. Muszkiewicz, C. A. Morrison and S. A. Moggach, *Angew. Chem. Int. Ed.*, 2011, **50**, 11138-11141.

33. A. U. Ortiz, A. Boutin, A. H. Fuchs and F. X. Coudert, *J. Phys. Chem. Lett.*, 2013, **4**, 1861-1865.

34. S. Cao, T. D. Bennett, D. A. Keen, A. L. Goodwin and A. K. Cheetham, *Chem. Commun.*, 2012, **48**, 7805-7807.

35. A. J. Graham, J. C. Tan, D. R. Allan and S. A. Moggach, *Chem. Commun.*, 2012, **48**, 1535-1537.

36. M. Daszkiewicz, *CrystEngComm*, 2013, **15**, 10427-10430.

37. K. Wozniak, H. Y. He, J. Klinowski, W. Jones and E. Grech, *J. Phys. Chem.*, 1994, **98**, 13755-13765.

38. M. F. de Lange, B. L. van Velzen, C. P. Ottevanger, K. J. F. M. Verouden, L. C. Lin, T. J. H. Vlugt, J. Gascon and F. Kapteijn, *Langmuir*, 2015, **31**, 12783-12796.

39. H. Wu, W. Zhou and T. Yildirim, *J. Am. Chem. Soc.*, 2007, **129**, 5314-5315.

-Chapter Four-

The Effect of Gas Loading ZIF-8

Under Extreme Pressure

4.1 Synopsis

This experimental chapter describes a new alternative approach to loading MOFs with gas molecules at high pressures. The technique, which uses liquefied gases as the PTM in a DAC, is demonstrated to have considerable advantages over other gas-loading methods when investigating host-guest interactions. Loading ZIF-8 with CH_4, Ar, O_2 or N_2 reveals the presence of six symmetry independent adsorption sites. Upon adsorption of the gases, the framework undergoes a phase transition to a high-pressure phase and the energy barrier to this transition can be calculated with periodic DFT. In addition, grand canonical Monte Carlo simulations are used to calculate the energy of each adsorption site for all the gases studied.

4.2 Introduction

An increased understanding of how porous metal organic frameworks (MOFs) interact with guest molecules of commercial interest is of vital importance for the further development and commercialization of MOFs in a wide range of applications including gas storage, catalysis and drug delivery.[1-3] Framework materials have been studied in depth, both experimentally and theoretically, with the intention of developing new materials with targeted properties. Yet frequently such studies present more questions than answers. Despite a vast library of synthesised and characterised MOFs, only a small number of these frameworks have been investigated extensively to correlate their structure with some of their unusual properties. ZIF-8 ($Zn_6(MeIm)_{12}$, MeIm = 2-methylimidazole) is one such material.[4] As discussed in Chapter Three, ZIF-8 is based on the zeolite sodalite topology, crystallising in the cubic space group (*I*-43*m* (*a*=16.9856(16) Å, V=4900.5(8) Å^3))[5] and contains one central

nano-sized pore per unit cell, with a volume of ≈2500 $Å^3$ and pore diameter of 11.6 Å. Connecting these large nanopores are eight six-membered ring (6MR) windows c.a. 3.4 Å in diameter, in the body diagonals of the unit cell, and six smaller four-membered ring (4MR) windows of c.a. 0.8 Å in the faces of the unit cell (**Figure 4.1**) ZIF-8 has been studied extensively using experimental and computational techniques,[6, 7] and was the first MOF in which gas loading studies using neutron powder diffraction (NPD) had been carried out.[8] In this NPD study, adsorption sites were found for D_2, however little to no structural changes occurred to the framework upon gas loading. A subsequent NPD study was undertaken on ZIF-8 with CD_4 in a comparative study with MOF-5 ($Zn_4O(BDC)_3$, BDC = 1,4-benzenedicarboxylate).[9] In MOF-5, preferential adsorption sites were located above the metal clusters, whereas in ZIF-8 they were above the organic linker. Attempts were made to model adsorption sites within the framework after a suspected transition to a new monoclinic supercell, but issues with data quality inhibited the refinement of all atomic positions of both the framework and guests. Difficulties obtaining atomistic quality structural data on guest molecules adsorbed into the framework is a common problem in the study of MOFs due to a number of factors such as the large void space, diffuse and partially occupied adsorption sites and weakly scattering guests. These issues, combined with experimental problems faced when using low pressure gas-cell apparatus, make the task of locating and quantifying adsorption sites with a high degree of confidence challenging.[10] This is one of the reasons why such few gas included framework structures have been reported in the Cambridge Structural Database (CSD), which on

first sight is peculiar considering that guest uptake plays such an important role in many of the potential applications of porous MOFs.

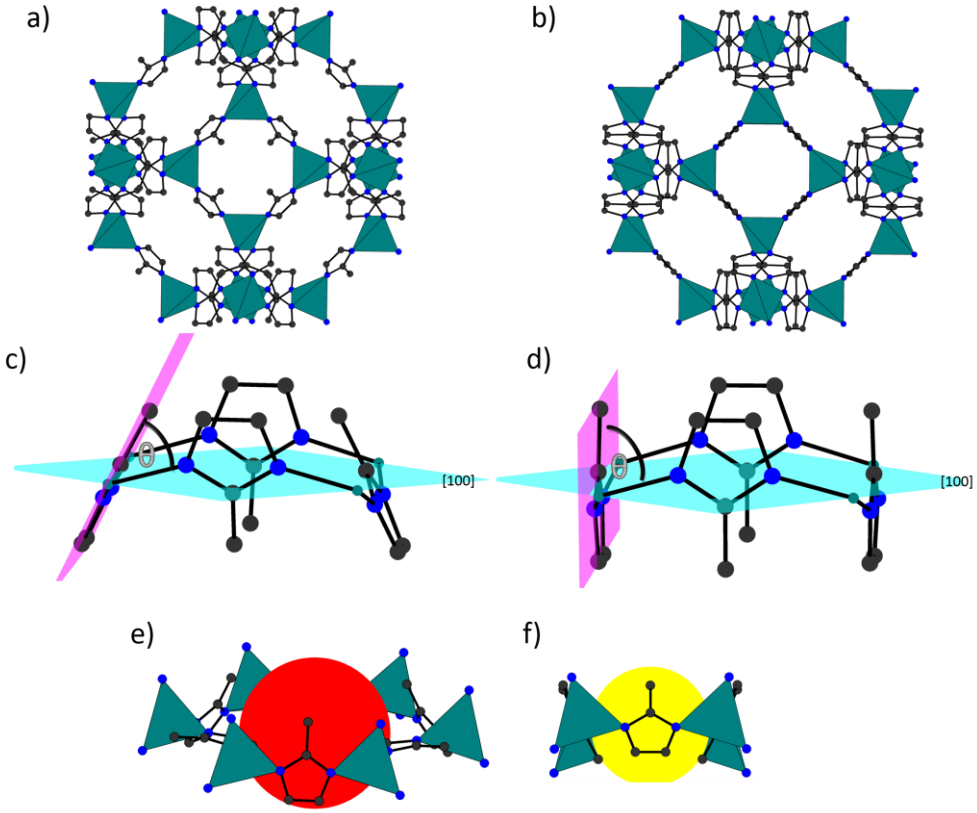

Figure 4.1: (a) ZIF-8-AP with 4MR window in the faces and 6MR windows in the body diagonal. (b) ZIF-8-HP with MeIm linkers rotated by 30° (c) 4MR window showing the opening angle of 68° for ZIF-8-AP, (d) 4MR window showing the opening angle of 89° for ZIF-8-HP, (e) 6MR window with pore diameter of 3.0 Å and (f) 4MR window with pore diameter of 0.8 Å.

An alternative to the experimental gas cell is the diamond anvil cell (DAC), which has induced new and unusual behaviour in porous materials through the application of GPa pressures. Examples include negative linear compressibility in cyanide-bridged frameworks,[11, 12] pressure-induced amorphisation of ZIFs,[13] and pressured induced phase transitions, as observed

in the high-pressure study of ZIF-8.[5] This latter study revealed previously unknown flexibility in the framework, where the sample underwent a second order phase transition to a new high pressure phase (ZIF-8HP) at 1.47 GPa, which was characterised by a re-orientation of the four and six membered imidazole rings, to form a "gate open" structure (**Figure 4.1**). The crystallographic determination of the transition to ZIF-8HP became invaluable in interpreting the adsorption mechanism for guest molecules in ZIF-8, with the ZIF-8HP phase being used to model a step in the N_2 adsorption isotherm at 77 K, indicating that the same structural re-arrangement can be induced by guest molecules at much lower pressure (~ 2 kPa). Experimental confirmation that this was indeed the case came from in situ powder XRD measurements at 77 K which allowed refinement of both the framework and N_2 adsorption sites.[13] Prior to this detailed structural work on ZIF-8, the adsorption behaviour for different gases had already been shown to be complex, with fundamental differences between the simulated and experimental adsorption isotherms. It was initially reported, using computational modelling techniques, that ZIF-8 displayed selective uptake of H_2 over other larger molecules such as N_2 and CH_4 due to the narrow size of the ring windows, restricting access to the large internal cavity for larger molecules.[14] However, this was later disproved experimentally, with ZIF-8 found to readily adsorb N_2, O_2 and CH_4, all of which are too large to theoretically enter the framework pores assuming a rigid framework; the mechanism of absorption is now known to involve the phase transition and opening of the MeIm gate.[15, 16]

In the previous high-pressure experiments on ZIF-8, a 4:1 by volume mixture of MeOH:EtOH was used as the pressure transmitting media (PTM). MeOH:EtOH is commonly used as it remains hydrostatic until 10 GPa, and

allows a systematic study of the framework as a function of pressure and on uptake of PTM. Using liquefied gases as a PTM is common in the fields of high-pressure physics and minerology but rarely employed outside of these fields.[17, 18] By using liquefied gases as PTM when studying adsorption processes in porous framework materials, the pressures that can be reached are much higher (GPa pressures) and thus the occupancies of the guest molecules inside the pores are much higher than at more modest pressures achievable with gas-cell capillaries (kPa pressures), ensuring higher quality X-ray diffraction representation of adsorption. In a recent study, liquefied CO_2 and CH_4 were loaded into the small pore MOF Sc_2BDC_3 at 0.20 and 0.30 GPa.[19] On increasing pressure to 2.50 GPa, hyperfilling of the framework of supercritical CH_4 was possible, allowing for the first time the determination of fully occupied CH_4 sites in the pores, which essentially formed a methane-MOF clathrate structure, while the loading of CO_2 revealed a new adsorption site which had previously never been observed experimentally. This new structure proved to give much better agreement with CO_2 isotherm data. In addition, the study provided the best possible model for any further computational modelling of adsorption of guests into the framework.[19]

Encouraged by previous success at using DAC techniques to investigate ZIF-8,[5] in this work the high pressure behaviour of ZIF-8 was studied using cryogenically loaded liquefied gases of CH_4, Ar, O_2 and N_2 to probe the high-pressure behaviour of ZIF-8 using experimental and computational techniques. In addition to locating the adsorption sites through high pressure crystallography, this chapter describes how a combination of periodic DFT methods and grand canonical Monte Carlo (GCMC) simulations was used to

relate the orientation of the MeIm ligands to the binding energies for each gas at specific adsorption sites.

4.3 Experimental

Synthesis of ZIF-8: A solid mixture of zinc(II) nitrate hexahydrate (0.525 g, 1.76×10^{-4} mol) and 2-methylimidazole (MeIm; 0.015 g, 1.83×10^{-4} mol) was dissolved in DMF (9 mL) in a 12 mL Teflon-capped vial. The vial was heated at a rate of 200°C h^{-1} to 130°C, held at this temperature for 24 h, and then cooled at a rate of 5°C h^{-1} to room temperature. Colourless polyhedral crystals were filtered from the reaction mixture, washed with chloroform (3×5 mL), and dried in air (30 min). Yield: 0.0064 g, 11 % based on 2-methylimidazole. The product was formulated using elemental analysis as $Zn(MeIM)_2(DMF)(H_2O)$ ($C_{11}H_{19}N_5O_2Zn$). Calculated C 41.51, H 5.97, N 22.01; found: C 42.04, H 5.46, N 21.83.

High-Pressure Cryogenic Loading: Each gas was cryogenically loaded into a diamond anvil cell (DAC) using the following basic procedure. A single crystal of ZIF-8 together with a chip of ruby (for pressure calibration) were loaded in a modified Merrill-Bassett diamond anvil cell (DAC) with 600 μm culet diamonds and a tungsten gasket.[20, 21] Springs were placed on the pins of the DAC and a calibration performed to determine the open and closed positions of the DAC. The DAC was then placed inside a cryogenic gas loading chamber (**Figure 4.2**), in the calibrated closed position and placed in a bath of liquid N_2 to equilibrate to 77 K. The gas (N_2, O_2, Ar or CH_4) was purged through the chamber until condensation occurred. The DAC was opened to a pre-calibrated open position in the bath of liquefied N_2 and the sample chamber exposed for approximately 30 seconds before closing. The DAC was then

removed from the bath and allowed to warm to room temperature before the pressure inside the cell was measured using the ruby fluorescence method.[21]

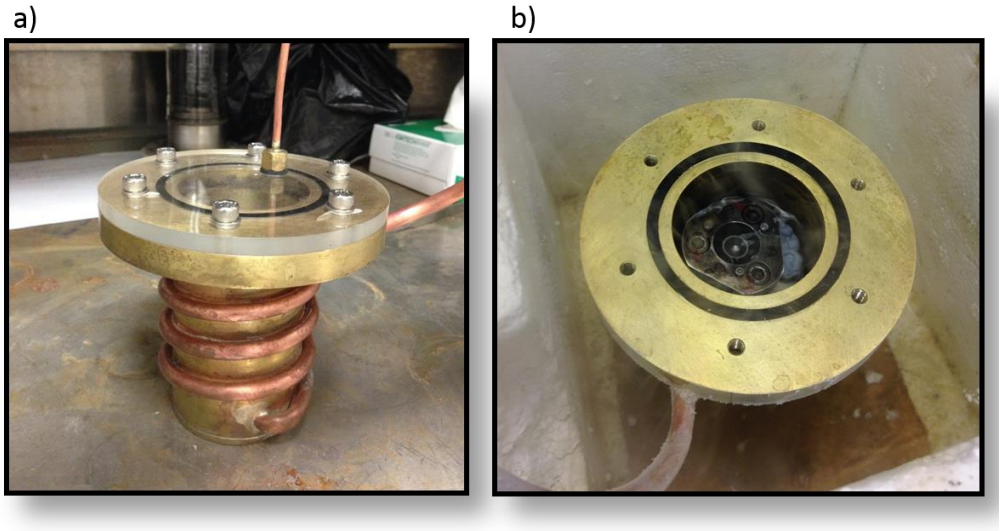

Figure 4.2: Cryogenic loading chamber set up: a) side view showing the brass coils through which the CH_4 gas is pumped into the chamber, b) top view showing the inside of the chamber with a DAC immersed in liquid CH_4, with the whole set up surrounded in liquid nitrogen in a polystyrene box.

High-pressure X-ray diffraction: High-pressure diffraction studies were collected on a Bruker APEX II diffractometer with graphite-monochromated Mo K_α radiation (0.71073 Å). Each gas loaded sample was studied over the following pressure regimes: CH_4 loaded in ZIF-8 (ZIF-8-CH_4) from 0.30 GPa to 1.40 GPa, O_2 loaded in ZIF-8 (ZIF-8-O_2) from 0.21 GPa to 2.00 GPa, N_2 loaded in ZIF-8 (ZIF-8-N_2) from 0.21 GPa to 3.25 GPa and Ar loaded in ZIF-8 (ZIF-8-Ar) from 0.75 GPa to 1.50 GPa. Upon increasing pressure, sample deterioration resulted in loss of resolution. Structure refinements were carried out to the maximum resolution of each sample as determined from the intensity statistics. Data were collected for each pressure point in ω scans in eight

settings of 2θ and ϕ, based on the strategy of Dawson *et al.* with an exposure time per frame of forty seconds and a step size of 0.5°.[22] The data were integrated using dynamic masks (generated using the program ECLIPSE), in order to avoid regions of the detector shaded by the DAC, while the absorption corrections for the DAC and sample were carried out using the program SADABS.[23, 24] The data were then merged in XPREP.[25]

Crystal Structure Refinements: Structure refinements were carried out in CRYSTALS starting from the ambient pressure structure of Park et al., (refcode VELVOY).[26, 27] All framework non-hydrogen atoms were refined anisotropically with thermal similarity and vibrational restraints applied to all non-hydrogen atoms except Zn. The SQUEEZE algorithm was applied (probe radius 1.2 Å, grid spacing 0.2 Å) to calculate the electron density in the pores and give an estimate to the number of guest species in the pore as a function of pressure.[28] Where the electron density was calculated to be at a maximum, the adsorbed gases were refined with crystallographic models, this occurred for Ar at 0.75 GPa, CH_4 at 1.40 GPa, N_2 at 3.25 GPa and O_2 at 0.75 GPa. For the adsorbed gases, argon and carbon atoms (for methane) were refined with anisotropic displacement parameters, whereas O_2 and N_2 were refined isotropically with distance, thermal and vibrational restraints applied.

Limiting window diameter analysis of the 4MR and 6MR windows in ZIF-8: Each crystallographic structure was analysed in Mercury using the void analysis tools to determine the limiting pore diameter [29] If guests were present in the pore, these were removed before void analysis. The grid spacing was set to 0.2 Å and the probe size was increased until the 4MR windows were no

longer accessible to solvent. The process was repeated for the 6MR windows of ZIF-8.

Density functional theory single point energy calculations: All calculations were performed using the CASTEP (version 5.11) simulation package.[30] The Hamiltonian operator was approximated using the Perdew-Burke-Ernzerhof (PBE) exchange-correlation functional, with the molecular wavefunction description provided by 'on-the-fly' pseudopotentials and a plane wave basis set operating at 650 eV, which gave convergence to within 4 meV per atom. The electronic structure was sampled at the gamma position only in the Brillouin zone due to the large size of the primitive unit cell (resulting in a k-point sampling grid of no greater than 0.06 $Å^{-1}$). Before carrying out single point energy calculations of the methyl functionalised imidazole ring rotation, the ambient crystal structure of ZIF-8 was geometry optimised without any symmetry constraints to allow both the relaxation of the atomic positions and the unit cell parameters. The potential energy surface was searched for energy minima by means of the Broyden-Fletcher-Goldfarb-Shanno (BFGS) algorithm.[31] The structure was considered to be optimised when the energy per atom, maximum force, maximum stress, and maximum atomic displacement converged to the values of 0.02 meV/atom, 0.05 eV/Å, 0.1 GPa, and 0.002 Å, respectively. Once optimised, the co-ordinates of the methyl imidazole linker were rotated through five degree increments from ambient to 30°; at each interval single point energy calculations were carried out at the same level of theory to the geometry optimisation. The data were then fitted to a second order polynomial to interpolate data between the 5° rotations.

Grand Canonical Monte Carlo simulations: Gas adsorption was simulated using grand canonical Monte Carlo (GCMC) simulations,[32] implemented in the

multipurpose code MuSiC.[33] The simulations were carried out using atomistic models of the frameworks ZIF-8AP and ZIF-8HP.[5] The atoms were fixed at their crystallographic positions. At each pressure, $5x10^7$ Monte Carlo steps were performed where each step consists of either a random translation, insertion or deletion, and for O_2 and N_2 random rotation – all equally weighted. The first 40 % of the steps were used for equilibration and the remaining used to calculate the ensemble averages. Standard Lennard-Jones (LJ) potentials were used to model the dispersive interactions between the framework and gases. The parameters for the force field were obtained from previous work from Fairen-Jimenez, who used a modified version of UFF (UFF*).[7] Mulliken charges were used as the partial charges on the framework – the advantage of using these charges is that they were derived from periodic DFT calculations and thus capture the periodic nature of the MOF. The Trappe force field was used to model O_2, CH_4 and N_2. Ar was modelled using Lennard Jones parameters fitted to vapour – liquid data.[34] Coulombic interactions were included for O_2 and N_2 and calculated using Wolf Coulombic summations which are much more efficient than Ewald summations.[35] Interactions beyond 18 Å were neglected. To calculate the gas-phase fugacity the Peng–Robinson equation of state was used.[36]

4.4 Results and discussion

4.4.1 The Effect of pressure on the framework fompressibility of ZIF-8 using CH_4, O_2, N_2 and Ar as PTM

Upon sealing the DAC at the lowest pressures possible using CH_4 as a PTM (0.30 GPa for ZIF-8-CH_4), the unit cell volume increased by 1.39% (**Figure 4.3**). This is indicative of the PTM penetrating into the pores of the framework, causing the unit cell to expand.[5, 37] On increasing pressure further to 0.50 GPa, the framework compressed (by 0.36%), before expanding again (by 2.83%) on increasing pressure to 0.70 GPa. The expansion of the unit cell dimensions here was accompanied by a phase transition to the ZIF-8-HP phase (as observed previously at 1.47 GPa when compressed using a MeOH:EtOH mixture as the PTM) (**Figure 4.3**).[5] On increasing pressure further between 0.70 and 1.40 GPa, the HP phase compressed, decreasing the unit cell volume by 1.40%. Above 1.40 GPa, the sample began to break apart, and no structural data could be extracted.

Upon closing the DAC at 0.21 GPa using O_2 as a PTM, the framework compressed slightly (by 0.10%). On increasing pressure to 0.50 GPa, the unit cell volume then decreased further (by 0.53%), before increasing again (by 0.20%) on increasing pressure to 0.75 GPa. The expansion shown here at 0.75 GPa was as a result of the transition to the ZIF-8HP phase, in an almost identical fashion to the compression study using CH_4 as the PTM. On increasing pressure further from 0.75 to 2.00 GPa, the framework compressed by 6.70%, resulting in an overall compression of 7.00%, compared to the volume observed under ambient temperature and pressure conditions. Above 2.00 GPa, the O_2 PTM began to solidify. As a consequence, the diffraction data

quality were seriously compromised and no further structural data could be extracted.[38]

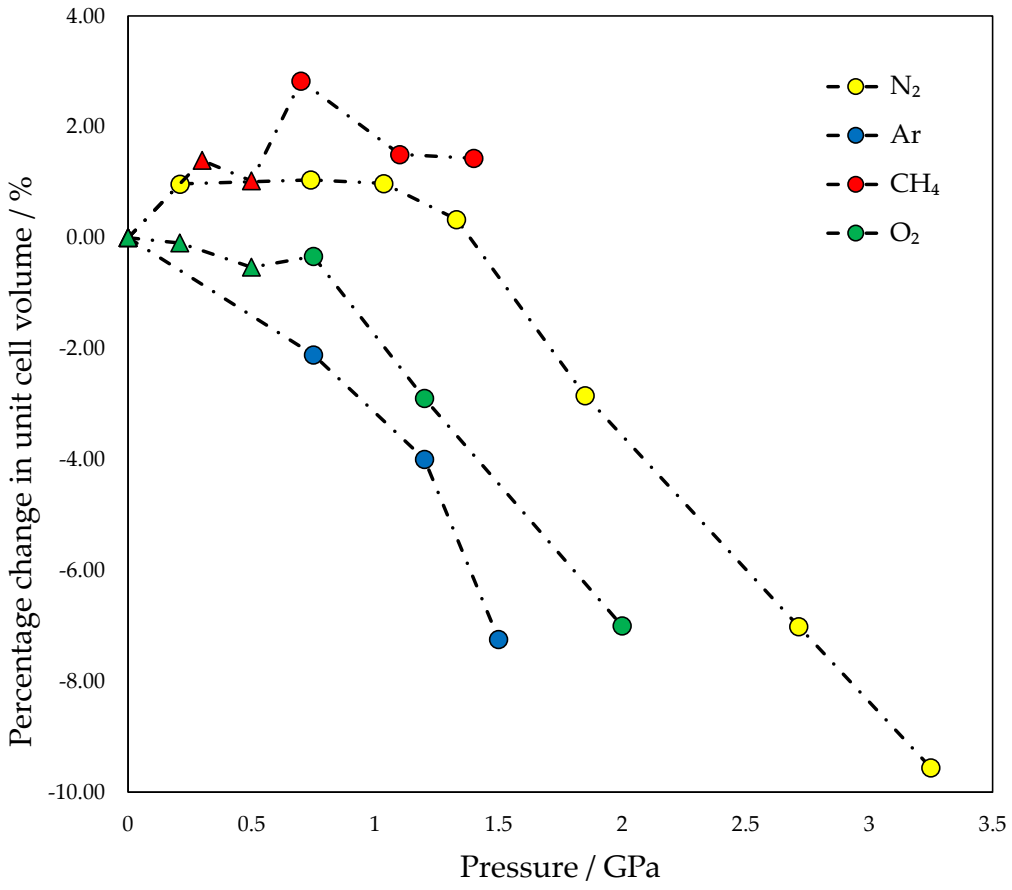

Figure 4.3: (a) Change in unit cell of ZIF-8 with pressure for N_2 (yellow), CH_4 (red), Argon (blue), O_2 (green), triangles and circles indicate ZIF-8AP and ZIF-8HP phases respectively.

On loading ZIF-8 with N_2 at 0.21 GPa, the unit cell volume increased by 1.00%. Unlike the compression studies in CH_4 and O_2, however, on loading ZIF-8 in N_2 the framework had already transformed to the ZIF-8HP phase. On increasing pressure further to 1.03 GPa, the unit cell volume remained approximately constant, changing by no more than 0.07%. This

incompressibility has been seen in other framework families, such as the UiO family, where the filling of the pores with methanol causes the structure to be resistant to compression to ~ 5 GPa.[39] On increasing pressure from 1.03 to 1.33 GPa, the framework began to compress by 3.17%. Upon increasing pressure to 3.25 GPa the framework was compressed by a further 6.71%, causing a total compression in unit cell volume of 9.55%

The final gas used as a PTM was Ar, which when loaded in a DAC with ZIF-8 and compressed to 0.75 GPa, resulted in a decrease in unit cell volume of 2.11%. Ar here behaves in a similar manner to N_2, as on loading at 0.75 GPa the framework had also transformed to the ZIF-8HP phase. On increasing pressure to 1.50 GPa, the framework compressed (by 7.24%). The compressibility of ZIF-8 in CH_4 is somewhat different, as the framework is never compressed past the ambient pressure value and ZIF-8 is always superfilled with solvent. It is well known that the compressibility of MOFs are dependent on the choice of hydrostatic media, such as in the case of Cu-BTC ($[Cu_3(BTC)_2(H_2O)_3 \bullet (guest)]$, with BTC = 1,3,5-benzenetricarboxylate)[40], where Chapman *et al.* found by using hydrostatic media composed of molecules of increasing sizes, i.e. MeOH, isopropyl alcohol and Fluorinert (a perfluorinated alkyl amine), they could induce different compressibility of the framework. Larger molecules were observed to cause a larger compression on Cu-BTC, whereas smaller hydrostatic liquids interact with the pore network causing the onset of compression to occur at higher pressures.[40]

4.4.2 *The Effect of pressure on the framework geometry and pore content of ZIF-8 using CH_4, O_2, N_2 and Ar as PTM*

On increasing pressure (and guest content) using CH_4, O_2, N_2 and Ar as PTM, changes in the framework geometry were monitored. The rotation of the MeIm linker in particular, was measured by the angle, θ, defined as the angle the MeIm plane made with the (100) plane. In the original compression study of ZIF-8 in a MeOH:EtOH PTM under ambient conditions, θ measured 64.3° (**Figure 4.1c**).[5] Upon the transition to ZIF-8HP, θ increased to 89.7° (**Figure 4.1d**). This structural rotation had an effect on both the 4MR and 6MR window diameters and consequently the pore volume. Under ambient conditions, the 4MR and 6MR windows measured 0.8 Å and 3.0 Å, respectively (using a grid spacing of 0.2 Å). On transforming to ZIF-8HP at 1.47 GPa, both the 4MR and 6MR windows increased to 2.2 Å and 3.7 Å, respectively. Although the volume of the nanopore decreased in size on undergoing the transition from 2485 to 2439 $Å^3$ at 0.96 and 1.47 GPa respectively, the overall effect of increasing the 4MR and 6MR window diameters increased the overall pore volume. [5]

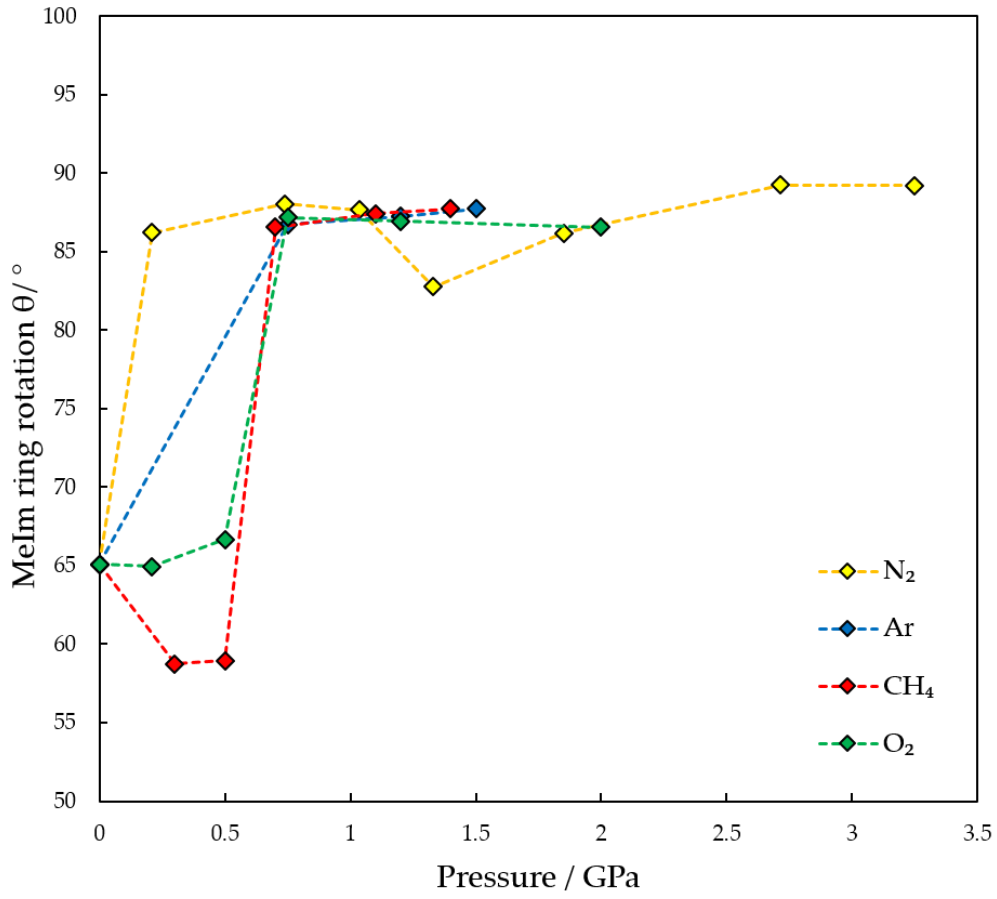

Figure 4.4: Change of angle of rotation of MeIm linker in ZIF-8 upon increasing pressure for N_2 (yellow), O_2 (green), Ar (blue) and CH_4 (red).

Under ambient pressure and temperature conditions in this study, θ measured 65.1°. On loading in CH_4 at 0.30 GPa, θ actually decreased (to 58.7°), causing the 4MR and 6MR windows to increase and decrease from 0.8 to 0.7 Å, and 3.0 to 3.1 Å respectively. No noticeable increase in guest molecule content (calculated using the SQUEEZE algorithm with the programme PLATON see **Table 4.1**), was observed.[28] The energy barrier to rotation of this first rotation calculated by means of DFT single point energy calculations is relatively small, with an energy penalty of just 0.4 kJ mol^{-1} per MeIm linker (see Chapter Three

Figure 3.8). On increasing the pressure further to 0.50 GPa, θ remained essentially unchanged (measuring 58.9°). Such a small change in rotation did not change the 4MR and 6MR diameters, however there was a small increase in electron density in the pores equating to ~5 CH_4 molecules/uc (molecules per unit cell) (**Table 4.1**). On increasing pressure to 0.70 GPa, θ increased to 86.6°, transforming to the ZIF-8HP phase, causing the diameters of the 4MR and 6MR to both increase to 2.5 Å and 3.3 Å, respectively. This was accompanied with a large change in solvent uptake into the pore (equating to ~62 CH_4 molecule/uc). The energy penalty for the framework to undergo such a rotation was calculated to be 5.8 kJ mol^{-1} per MeIm linker, indicating that the energy of adsorption must be much greater to overcome this energy barrier. On increasing pressure further to 1.40 GPa, θ continued to increase, measuring 87.8° at 1.40 GPa (a 6.2 kJ mol^{-1} penalty for rotation per linker). Conversely the 6MR diameter actually decreased between 0.70 and 1.40 GPa (by 2.4%), though this coincides with a reduction in the unit cell volume (of 1.4%) as the ZIF-8HP phase was compressed.

In a similar manner to CH_4, on loading ZIF-8 in O_2 at 0.21 GPa, θ also decreased (from 65.1° to 64.9°). This small rotation caused the 4MR and 6MR windows to increase and decrease from 0.8 Å to 0.9 Å and 3.0 Å to 2.9 Å, respectively. This was accompanied by an increase in pore content of ~26 O_2 molecules/uc. On increasing the pressure further to 0.50 GPa, θ increased to 66.7° and coincided with a further increase in pore content (~72 O_2 molecules/uc), the 4MR and 6MR diameters remained unchanged. On increasing pressure to 0.75 GPa, θ increased to 87.2° as a result of the transition to the ZIF-8HP phase (with an associated framework rotation energy penalty of 6.0 kJ mol^{-1}), resulting in the largest uptake of O_2, (~85 molecules/uc). Both the 4MR and

6MR diameters increased to 2.2 Å and 3.6 Å, respectively, as a result of the transition. On increasing pressure to 2.0 GPa, the 6MR diameter decreased (along with the unit cell volume) as the ZIF-8HP phase was compressed. For ZIF-8 loaded in both CH_4 and O_2 PTM, it was possible to see the effect the guest had on the framework before transforming to ZIF-8HP, as for both the MeIm linkers rotate to lower θ values before transforming to ZIF-8-HP (resulting in an increase in θ). Although not mentioned in the original HP study of ZIF-8 using MeOH/EtOH as a PTM, there θ also decreased on going from ambient pressure to 0.18 GPa (from 64.3° to 59.2°). On increasing pressure further from 0.18 to 0.96 GPa, θ increased to 59.8° before transforming to ZIF-8HP (where θ increased to 89.7°). This decrease in θ would therefore appear to be a general trend observed during the diffusion of fluid molecules into ZIF-8 prior to the transition to ZIF-8HP.

In the case of N_2 and Ar loaded ZIF-8, the framework had already undergone the transition to ZIF-8HP upon loading (at 0.20 and 0.75 GPa respectively), resulting in an increase in θ from 65.1° in the ambient pressure structure to 86.2° and 86.7° respectively, with similar energy penalties for the framework rotation (of ~5.8 kJ mol^{-1} per linker). Both were accompanied by an increase in pore content (**Table 4.1**). The 6MR windows increased from 3.0 Å to 3.4 Å and 3.3 Å for N_2 and Ar respectively, while the 4MR window diameters increased from 0.8 to 2.5 Å for both gases. On increasing the pressure further to 0.74 GPa with N_2, the 6MR windows increased to a maximum value of 3.5 Å, above this pressure the 6MR window diameter decreased in size along with the unit cell volume as the ZIF-8HP phase was compressed, whereas θ continually increased to a maximum of 89.2° at 3.25 GPa (with an associated rotation penalty of 6.8 kJ mol^{-1}, increasing by 1.0 kJ mol^{-1} from 0.20 GPa). The same

trend was seen in Ar loaded ZIF-8, where above 0.75 GPa the 6MR window diameters decreased along with the unit cell compression, with θ continually increasing to a maximum of 87.7° at 1.50 GPa. The associated energy penalty for the framework rotation is 6.2 kJ mol^{-1}.

Table 4.1: Unit cell volume, solvent accessible pore volume (SAV), pore content and diameter of 4MR and 6MR windows for the different phases of ZIF-8 loaded with N_2, Ar, O_2 and CH_4 as PTM on increasing pressure. The transition to the ZIF-8HP phase is highlighted with *.

Pressure (GPa)	Unit cell volume (Å³)	% change in uc volume	CH_4 (mole/uc)	SAV (Å³)	θ (°)	4MR diameter (Å)	6MR diameter (Å)
0.00	4924.5(2)	0.00	n/a	2497	65.1	0.8(1)	3.0(1)
0.30	4993.1(1)	1.39	0	2580	58.7	0.7(1)	3.1(1)
0.50	4974.9(4)	1.02	5	2551	58.9	0.7(1)	3.1(1)
0.70*	5063.8(4)	2.83	62	2657	86.6	2.5(1)	3.3(1)
1.10*	4998.5(4)	1.50	64	2710	87.4	2.5(1)	3.2(1)
1.40*	4995.1(3)	1.43	69	2586	87.8	2.5(1)	3.2(1)

Pressure (GPa)	Unit cell volume (Å³)	% change in uc volume	O_2 (mole/uc)	SAV (Å³)	θ (°)	4MR diameter (Å)	6MR diameter (Å)
0.00	4924.5(2)	0.00	n/a	2514	65.1	0.8(1)	3.0(1)
0.21	4919.8(5)	-0.10	26	2487	64.9	0.9(1)	2.9(1)
0.50	4898.2(3)	-0.53	72	2456.8	66.7	0.8(1)	2.9(1)
0.75*	4908.0(4)	-0.33	85	2521.9	87.2	2.2(1)	3.6(1)
1.20*	4782.0(9)	-2.89	78	2355.9	86.9	2.2(1)	3.4(1)
2.00*	4579.9(6)	-7.00	33	2255	86.6	2.4(1)	3.1(1)

Pressure (GPa)	Unit cell volume (Å³)	% change in uc volume	N_2 (mole/uc)	SAV (Å³)	θ (°)	4MR diameter (Å)	6MR diameter (Å)
0.00	4924.55(23)	0.00	n/a	2497	65.1	0.8(1)	3.0(1)
0.21*	4972.3(4)	0.97	14	2548.1	86.2	2.5(1)	3.4(1)
0.74*	4976(1)	1.04	54	2524.7	88.0	2.3(1)	3.5(1)
1.03*	4972.8(9)	0.98	72	2512	87.7	2.3(1)	3.5(1)
1.33*	4940.8(3)	0.33	64	2401.8	82.8	2.0(1)	3.5(1)
1.85*	4784.5(6)	-2.84	65	2363.8	86.2	2.0(1)	3.5(1)
2.72*	4579.3(5)	-7.01	76	2222.6	89.3	2.2(1)	3.2(1)
3.25*	4454.0(3)	-9.55	32	2053.7	89.2	2.2(1)	3.0(1)

Pressure (GPa)	Unit cell volume (Å^3)	% change in uc volume	Ar (atoms/uc)	SAV (Å^3)	θ (°)	4MR diameter (Å)	6MR diameter (Å)
0	4924.5(2)	0.00	n/a	2497	65.1	0.8(1)	3.0(1)
0.75*	4820.6(3)	-2.11	53	2458	86.7	2.5(1)	3.3(1)
1.20*	4727.9(5)	-3.99	54	2405	87.3	2.4(1)	3.3(1)
1.50*	4567.9(4)	-7.24	51	2256	87.7	2.4(1)	3.2(1)

SAV = solvent accessible volume, calculated using PLATON, with probe size of 1.2 and a grid spacing of 0.2 Å.[28] Diameters of 4MR and 6MR calculated using the void analysis routine in Mercury, (grid spacing of 0.2 Å).[29, 41, 42] % change in uc volume is normalised to ambient.

4.4.3 Crystal structures of ZIF-8 loaded with CH_4, O_2, N_2 and Ar:

For CH_4 and O_2 loaded ZIF-8, the gas molecules could not be modelled atomistically in ZIF-8AP, as the guest content was too low and the electron density in the pores too diffuse. As a consequence, the pore content was modelled using the SQUEEZE algorithm in PLATON for all pressure points in all PTMs. After the phase transition to ZIF-8HP structural models were obtained when the electron density in the pores was sufficient enough to model. The pressures of the ZIF-8 gas loaded models were taken at 1.40, 0.75, 3.25 and 0.75 GPa in CH_4, O_2, N_2 and Ar PTM respectively (**Table 4.1**).

The simplest gas to study was Ar, due to its high X-ray scattering factor and its monatomic nature. On loading at 0.75 GPa, six symmetry independent adsorption sites could be located, all of which were fully occupied (**Figure 4.5**). Site Ar-1 (green) sits in the centre of each 6MR window, whilst Ar-2 (red) is positioned between the 4MR and 6MR windows, directly below every other MeIm linker in the 6MR window (**Figure 4.5d**). Ar-3 (yellow) sits in the centre of the 4MR window. Both Ar-1 and Ar-3 sites have slightly elongated ellipsoids in the direction perpendicular to the plane of the windows (**Table 4.2**), showing that these sites are quite labile and the guests, on average, are librating in and out of the plane of the 4MR and 6MR windows. Ar-4 (blue) is located below Ar-1 further into the nanopore, and makes a close contact to the 4MR window, with the closest contact measuring 3.8118(1) Å to the imidazole C2 carbon (**Figure 4.5c**). Ar-5 (orange) sits below the 6MR window equidistant from the MeIm ligands with the shortest contact distance to a non-H atom of C2 to Ar-5 of 4.8677(1) Å, **Figure 4.5d**). Ar-6 (magenta) sits in the centre of the large nanopore above the 6MR windows. The closest non-hydrogen atom

contact to Ar-6 measures 5.9078(2) Å, from the methyl (C3) atoms (**Figure 4.5b**).

Table 4.2: Principal axes of the ellipsoids of Ar and CH_4 sites in ZIF-8 at 0.75 and 1.40 GPa respectively. Note the elongation of Ar-1 and Ar-2 as well as CH_4-1 and CH_4-2 from minimum to maximum principal axis. This direction is perpendicular to 6MR and 4MR windows respectively.

Ar site	Minimum principal axis ($Å^2$)	Maximum principal axis ($Å^2$)	CH site	Minimum principal axis ($Å^2$)	Maximum principal axis ($Å^2$)
Ar-1	0.0517	0.1137	CH_4-1	0.0547	0.0888
Ar-2	0.0342	0.1369	CH_4-2	0.0268	0.1448
Ar-3	0.0677	0.0879	CH_4-3	0.0641	0.0832
Ar-4	0.0710	0.0961	CH_4-4	0.0503	0.0674
Ar-5	0.0643	0.0879	CH_4-5	0.0383	0.1193
Ar-6	0.1062	0.1233	CH_4-6	0.1296	0.1353

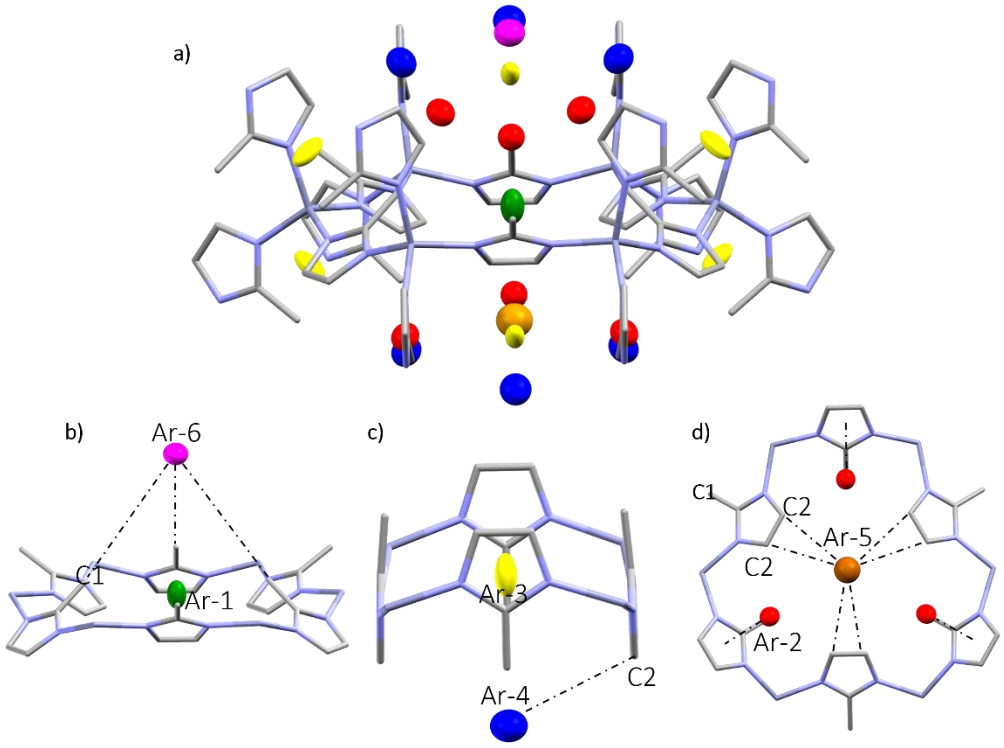

Figure 4.5: a) Ar adsorption sites in ZIF-8 at 1.20 GPa as shown on a 6MR window for Ar-1 (green), Ar-2 (red), Ar-3 (yellow), Ar-4 (dark blue), Ar-5 (orange), Ar-6 (magenta). Short contacts for (b) Ar-6 with the methyl C-atom (C1) and (c) Ar-4 with the imidazole C-atom (C2) and (d) Ar-5 (with C2) are drawn as black dotted lines and discussed in the text. Colour scheme; Zn (grey), N (light blue) and C (grey). Hydrogen atoms have been omitted for clarity, ellipsoids for Ar-atoms are drawn at 50 % probability, whilst the ZIF-8 framework is drawn as capped sticks.

The position of the six adsorption sites found in Ar are also representative of those found in ZIF-8-HP for CH_4 (at 1.40 GPa). At a pressure of 1.40 GPa, the CH_4 content reached a maximum and the adsorption sites could be refined with anisotropic displacement parameters. Again the values of the principal axes of the ellipsoids give a measure of the lability of the adsorption sites (**Table 4.2**). In particular, CH_4-1, CH_4-2 and CH_4-5 show elongation along one

direction (perpendicular to the 6MR window for CH_4-1 and to the 4MR window for CH_4-2 and CH_4-5).

In ZIF-8HP at 3.25 GPa in N_2 the adsorption sites are located in the same positions as Ar, however, some more labile N_2 positions exhibit positional disorder (**Figure 4.6**).[43] N_2-1 (green) shows positional disorder perpendicular to the 6MR window, with one N-atom fully occupied, whilst the other was split across two positions (50% occupied). The shortest contact to the central N atom from N_2-1 measures 3.444(49) Å to the C2-atom on the MeIm ligand. N_2-2 (red) site shows no disorder; it is positioned around a 3-fold axis that goes through the centre of the 6MR window, with each N_2-2 sitting above every other MeIm linker in the 6MR. N_2-3 (yellow) displayed similar disorder to N_2-1 but in the four-membered window, with one fully occupied N in the plane of the window with a 50% occupied N atom above and below the plane. N_2-4 (blue) is located below the 4MR window and also exhibits similar disorder to N_2-1 and N_2-3. The central N atom sits directly below N_2-3, and the other N-atom is split across two positions (50 % occupied) with a close contact to C3 of the MeIm linker of 3.08(8) Å. N_2-5 (orange) is situated below the 6MR window at a distance of 4.10(16) from C2, and is in close contact with N_2-1 with a contact distance of 1.99(33) Å. N_2-6(magenta) sits on the axis of rotation going through the 6MR window, above N_2-1 at a distance of 3.7(5) Å. It is worth noting that N_2-5 and N_2-6 have larger Uiso values than N_2-1 to N_2-4, illustrating that these sites are diffuse and most likely not fully occupied (**Figure 4.6**).

At 1.20 GPa, the oxygen positions within ZIF-8HP could be successfully refined and were comparable to that of ZIF-8-N_2. The same sites in both gases

displayed positional disorder. (**Figure 4.6**). O_2-1 (green) sits in the centre of the 6MR window displaying the same occupational disorder as N_2-1. O_2-2 (red) sits around the three fold axis that goes through the 6MR ring, resulting in O_2-2 sites above every other MeIm linker in the 6MR. The difference with O_2-2 and N_2-2 site is the angle which they make with the MeIm linker, defined as the O_2-2(1)-O_2-2(2)-C3 angle (**Figure 4.6f**). An angle of 90° would mean the molecule sits parallel to the MeIm ring, however for O_2-2 the angle is 130° and the respective N_2-2 angle is 150°. Thus it can be seen that N_2 prefers an arrangement closer to an *end-on* intermolecular interaction (**Figure 4.6e**) than a more traditional *side-on* interaction seen in O_2-2 (**Figure 4.6f**). O_2-3 (yellow) sits in the 4MR window, with the same occupational disorder as N_2-3. O_2-4 (blue) exhibited the same disorder as in ZIF-8-N_2, where the middle oxygen is fully occupied and there is a 50% occupied oxygen on either side. O_2-5 (orange), sits below the 6MR window at a distance of 4.06(176) from C2, and is in close contact with O_2-1 with a shortest contact distance of 1.779(402) Å. The close contact of this site with other O_2 sites and the fact that it is at a significant distance from the framework itself may be an indication that it is only favourable due to guest-guest interactions rather than interactions with the framework. O_2-6 is the site located furthest from the framework, in the centre of the nanopore. The closest contact to the framework is with C3 at 5.326(209) Å (**Figure 4.6h**). Again in relation to ZIF-8-N_2, the U_{iso} values of O_2-5 and O_2-6 are much larger than for the other O_2 sites, illustrating that O_2-5 and O_2-6 are diffuse and most likely not fully occupied.

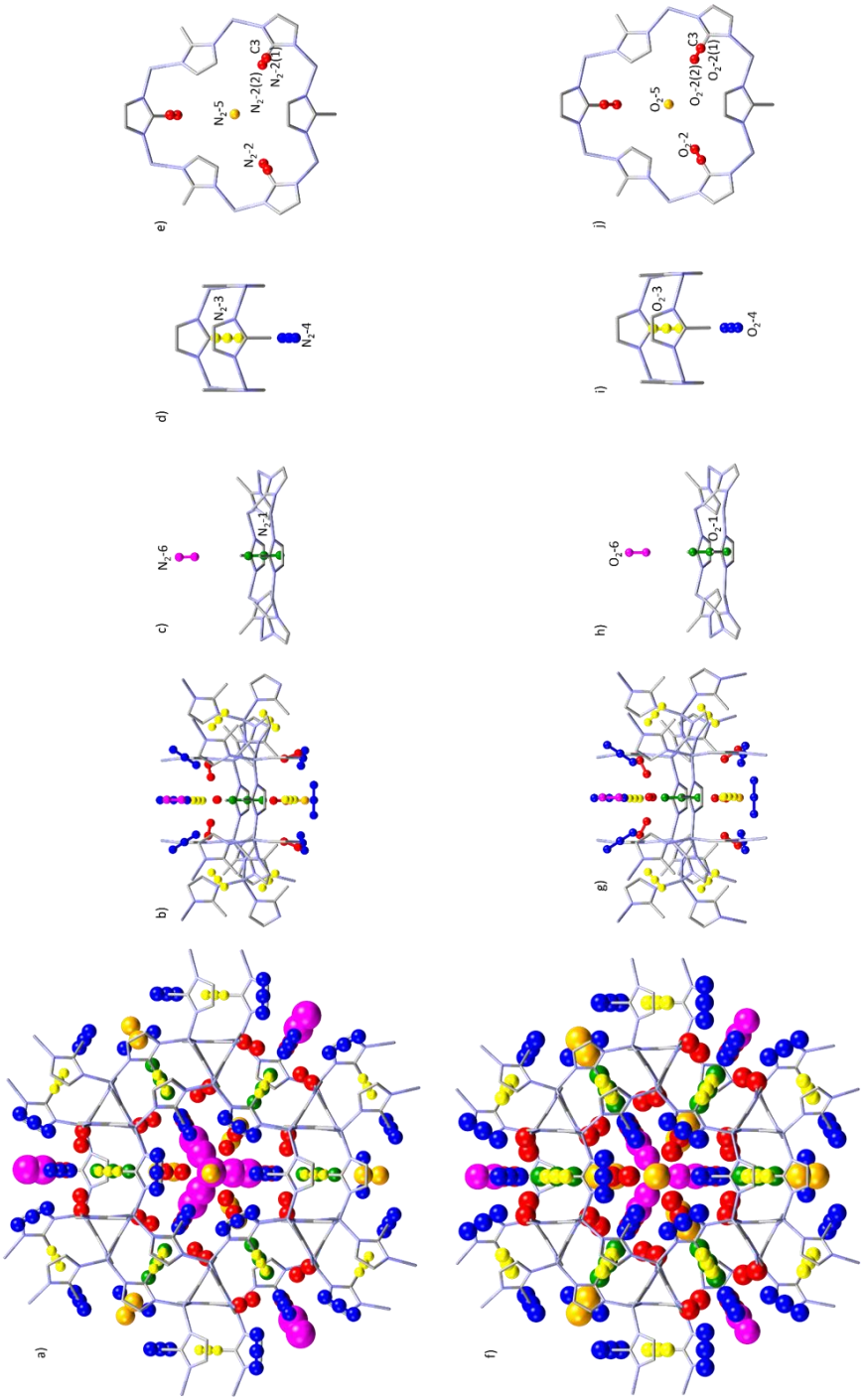

Figure 4.6: Unit cell of ZIF-8-HP with adsorbed N_2 at 3.25 GPa (a), with O_2 at 1.20 GPa (f). In (a) and (f) guests shown as ellipsoids (50% probability) and each colour represents symmetry independent adsorption sites and viewed down the 111 axis. View of 6MR window with N_2 (b) and O_2 (g) adsorption sites. 6MR window with sites N_2-1 and N_2-6 (c) and O_2-1 and O_2-6 (h). 4MR window with sites N_2-3 and N_2-4 (d) and O_2-3 and O_2-4 (i). 6MR window with N_2-2 and N_2-5 (e) and O_2-2 and O_2-5 (j).

4.4.4 Grand canonical Monte Carlo simulations of gases into ZIF-8

To have a complete understanding of the adsorption process within ZIF-8, in particular for the reasons behind the transition to the HP phase, and to be able to quantify the energies of each adsorption site that was identified crystallographically, simulations of adsorption isotherms were carried out. These were done by means of the grand canonical Monte Carlo (GCMC) method for all gases studied using both ZIF-8-AP and ZIF-8-HP phases. Previous work has shown excellent agreement between simulated and experimental adsorption isotherms for both the ZIF-8AP and HP structures.[7, 44] The crystallographic data for ZIF-8-Ar proposes the structure can support 66 argon atoms per unit cell (0.75 GPa), while the GCMC simulations predict 60 sites. The similarity in the two values confirms that the force field parameters appear to be well suited for this system and the small discrepancy between the two is likely to be due to a super-filling effect which is observed experimentally, not computationally. This effect, which is well documented within the high-pressure MOF community, is where at high pressures the pores of porous materials often swell to accommodate extra guest in thermodynamically inaccessible regions.[37] As the GCMC method operates on a fixed-framework model this super-filling effect will not be mimicked by the simulation.

Figure 4.7 shows the distribution of energies of each sorbate with each ZIF-8 phase at 1 bar. Each peak normally corresponds to an adsorption site (although sometimes two different adsorption sites can have similar fluid-framework interaction energies). Analyses of the energy histograms of the two phases of the framework explain why the framework undergoes a transition: the interaction energies of each sorbate with ZIF-8 is lowered by ~ 3 kJ mol^{-1} (i.e.

more negative and favourable) by switching to ZIF-8HP, and in the diatomic cases by up to 7 kJ mol^{-1}, so any penalty for the framework rotation (as calculated by DFT) to the HP phase must be outweighed by the favourable adsorption sites. Although the framework for ZIF-8 was once assumed to be rigid and the phase transition has yet to be seen upon variable temperature studies which could provide enough thermal energy to undergo linker rotation transitions, it has been shown here that the interaction with guest molecules induce linker rotation.[45]

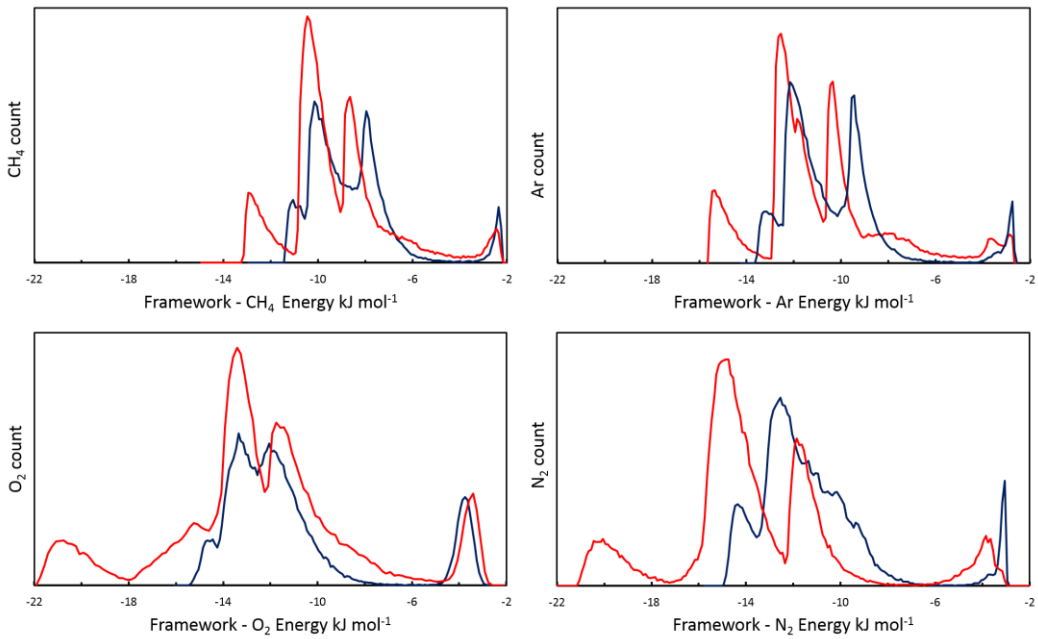

Figure 4.7: Histograms of guest- framework interaction energies at 1 bar (0.0001 GPa) during GCMC simulation in ZIF-8 clockwise from top left ZIF-8-CH4, ZIF-8-Ar, ZIF-8-N_2, ZIF-8-O_2 Red plot shows interactions with ZIF-8-HP, blue plot shows interactions with ZIF-8-AP.

For each guest adsorbed in ZIF-8HP, it was possible to correlate these energies with the crystallographically determined sites, as each guest location can be visualised within the framework (for example in **Figures 4.8** & **4.9**). Here each dot corresponds to the centre of mass (COM) position of a fluid molecules, which was coloured according to an energy interval taken from a peak in the

energy histogram (**Figure 4.8**). By understanding the energies of guest-framework interactions with the experimentally determined positions of the guest, we can rationalise chemically why each site is preferred and in the case of diatomics O_2 and N_2, the preferred orientation of the molecule.

ZIF-8-Ar GCMC analysis

For ZIF-8-Ar, the GCMC simulations with the HP phase gave excellent agreement with the crystal structure positions of argon (c.f. **Figure 4.5 and Figure 4.9)**. In addition, the energies of each absorption site have been calculated (**Figure 4.8**). Ar-1 (green) is the lowest energy site with a framework- argon interaction energy of ~-16 kJ mol^{-1}. In**Figure 4.9a** the effect of libration can be seen in this site, due to the COM positions sit in and out of the plane of the six-membered window.

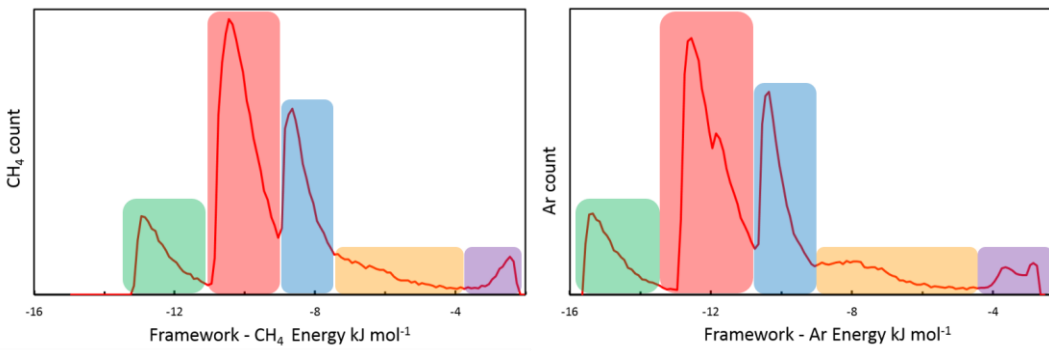

Figure 4.8: Histograms of guest- framework interaction energies at 1 bar of guest during GCMC simulation in ZIF-8. ZIF-8-CH4 (left), ZIF-8-Ar (right). Red line shows interactions with ZIF-8-HP. The coloured sections show the area of each peak in the plot and each colour is the colour of each centre of mass in Figure 4.9.

The second lowest energy site is Ar-2, ~-12 kJ mol^{-1}. Ar-3, the site which sits in the plane of the 4-MR is found to have a similar energy, however its orientation

has a large effect on the energy of the site: if the position is offset from the centroid of the four-membered window can lower this energy (as seen in **Figure 4.9c**) to around -10 kJ mol^{-1}. Site Ar-4 also has an interaction energy of ~-10 kJ mol^{-1} (seen in blue in **Figure 4.8**). In the histogram, the orange block of ZIF-8-Ar has a large energy range with a fairly low argon count: this region correspond to Ar-5. It can be noted that this higher energy (weak interaction) site can have a larger spread of interaction energies and therefore a weaker binding with the framework. This site is predominately found in the central pore and **Figure 4.9d** shows that the position of argon during each iteration of the simulation can vary compared to other sites. The lowest energy site is Ar-6 in magenta (see **Figure 4.8 and 4.9)** with an interaction energy in the order of -2 kJ mol^{-1}. This site also has a diffuse orientation in the framework due to the weak interactions.

ZIF-8-CH_4 GCMC analysis

The density distribution analysis for ZIF-8-CH_4 was similar to ZIF-8-Ar, with each CH_4 site found in its refined crystallographic position (see **Figure 4.9**). One difference in the two systems was the decreased interaction energy between CH_4 and ZIF-8 compared to Ar and ZIF-8, where each site was found to be a few kJ mol^{-1} less favourable in ZIF-8-CH_4 than ZIF-8-Ar. This is due to the size of Ar compared to CH_4, and is explicit in the larger LJ parameters. Ar is often thought of as an inert gas, however the dispersion forces are quite substantial.[34]

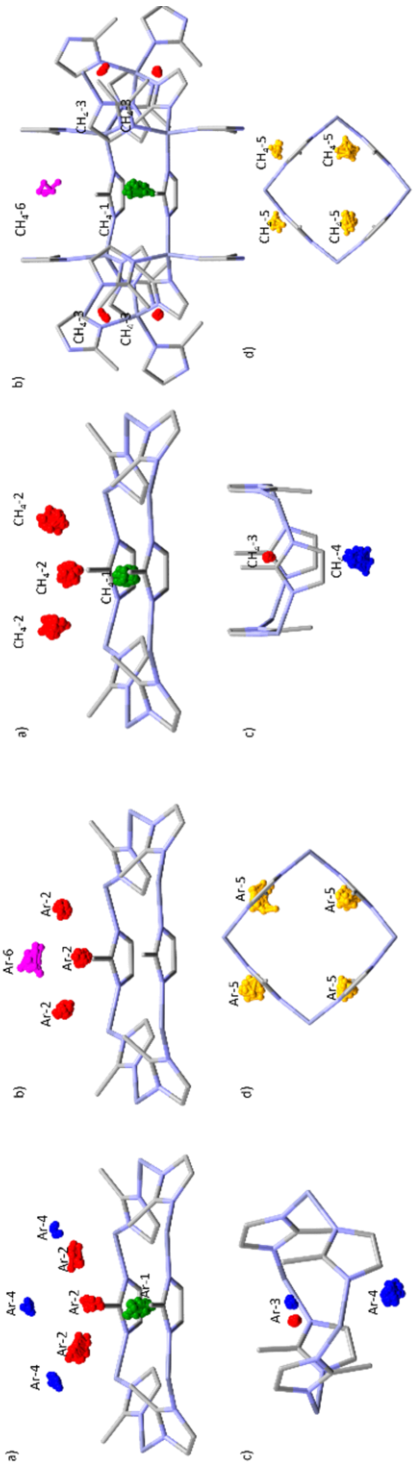

Figure 4.9: GCMC sites for Ar (Left) and CH_4 (right) in ZIF-8 at 1 bar. Colours of sites correspond to the sections in Figure 4.8 Sites in terms of decreasing interaction energy with the framework are green > red > blue > orange > magenta. (a) Sites-1, -2 and -4 within the six-membered window. (b) Sites -2and -6 within the six-membered window. (c) -3 and -4 within the four-membered MeIm window. Note the two energy sites for Ar-3. (d) Site -5 viewed down the *a* axis showing the four-membered MeIm window

ZIF-8-O_2 and ZIF-8-N_2 GCMC analysis

Upon comparing the positions of both O_2 and N_2 from the GCMC simulations with respect to their crystallographic coordinates, there was good agreement, giving confidence to the parameters used in the simulation. In order to have better sampling statistics on the atomic positions of each diatomic molecule within the framework, NVT ensemble simulations were carried out at the maximum loading at 1 bar (62 molecules/unit cell and 53 molecules/unit cell for ZIF-8-O_2 and ZIF-8-N_2 respectively). The positions for the simulations were stored every 1000 steps. Calculated atomic positions from the GCMC simulations could help explain features found in the crystal structures, such as large isotropic displacement parameters (Uiso) and disordered molecules (**Figure 4.10**), as well attaining the energy of each adsorption site from the simulation. For instance, guest molecule site one, N_2-1 and O_2-1, showed crystallographic disorder in the 6MR plane, and in the simulation this site also shows a range of positions above and below this plane (circled in green in **Figure 4.10**). Some sites, O_2-2 to 3 and N_2-2 to -3, had a small spread of atomic positions throughout the sampling of space during the simulation which confirms their crystallographic full occupancies (i.e. the site is there all of the time) and the small Uiso values (circled in dark green in **Figure 4.10**). Differences in the larger Uiso values that were crystallographically refined for sites N_2-5 to 6 and O_2-5 to 6, (Uiso parameter shown in orange and magenta in **Figure 4.10**) could be explained from the simulations. The stored positions for these sites were scattered in the nanopore, suggesting that the energy landscape is very flat in the centre of the pore. In addition, the sites are not present in every part of the unit cell, suggesting that there occupancy is not

100 % which would explain the large Uiso parameter refined from the crystallographic data.

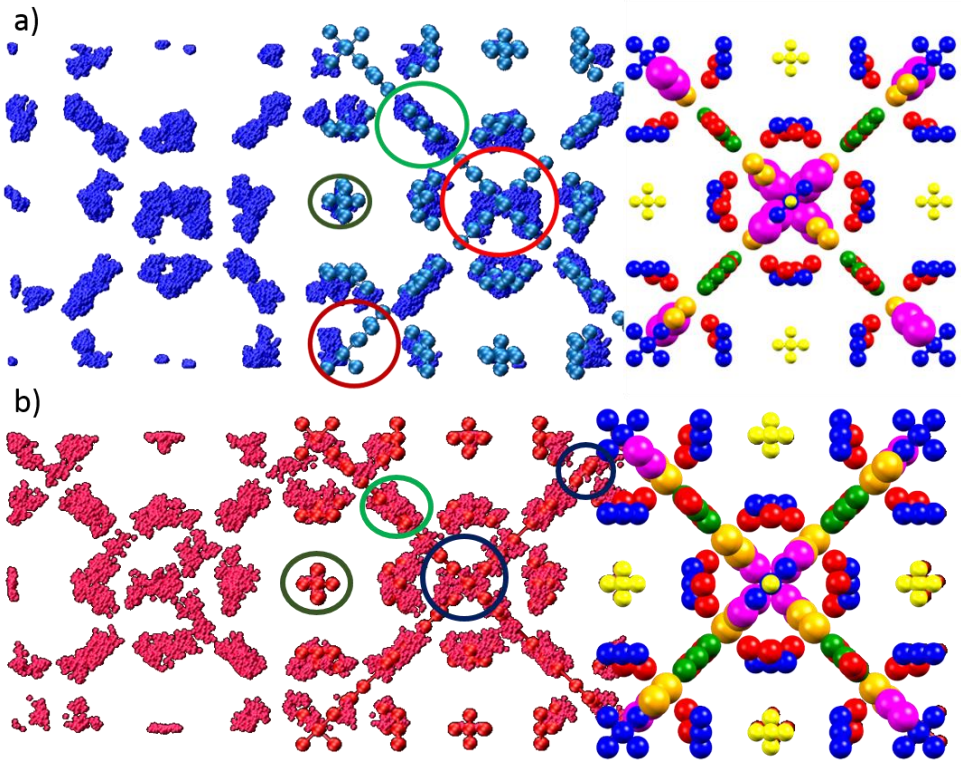

Figure 4.10: (a) From left to right, the binned atomic positions of N_2 during NVT simulation at 1 bar (53 molecules per unit cell) – dark blue, overlay of crystal structure of N_2 at 3.25 GPa (light blue) with NVT N_2 atomic positions (dark blue) and crystal structure of N_2 at 3.25 GPa with Uiso parameter displayed at 50 %. Each colour represents symmetry independent site as in previous figures. (b) From left to right, the binned atomic positions of O_2 during NVT simulation at 1 bar (62 molecules per unit cell) (pink), overlay of crystal structure of O_2 at 0.75 GPa (red) with NVT O_2 atomic positions (pink) and crystal structure of O_2 at 0.75 GPa with Uiso parameter displayed at 50 %. Each colour represents symmetry independent site as above. The green circles note the sites which are well ordered (those which lie in the 4MR and 6MR windows) and the blue and red circles note the diffuse sites (in the central pore).

For example, N_2-6 and O_2-6 sites are in the centre of the pore (in magenta in **Figure 4.10**), due to the symmetry imposed in the crystal structure (*I*-43*m*) symmetry equivalent sites are generated through a four-fold operation to create a tetrahedral motif in the central pore. However, the simulations were run in the absence of symmetry and in fact the site was much less ordered, and did not maintain the tetrahedral motif. This helped explain the large crystallographic Uiso value, as in average time and space the location of the adsorption site would be random in the centre of the pore. The case was similar for N_2-5 and O_2-5, which also had large crystallographic Uiso values and the reason for that was explained from the positions obtained from the simulation. The site was not present at all symmetry equivalent locations throughout the unit cell used to model the adsorption behaviour. So in reality, an occupancy of one (fully occupied) would not be expected for the site, which is the reason the Uiso value is increased compared to N_2-1 to N_2-4 or O_2-1 to O_2-4. Intuitively, all the behaviour shown in both the crystal structure and the simulation can be traced back to the energy of each adsorption site. Instinctively, the most negative interaction energies (i.e. the strongest adsorption sites) were the most ordered in the simulation and crystal structure, and as framework – guest interaction energies became less favourable, the position of the sites were more disordered. The strongest sites for both gases were O_2-1 to 3, N_2-1 to -3. These were located in the 6MR, on to the π cloud of the MeIm ring and in the 4MR, respectively.

These strongly interacting sites for each diatomic have comparable interaction energies ranging between -22 to -12 kJ mol^{-1}., as seen in **Figure 4.11** which show the centre of mass of each diatomic and its interaction energy with the framework The broad range of energies comes from the position of the

diatomic molecule with respect to the framework. For example in ZIF-8-N_2 the interaction energy is reduced if N_2-1 does not sit exactly in the plane and if the molecule is not orientated exactly in the centroid of the plane. In addition, there is an energy penalty if the N_2-2 site is found closer to ZIF-8, decreasing from -14 kJ mol^{-1} to -12 kJ mol^{-1}, as the distance from N_2-COM shortens from 4.313 Å to 2.639 Å. Site four, N_2-4 and O_2-4, is located below the 4MR window with energies in the region of -12 to -9 kJ mol^{-1}. By analysing the multiple orientations calculated from the GCMC simulations, it was clear why the resulting crystallographic position of O_2-4 had an increased Uiso value. The GCMC positions showed a wide spread of orientations below the 4-MR ring, which could mean that there is no preferred orientation for pointing to either the methyl group or the bond of the MeIm. Adsorption sites one to four were the easiest to locate and the most prominent in both the GCMC simulation and crystal structures, which confirms their full occupancy noted in the crystallographic refinement.

As previously mentioned, the last two sites were much more diffuse in their positions and had very weak interaction energies with the framework, around -3 kJ mol^{-1}, and were not present at every N_2-5 and N_2-6 or O_2-5 and O_2-6 site during the GCMC simulations. As there is no symmetry imposed during the GCMC simulation, unlike the diffraction experiment where cubic *I*-43*m* symmetry is imposed on the unit cell, this helped confirm that these sites were not fully occupied. This also helped confirm why there was a difficulty in finding the electron density corresponding to these crystallographic sites.

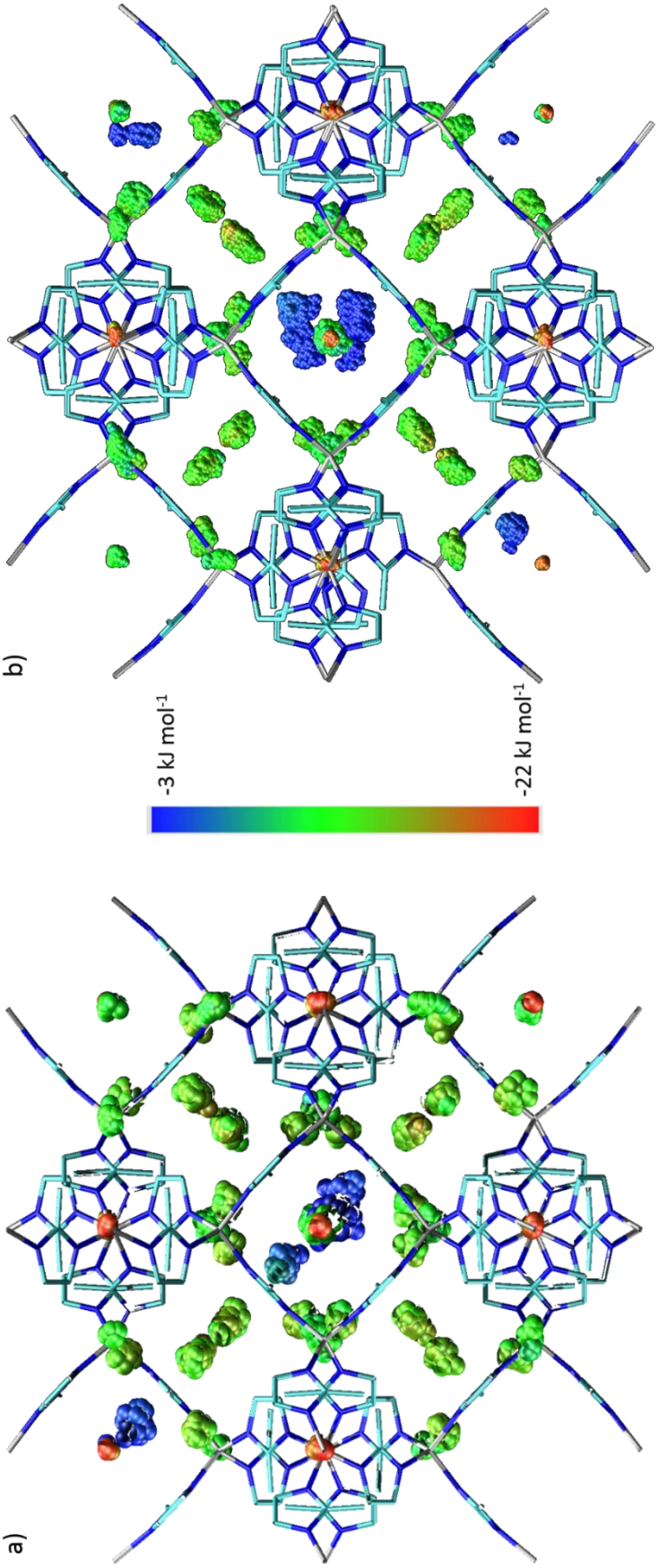

Figure 4.11 (a) Heat map of N_2 in ZIF-8HP. (b) Heat map of O_2 in ZIF-8HP. Points are centre of masses of diatomic molecules and colour of point represents the energy. Where red is a low energy (strong interaction) and blue is a high energy (weak interaction).

4.5 Conclusions

Using high-pressure crystallography, O_2, N_2, Ar and CH_4 were successfully loaded into ZIF-8 to determine the adsorption sites inside the framework. By using a cryogenic method of loading, extreme pressures were used as a tool to force liquefied "gases" into the framework, thus building up occupancy of the gas in the framework and allowing for the first time high resolution high-pressure single crystal X-ray diffraction experiments to locate the adsorption sites. The wide variety in behaviour confirms the suggestion, in previous work crystallographic work by the Moggach group and others that PTMs play a dynamic role in high-pressure studies of MOFs and their role should not be underestimated.[5, 37, 40, 46] The energies of these crystallographically determined sites could then be calculated with GCMC simulations. The GCMC simulations for the diatomics in ZIF-8-O_2 and ZIF-8-N_2 helped explain a number of unanswered questions from the crystallographic data, including the hierarchy of adsorption sites, the low occupancies and the disorder of the small molecules seen crystallographically. Due to the crystallographic disorder it was impossible at ambient temperature to locate the full diatomic at this site, so in future a combined low temperature- high-pressure experiment could be carried out and this could help to freeze out any dynamic disorder present making the modelling of the guest molecules much more straightforward. The simulations also gave valuable information to confirm the orientation of the molecules in the pores. This work has helped to understand, for a SOD-topology MOF what interactions are the most favourable, and which gases have the strongest interaction energy with framework. With this information, it is possible to begin to think of developing

MOFs to maximise these favourable interactions and can progress the field of MOFs to having even better selective gas storage properties.

4.6 References

1. S. Chavan, J. G. Vitillo, D. Gianolio, O. Zavorotynska, B. Civalleri, S. Jakobsen, M. H. Nilsen, L. Valenzano, C. Lamberti, K. P. Lillerud and S. Bordiga, *Phys. Chem. Chem. Phys.*, 2012, **14**, 1614-1626.
2. J. W. Liu, L. F. Chen, H. Cui, J. Y. Zhang, L. Zhang and C. Y. Su, *Chem. Soc. Rev.*, 2014, **43**, 6011-6061.
3. R. A. Smaldone, R. S. Forgan, H. Furukawa, J. J. Gassensmith, A. M. Z. Slawin, O. M. Yaghi and J. F. Stoddart, *Angew. Chem. Int. Ed.*, 2010, **49**, 8630-8634.
4. K. S. Park, Z. Ni, A. P. Cote, J. Y. Choi, R. D. Huang, F. J. Uribe-Romo, H. K. Chae, M. O'Keeffe and O. M. Yaghi, *Proc. Natl. Acad. Sci. U.S.A.*, 2006, **103**, 10186-10191.
5. S. A. Moggach, T. D. Bennett and A. K. Cheetham, *Angew. Chem. Int. Ed.*, 2009, **48**, 7087-7089.
6. A. S. Huang, Q. Liu, N. Y. Wang, Y. Q. Zhu and J. Caro, *J. Am. Chem. Soc.*, 2014, **136**, 14686-14689.
7. D. Fairen-Jimenez, R. Galvelis, A. Torrisi, A. D. Gellan, M. T. Wharmby, P. A. Wright, C. Mellot-Draznieks and T. Duren, *Dalton Trans.*, 2012, **41**, 10752-10762.
8. H. Wu, W. Zhou and T. Yildirim, *J. Am. Chem. Soc.*, 2007, **129**, 5314-5315.
9. H. Wu, W. Zhou and T. Yildirim, *J. Phys. Chem. C*, 2009, **113**, 3029-3035.
10. E. J. Carrington, I. J. Vitorica-Yrezabal and L. Brammer, *Acta Crystallogr. Sect. B-Struct. Sci.*, 2014, **70**, 404-422.
11. A. L. Goodwin, D. A. Keen and M. G. Tucker, *Proc. Natl. Acad. Sci. U.S.A.*, 2008, **105**, 18708-18713.
12. A. B. Cairns, A. L. Thompson, M. G. Tucker, J. Haines and A. L. Goodwin, *J. Am. Chem. Soc.*, 2012, **134**, 4454-4456.
13. T. D. Bennett, A. L. Goodwin, M. T. Dove, D. A. Keen, M. G. Tucker, E. R. Barney, A. K. Soper, E. G. Bithell, J. C. Tan and A. K. Cheetham, *Phys. Rev. Lett.*, 2010, **104**, 15503.
14. K. S. Park, Z. Ni, A. P. Côté, J. Y. Choi, R. Huang, F. J. Uribe-Romo, H. K. Chae, M. O'Keeffe and O. M. Yaghi, *Proc. Natl. Acad. Sci. U.S.A.*, 2006, **103**, 10186-10191.
15. X. C. Huang, Y. Y. Lin, J. P. Zhang and X. M. Chen, *Angew. Chem. Int. Ed.*, 2006, **45**, 1557-1559.
16. W. Zhou, H. Wu, M. R. Hartman and T. Yildirim, *J. Phys. Chem. C*, 2007, **111**, 16131-16137.
17. C. J. Ridley and K. V. Kamenev, *Z. Kristallogr.*, 2014, **229**, 171-199.
18. J. B. Parise, *Rev. Mineral. Geo. Chem.*, 2006, **63**, 205-231.
19. J. Sotelo, C. H. Woodall, D. R. Allan, E. Gregoryanz, R. T. Howie, K. V. Kamenev, M. R. Probert, P. A. Wright and S. A. Moggach, *Angew. Chem. Int. Ed.*, 2015, **54**, 13332-13336.
20. S. A. Moggach, D. R. Allan, S. Parsons and J. E. Warren, *J. Appl. Crystallogr.*, 2008, **41**, 249-251.
21. G. J. Piermarini, S. Block, J. D. Barnett and R. A. Forman, *J Appl Phys*, 1975, **46**, 2774-2780.
22. A. Dawson, D. R. Allan, S. Parsons and M. Ruf, *J. Appl. Crystallogr.*, 2004, **37**, 410-416.
23. Bruker, ed. ECLIPSE, Madison, Wisconsin, USA, 2006.
24. G. M. Sheldrick, University of Göttingen, Germany., 2008.
25. Bruker, ed. XPREP, Madison, Wisconsin, USA, 2004.
26. K. S. Park, Z. Ni, A. P. Côté, J. Y. Choi, R. Huang, F. J. Uribe-Romo, H. K. Chae, M. O'Keeffe and O. M. Yaghi, *Proc. Natl. Acad. Sci. U.S.A*, 2006, **103**, 10186-10191.

27. P. W. Betteridge, J. R. Carruthers, R. I. Cooper, K. Prout and D. J. Watkin, *J. Appl. Crystallogr.*, 2003, **36**, 1487-1487.
28. A. L. Spek, *J. Appl. Crystallogr.*, 2003, **36**, 7-13.
29. C. F. Macrae, I. J. Bruno, J. A. Chisholm, P. R. Edgington, P. McCabe, E. Pidcock, L. Rodriguez-Monge, R. Taylor, J. van de Streek and P. A. Wood, *J. Appl. Crystallogr.*, 2008, **41**, 466-470.
30. S. J. Clark, M. D. Segall, C. J. Pickard, P. J. Hasnip, M. I. J. Probert, K. Refson and M. C. Payne, *Z. Kristallogr.*, 2005, **220**, 567-570.
31. D. F. Shanno, *Math. Comput.*, 1970, **24**, 647.
32. D. Frenkel and B. Smit, Academic Press, San Diego, Second edn., 2002, pp. 1-638.
33. A. Gupta, S. Chempath, M. J. Sanborn, L. A. Clark and R. Q. Snurr, *Mol. Simul.*, 2003, **29**, 29-46.
34. M. J. McGrath, J. N. Ghogomu, N. T. Tsona, J. I. Siepmann, B. Chen, I. Napari and H. Vehkamaki, *J. Chem. Phys.*, 2010, **133**, 084106
35. D. Wolf, P. Keblinski, S. R. Phillpot and J. Eggebrecht, *J. Chem. Phys.*, 1999, **110**, 8254-8282.
36. R. C. Reid, J. M. Prausnitz and B. E. Poling, *The properties of gases and liquids*, Fourth edn., McGraw-Hill, London, 1987.
37. A. J. Graham, D. R. Allan, A. Muszkiewicz, C. A. Morrison and S. A. Moggach, *Angew. Chem. Int. Ed.*, 2011, **50**, 11138-11141.
38. Y. A. Freiman and H. J. Jodl, *Phys. Rep.*, 2004, **401**, 1-228.
39. C. L. Hobday, R. J. Marshall, C. F. Murphie, J. Sotelo, T. Richards, D. R. Allan, T. Duren, F. X. Coudert, R. S. Forgan, C. A. Morrison, S. A. Moggach and T. D. Bennett, *Angew. Chem. Int. Ed.*, 2016, **55**, 2401-2405.
40. K. W. Chapman, G. J. Halder and P. J. Chupas, *J. Am. Chem. Soc.*, 2008, **130**, 10524-10526.
41. B. Zheng, M. Sant, P. Demontis and G. B. Suffritti, *J. Phys. Chem. C*, 2012, **116**, 933-938.
42. H. Tanaka, S. Ohsaki, S. Hiraide, D. Yamamoto, S. Watanabe and M. T. Miyahara, *J. Phys. Chem. C*, 2014, **118**, 8445-8454.
43. Y. Akahama and H. Kawamura, *Chem. Phys. Lett.*, 2004, **400**, 326-330.
44. C. O. Ania, E. García-Pérez, M. Haro, J. J. Gutiérrez-Sevillano, T. Valdés-Solís, J. B. Parra and S. Calero, *J. Phys. Chem. Lett.*, 2012, **3**, 1159-1164.
45. W. Morris, C. J. Stevens, R. E. Taylor, C. Dybowski, O. M. Yaghi and M. A. Garcia-Garibay, *J. Phys. Chem. C*, 2012, **116**, 13307-13312.
46. K. W. Chapman, G. J. Halder and P. J. Chupas, *J. Am. Chem. Soc.*, 2009, **131**, 17546-17547.

-Chapter Five-

Understanding the Mechanical Properties of Zr-MOFs with Experiment and Theory

5.1 Synopsis

This chapter covers the synthesis and characterisation of the physical properties of a series of Zr-containing metal-organic frameworks (MOFs). The isoreticular series of UiO-type MOFs consist of $Zr_6O_4(OH)_4$ nodes interconnected by linear or bent dicarboxylate ligands.[1, 2] The high valency of Zr(IV) and 12-fold coordination of the metal cluster are associated with high shear and bulk moduli, which surpass those of other MOFs.[8] This chapter presents a combined computational and experimental study of the mechanical behavior of UiO-67 [$Zr_6O_4(OH)_4(bpdc)_6$] (bpdc: 4,4'-biphenyl dicarboxylate)[9] and an azobenzene derivative, UiO-abdc [$Zr_6O_4(OH)_4(abdc)_6$] (abdc: 4,4'-azobenzene dicarboxylate).[10] A combination of single-crystal nanoindentation, high-pressure X-ray diffraction studies, density functional theory (DFT) calculations, and first-principles molecular dynamics (MD) simulations, which are explained in full detail in Chapter Two, are used to show that the dynamic disorder induced in UiO-abdc by the ligand has a significant impact upon the mechanical behavior of the framework.

5.2 Introduction

Metal-organic frameworks (MOFs) continue to be of exceptional interest to the scientific community because of their guest-specific gas sorption, separation, drug-delivery and catalytic properties.[11, 12] Whilst significant progress has been made in increasing the chemical stability of MOFs,[13] their 'soft' mechanical properties often lead to framework collapse or structural distortion upon application of temperature, shear stress or hydrostatic pressure.[14] It is logical that MOFs have lower mechanical stabilities than dense materials as MOFs are

metastable structures, that is, the structures represent a local energy minimum rather than the thermodynamic energy minimum of the potential energy landscape. This poses a severe problem during sintering and pelletization processes, used to shape MOF powders into industrially useful morphologies.[15, 16] Any structural deformation however also alters the highly selective, specific guest-binding properties of MOFs, meaning structural durability is therefore a highly desired quality. Routes to such mechanically robust structures have included embedding MOFs into polymer matrices, or coating nanoparticles with silica,[17] though both lead to substantial deterioration in guest sorption ability.

While sometimes problematic for applications, structural flexibility does however give rise to a very rich and diverse array of pressure- and temperature-induced mechanical responses in MOFs, which may be tuned to individual application needs.[18-23] The importance of this mechanical behavior was the motivation behind this chapter to investigate the link between stimuli-induced mechanical response and chemical structure in the well-known UiO family of Zr-MOFs.

5.2.1 Mechanical properties

The mechanical properties of a material can be defined in a variety of ways. These properties can be calculated by subjecting a stress (load) on the material in a particular direction and measuring the induced strain. These stress/strain

relationships come in a variety of forms, some of the most common are outlined in **Figure 5.1**.

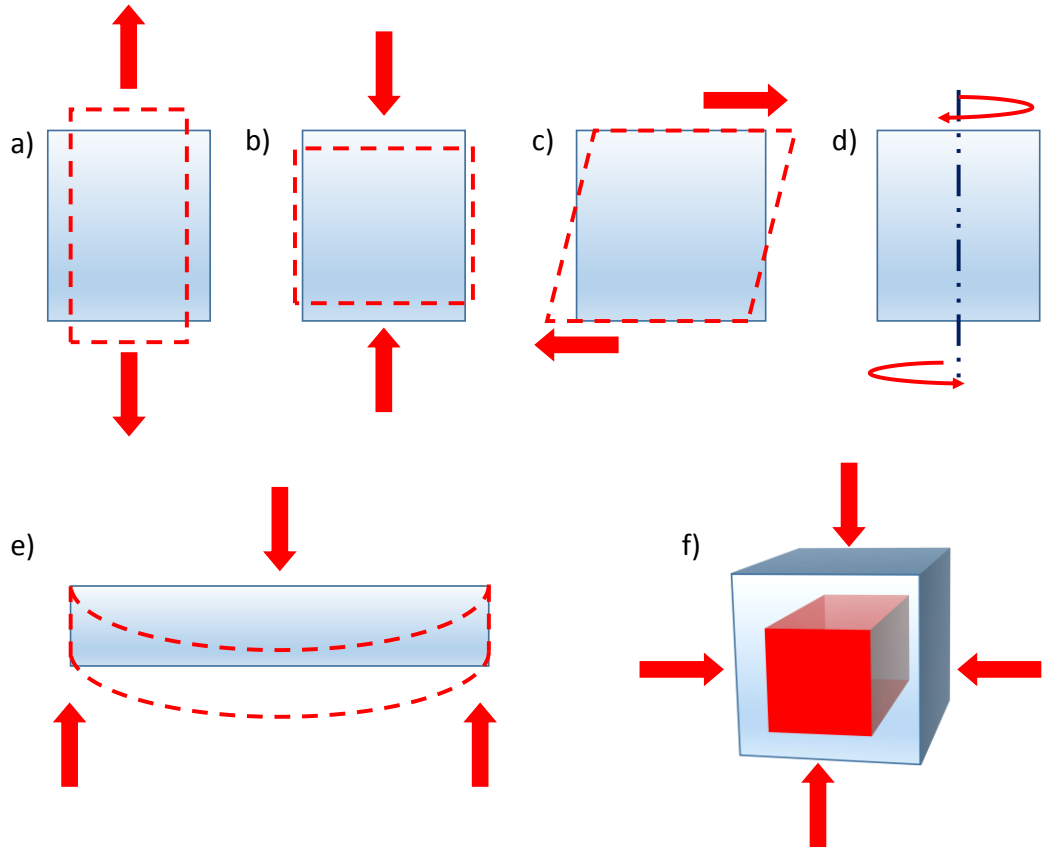

Figure 5.1: Diagrams outlining the major modes of mechanical loading: (a) uniaxial tension, (b) uniaxial compression, (c) shear strain, (d) torsion, (e) bending and (f) hydrostatic compression. The arrows note the direction of the stress. The blue and red boxes represent the effect before, and after the applied stress respectively.. Illustration adapted from Tan *et al.*[3]

Three particularly important measures of mechanical strength are the shear modulus (G_{min}), Young's modulus (E) and bulk modulus (K). G_{min} and E are relevant to the MOF's durability during shaping into films or membranes.[3] Whilst K is important to understand adsorption processes occurring in the MOF adsorption community. The methods chapter outlines experimental and computational methods for determining some of these properties, including

nanoindentation, high-pressure crystallography and elastic stiffness tensor calculations.

5.2.2 UiO-MOFs

The isoreticular series of UiO-type MOFs, named after the Lillerud group at the University of Oslo who first synthesised them, are built from $Zr_6O_4(OH)_4$ nodes, which are interconnected by dicarboxylate ligands.[1, 2] These systems are widely studied as they have been shown to exhibit great thermal, aqueous and acid stability.[9] The building blocks of the original UiO framework, UiO-66, are $Zr_6O_4(OH)_4$ nodes connected by 1,4-benzenedicarboxylate linkers.[9] The frameworks which are the main focus of this chapter are UiO-67 and UiO-abdc, which differ from the original MOF by having longer linkers of biphenyl-4,4'-dicarboxylate and 4,4-azobenzene-dicarboxylate, respectively (**Figure 5.2**).[9, 10] The advantage of studying UiO-67 and UiO-abdc is that while they possess similar features to that of the robust UiO-66, single crystals of the UiO-67 and UiO-abdc can be easily synthesised, making it possible to study the materials by single crystal X-ray diffraction. Synthetic conditions leading to single-crystals of UiO-type MOFs are rare and typically require the addition of a significant excess of monocarboxylic acid crystallization modulators.[24, 25] The modulation process involves an additional species, usually a monocarboxylic anion, e.g. benzoic acid, and is in equilibrium with the organic linker to bind to the SBU $[Zr_6O_4(OH)_4]^{12+}$. It is thought that using a modulator influences crystal nucleation and growth due to the competition for the coordination sites at $[Zr_6O_4(OH)_4]^{12+}$ clusters. In addition to these native structures, many derivatives have also been synthesised with functionalised linkers to create frameworks incorporating amino, halogen, hydroxyl or nitro groups.[2] UiO-66 is difficult to grow single crystals of with a modulator

method, due to the small length of the linker, 1,4-benzenedicarboxylate (BDC), creating small pores which trap the modulator and cause poor competition between the modulator and linker. This leads to a high degree of missing linkers and results in correlated disorder. This is what was found by Lillerud *et al.* when they used a benzoic modulator approach for the synthesis of single crystals of UiO-66. A route to defect free single crystals of UiO-66 has still not been found despite the modulator approach working for a wide variety of Zr-based MOFs.[26] We have found the amino acid *L*-proline to be a highly efficient modulator in the synthesis of Zr UiO-MOFs.[27] Addition of 5 and 1 equivalents (with respect to the linker) of L-proline and HCl (a known synthetic promoter[28]) during solvothermal syntheses yields single crystals of ~50-100 μm diameter of both UiO-67 and UiO-abdc (**Figure 5.2**). Both UiO-67 and UiO-abdc crystallise in the cubic space group *Fm*-3*m* ($a \approx 26.85$ Å and 29.32 Å respectively), and contain octahedral cages of diameter 16 Å (UiO-67) and 19 Å (UiO-abdc), which face share with eight smaller tetrahedral pores of diameters 12 Å (UiO-67) and 15 Å (UiO-abdc).[10]

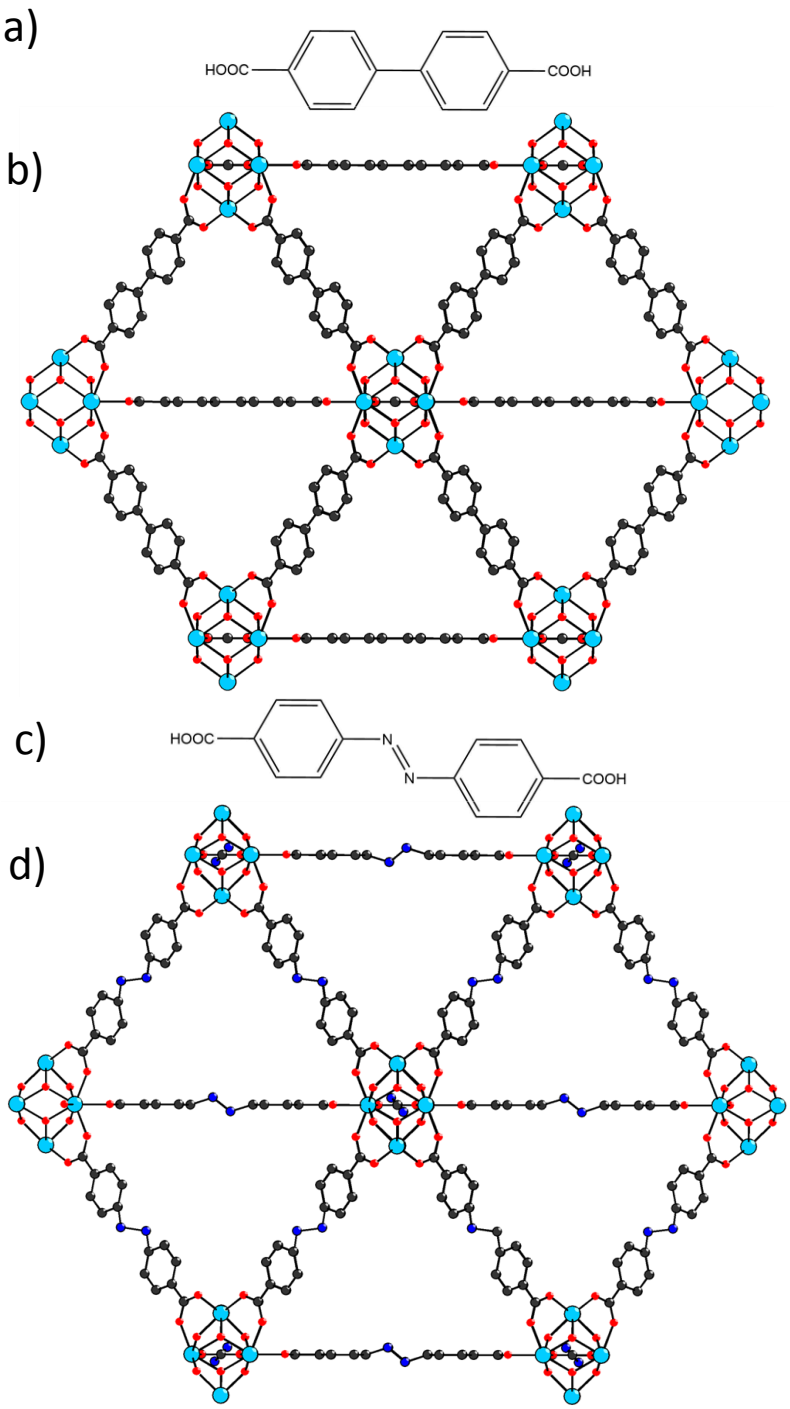

Figure 5.2: (a) Chemical drawing of biphenyl-4,4′-dicarboxylic acid (b) and Unit cell of UiO-67. (c) Chemical drawing of 4,4-azobenzene-dicarboxylic acid (d)Unit cell of UiO-abdc. Both MOFs are face centred cubic structures with an octahedral central pore, surrounded by smaller tetrahedral pores. Zirconium - light blue, oxygen – red, carbon – back and nitrogen – dark blue. H-atoms are omitted for clarity.

The high valency of Zr(IV) and 12-fold coordination of the metal cluster are associated with high calculated shear and bulk moduli, which surpass those of other MOFs.[8] In **Table 5.1** the UiO-MOFs are compared to archetypal MOFs, MOF-5; ZIF-8 and HKUST-1.[28] The inorganic nodes (based on Cu(II) and Zn(II)) used in these MOFs represent a large portion of rigid MOFs in the field. The bulk modulus value of UiO-66 is very high compared to these MOFs, being almost twice that of MOF-5 and three and a half times larger than ZIF-8. This makes UiO-66 one of the most mechanically strong MOFs known. UiO-66 is more porous than ZIF-8, it appears, perhaps counterintuitively, that low porosity is not the determining factor in achieving a high *K*. It appears that the higher coordination number of the node-linker plays a vital role. If the ratio of metal centre – linker coordination to metal- O/N is more than 1:1 the resulting structure is more likely to have a higher bulk modulus value.[20] One main reason that the UiO set of MOFs have captured so much attention in the engineering world is their stability to mechanical stress in addition to their thermal and chemical inertness.

Table 5.1: Bulk modulus, shear modulus and porosity values of common porous MOFs. Porosities were calculated from density functional theory (DFT)-optimised crystal structures using the PLATON.[29] Table adapted from Wu *et al.* [8]

MOF	Inorganic node	Organic linker	Node-O/N coordination	Node-linker coordination	Porosity (%)	Bulk modulus K (GPa)	Shear modulus G_{min} (GPa)
UiO-66	$Zr_6O_4(OH)_4$	BDC	8	12	52.6	31.85	13.75
UiO-67	$Zr_6O_4(OH)_4$	BPDC	8	12	67.7	17.15	5.69
MOF-5	Zn_4O_{13}	BDC	4	6	76.5	18.20	1.66
ZIF-8	ZnN_4	MeIm	4	4	45.8	9.23	0.94 – 0.97
HKUST-1	Cu_2O_8	BTC	5	4	68.7	24.53	1.04

5.3 Experimental

Note: the synthesis of materials was carried out by Mr Ross Marshall, Mr Colin Murphie and Dr Ross Forgan of the University of Glasgow.

5.3.1 Synthesis

UiO-67: $ZrCl_4$ (0.210 g, 0.90 mmol, 1 eq.), biphenyl-4,4′-dicarboxylic acid (0.218 g, 0.90 mmol, 1 eq.) and L-proline (0.500 g, 4.50 mmol, 5 eq.) were added to a 50 ml screw top Pyrex jar. 20 ml of dimethylformamide (DMF) was added then HCl (0.08 ml) was added. The reaction mixture was sonicated for several minutes until a homogeneous white suspension remained. The white suspension was transferred to an acid digestion vessel and sealed before being placed in the oven at 120 °C for 24 hours. The reaction vessel was removed from the oven and allowed to cool to room temperature. The contents of the acid digestion vessel were removed by pipette and added to a 50 ml centrifuge tube. The reaction DMF was exchanged for fresh DMF several times. The crystals were retained in DMF before being analysed by single crystal X-ray diffraction (SCXRD).

UiO-abdc: $ZrCl_4$ (0.052g, 0.225 mmol, 1 eq.), 4,4-azobenzenedicarboxylic acid (0.061 g, 0.225 mmol, 1 eq.) and L-proline (0.104 g, 0.900 mmol, 4 eq.) were added to a 50 ml screw top Pyrex jar. 10 ml of DMF was added and the jar was placed in a sonicator for 5 minutes. HCl (0.02 ml) was added to the resulting suspension and the jar was placed in a sonicator for 5 minutes. The glass jar was placed in the oven at 100 °C for 48 hours. The glass jar was removed from the oven and allowed to cool to room temperature. The reaction DMF was exchanged for fresh DMF several times. The crystals were retained in DMF before being analysed by SCXRD.

5.3.2 *Nanoindentation*

Note: the nanoindentation of materials was carried out by Dr Tom Bennett at the University of Cambridge.

Nanoindentation experiments were performed using an MTS Nanoindenter XP, located in an isolation cabinet to shield against thermal fluctuations and acoustic interference. Samples were first mounted using an epoxy resin, which was then ground away using a silicon carbide disc, before being polished using increasingly fine diamond suspensions. Indentations were conducted under the dynamic displacement-controlled "continuous stiffness measurement" mode. *E* (Young's Modulus) and *H* (Hardness) were subsequently determined as a function of the surface penetration depth. A 2 nm sinusoidal displacement at 45 Hz was superimposed onto the system's primary loading signal, and the loading and unloading strain rates were set at $5\times10^{-2}\,s^{-1}$. All tests were performed to a maximum indentation depth of 500 nm (unless otherwise stated) using a Berkovich (i.e., three-sided pyramidal) diamond tip of radius ~ 100 nm. The raw data (load-displacement curves) obtained were analysed using the Oliver and Pharr method.[30]

5.3.3 *Face-indexing and structure determination*

Face-indexing measurements used to determine the crystal faces being indented were performed at room temperature, using an Oxford diffraction SuperNova X-ray diffractometer with Cu k_α radiation (=1.540598 Å) with an Atlas CCD detector. Data were collected in ω-scans in four settings of 2θ and ϕ with a step size of 1°. Exposure times for UiO-67 were 60 s at low angle and 180 s at high angle, whilst exposure times for UiO-abdc were 1 s and 40 s at low angle and high angle respectively. Data processing, unit cell determination and face indexing were carried out using the program

CrysAlisPro. **Tables 5.2** and **5.3** and **Figures 5.3** and **5.4** contains the main crystallographic parameters and different views of the indexed crystals.

Tale 5.2: Summary of face indexing statistics for UiO-67

UiO-67		
Crystal system	Cubic	
Space group	*Fm*-3*m*	
Unit cell dimensions	*a* = 26.8042(2)	$\alpha = 90$
(Å, °)	*b* = 26.8042(2)	$\beta = 90.$
	c = 26.8042(2)	$\gamma = 90$
Volume (Å^3)	19257.9(3)	
Crystal size (mm)	0.049 x 0.061 x 0.071	
Main crystal faces	(1 1 1), (-1 1 1), (1 -1 1), (1 1 -1), (1 -1 -1), (-1 1 -1), (-1 -1 1) (-1 -1 -1)	

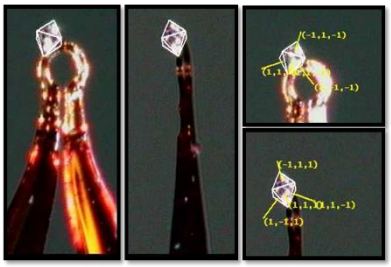

Figure 5.3: Face-normals of principal faces of the crystal, note the triangular shaped faces (1 1 1), (-1 1 1), (1 -1 1), (1 1 -1), (1 -1 -1), (-1 1 -1), (-1 -1 1) and (-1 -1 -1)

Table 5.3:: Summary of face indexing statistics for UiO-abdc

UiO-abdc		
Crystal system	Cubic	
Space group	*Fm*-3*m*	
Unit cell dimensions	a = 29.4065(2)	$\alpha = 90$
(Å, °)	b = 29.4065(2)	$\beta = 90$
	c = 29.4065(2)	$\gamma = 90$
Volume (Å^3)	25429.2(3)	
Crystal size (mm)	0.047 x 0.062 x 0.073	
Main crystal faces	(1 1 1), (-1 1 1), (1 -1 1), (1 1 -1), (1 -1 -1), (-1 1 -1), (-1 -1 1),(-1 -1 -1)	

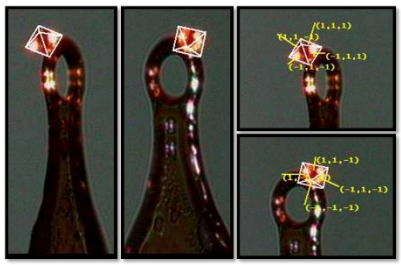

Figure 5.4: Face-normals of principal faces of the crystal, note the triangular shaped faces (1 1 1), (-1 1 1), (1 -1 1), (1 1 -1), (1 -1 -1), (-1 1 -1), (-1 -1 1) and (-1 -1 -1)

5.3.4 High-pressure crystallography

Synchrotron radiation high pressure single crystal measurements. A single crystal was loaded into a Merrill-Bassett diamond anvil cell (DAC) with a half-opening angle of 40 degrees, composed of Boehlar Almax diamonds with 600μm culet diamond anvils, a tungsten gasket and tungsten carbide backing plates.[31] The appropriate hydrostatic pressure medium was added. A small ruby chip was also loaded into the cell to act as a pressure calibrant, using the pressure dependent fluorescence of the ruby to measure the pressure.[32] Diffraction data were collected on station I19 at the Diamond Light Source, Rutherford Appleton Laboratory, on a Huber 4-circle goniometer with a Rigaku Saturn 724 CCD detector using synchrotron radiation (wavelength = 0.5159 Å) from 0.14 GPa to 3.80 GPa. Data collection was carried out using an exposure time and a step size of 1 second and 0.5 degrees respectively. The data were integrated with the program SAINT using dynamic masks (these mask the regions of the detector which are shaded due to the pressure cell).[33, 34] Omission of shaded reflections, absorption correction and merging of data were carried out in a three-step process, firstly with the program SHADE, then SADABS and finally XPREP.[35-37]

Laboratory high pressure single crystal measurements. A suitable single crystal was placed in a Merrill-Bassett DAC composed of a tungsten gasket, 600μm diamond culets and tungsten carbide backing discs with a half opening angle of 40 degrees.[31] The appropriate hydrostatic pressure medium was added and small ruby chip was also loaded into the cell to act as a pressure calibrant, as previously described. High pressure diffraction data were collected on a Bruker APEX II diffractometer with graphite-monochromated Mo K_α radiation (0.71073 Å). Data were collected from 0.1 GPa to 0.9 GPa in

omega scans in eight settings of 2θ and φ with an exposure time of 100 s and a step size of 0.5°. The data were integrated using dynamic masks and absorption corrections for the DAC and sample were carried out with the programs SHADE and SADABS, respectively. [33-37]

Structure refinements were carried out in CRYSTALS.[38] The structure was solved by SUPERFLIP.[39] All structures were refined anisotropically against *F* with an I/σ cut-off of -3, to reject weak reflections. All 1,2 and 1,3 distances for the organic linker (biphenyl dicarboxylate or azobenzenedicarboxylate for UiO-67 and UiO-abdc respectively) were restrained, whilst all torsion angles and metal – ligand bond distances were allowed to freely refine. Vibrational and thermal similarity restraints were also applied to the organic linker. Hydrogen atoms on the linker were placed geometrically and constrained to ride on their host atoms. The pore volume and electron count per unit cell were calculated using the SQUEEZE algorithm within PLATON.[29]

5.3.5 Ab-initio molecular dynamics

All *ab initio* (Born-Oppenheimer) MD calculations were performed using the Quickstep module of the CP2K (version 2.6) simulation package.[40] The BLYP[41, 42] exchange-correlation functional with semi-empirical dispersion corrections to the energies and gradients from the DFT-D3[43] method (cut-off radius 10 Å) where used throughout. Energies and forces were calculated utilizing the Gaussian plane-wave scheme, which is a dual basis set method wherein a linear combination of Gaussian-type orbitals is used to describe the Kohn-Sham molecular orbitals while the electron density is described by an auxiliary plane-wave basis set (expressed at an energy cut-off of 350 Ry, accompanied by the relative cutoff of 50 Ry for the Gaussian basis set collocation). The

double-zeta quality MOLOPT basis set[44-47] was used for all elements, in conjunction with the relativistic, norm-conserving Goedecker-Teter-Hutter pseudopotentials, optimised for use against the BLYP functional. During each SCF cycle, the electronic structure was explicitly minimised to a tolerance of 10^{-7} Hartree. The equations of motion were integrated using a time step of 0.55 fs. The use of these particular functionals, basis sets and potentials were chosen to study dynamics in UiO- MOFs as these have already been tested for microporous systems which illustrate dynamic behaviour such as MIL-53(Sc).[48]

The crystallographic models of both UiO-67 and UiO-abdc were recast to their primitive cell settings, thereby reducing the volume of the crystallographic unit cells to a quarter of their conventional setting, and presenting a considerable cost-saving for the modelling work. However, this still resulted in relatively large unit cell models ($a = b = c = ca.$ 20 Å, $\alpha = \beta = \gamma = 60°$), which by definition results in compact 1st Brillouin zones. Thus, the constraint that the QUICKSTEP module employs Γ-point sampling only of the Brillouin zone was not a concern in this work. For the crystallographically disordered UiO-abdc, equilibration of the model was initiated under the isobaric-isothermal ensemble regime (NPT; constant number of particles, pressure and temperature) for 4 ps. The temperature was set to 300 K and controlled by a chain of Nosé-Hoover thermostats[49] coupled to every degree of freedom (the so-called massive thermostat) with a frequency of 4000 cm^{-1}, which is high enough to properly sample the fast vibrational motion of the O-H bond in the ZrO cluster of the UiO-67-based MOFs. The barostat was set up with a coupling time constant of 300 fs and an external pressure of 1 bar. In addition, a reference unit cell of constant volume was defined alongside the model of

UiO-abdc to fix the number of grid points used to compute the Coulomb and exchange-correlation energies. This was used to mitigate any effects of varying grid points due to potential volume fluctuations of the simulation box (due to large breathing motions of UiO-abdc). It has been shown previously that the use of such a reference cell avoids any discontinuities in the potential energy profile when the volume is permitted to vary.[48, 50, 51] However, minimal (2 %) unit cell expansion was observed by this process. The unit cell parameters were then fixed at the equilibrated values, and the ensemble switched to NVT for production run dynamics (4 ps). For UiO-67, with rigid linker geometry even less unit cell expansion was anticipated; for this reason, system equilibration (1 ps) and production run dynamics (4 ps) were all performed in the NVT ensemble (with same settings as listed above for UiO-abdc). The resulting trajectories were then analysed numerically to determine the time-averaged mean atomic positions (which are simply the coordinates for each atom averaged over all frames from the production run data set), and to calculate the atomic probability density functions (via numerical calculation of the variances and co-variances of each atom, using methods described previously).[52-54] The later are analogous to the thermal ellipsoid model used in crystallographic refinements, and are displayed in in the main text at the standard 50% probability level. The output data were then processed graphically using Mercury CSD 3.3.1.[55] The time-average atomic positions were suitable models to use as starting points for geometry optimization calculations (reported in the following section).

5.3.6 DFT-D isotropic compression

All calculations were performed using the CASTEP (version 5.11) simulation package.[56] The Hamiltonian operator was approximated using the Perdew-

Burke-Ernzerhof (PBE) exchange-correlation functional, with the molecular wavefunction description provided by 'on-the-fly' pseudopotentials and a plane wave basis set operating at 650 eV, which gave convergence to within 4 meV per atom. In addition, a Tkatchenko-Scheffler dispersion correction was applied.[57, 58] The electronic structure was sampled at the gamma position only in the Brillouin zone due to the large size of the primitive unit cell (resulting in a k-point sampling grid of no greater than 0.06 $Å^{-1}$). The geometry optimisation calculations, which took the time-averaged mean atomic position models derived from the MD production trajectories as input, were run without any symmetry constraints, thus allowing for an independent variation of both the atomic positions and the primitive cell parameters. The potential energy surface was searched for energy minima by means of the Broyden-Fletcher-Goldfarb-Shanno (BFGS) algorithm.[59] Structures were considered to be optimised when the energy per atom, maximum force, maximum stress, and maximum atomic displacement converged to the values of 0.02 meV $atom^{-1}$, 0.05 eV $Å^{-1}$, 0.1 GPa, and 0.002 Å, respectively. Once the first, ambient pressure, model was optimised, an external hydrostatic pressure of 0.2 GPa was applied and the system re-optimised; this process was repeated at 0.2 GPa steps until an external pressure of 1 GPa was reached. After 1 GPa, the optimization of UiO-abdc could not be achieved as the structure had reached the limit of sensible bonding.

5.3.7 Elastic stiffness tensor calculations

Note: the elastic stiffness tensor calculations were carried out by Dr F-X Coudert of Institut de Recherche de Chimie Paris.

DFT calculations of the elastic stiffness tensors (second-order elastic constants) of both UiO-67 and UiO-abdc were performed at the quantum mechanical

level, in the density functional theory approach with localised basis sets (CRYSTAL14 code[60]). We used the PBESOL0 hybrid exchange-correlation functional[61] and all-electron basis sets for all atoms, following the methodology established for both structural and mechanical properties on UiO-66.[62, 63] The accuracy of this methodology is now well established for the calculation of MOF structures,[64] energies,[65] and elastic constants.[66, 67]Elastic stiffness tensors were calculated and tensorial analysis was performed following the procedure.

The tensorial Hooke's law establishes a general relationship between the strain ε and the stress σ in a solid in the linear elastic regime, through the fourth-order tensor **C** of second-order elastic constants.[68]

$$\sigma_{ij} = \sum_{kl} C_{ijkl}\varepsilon_{kl}$$

where indices *i*, *j*, *k*, *l* run between 1 and 3. Taking advantage of the symmetries of stress and strain matrices and using the Voigt notation, the elasticity tensor (or stiffness tensor) C_{ijkl} can be expressed as a 6 × 6 symmetric matrix of 21 elastic constants $\mathbf{C}_{ij}$, where *i* and *j* now run between 1 and 6 (in Voigt's notation, pair of indices are grouped as follows: 11→1, 22→2, 33→3, 23→4, 13→5, 12→6; this yields a one-index notation for **σ** and **ε**, and a two-indices notation for *C*). The crystal system of the material considered yields additional symmetry constraints, further reducing the number of independent elastic constants. The cubic elasticity matrix has the form

$$C = \begin{matrix} C_{11} & C_{12} & C_{12} & & & \\ C_{12} & C_{11} & C_{12} & & 0 & \\ C_{12} & C_{12} & C_{11} & & & \\ & & & C_{44} & & \\ & 0 & & & C_{44} & \\ & & & & & C_{44} \end{matrix}$$

The calculation of second-order elastic constants of the materials studied were performed with the use of the CRYSTAL09 code.[60] Starting from the optimised geometry of the relaxed crystal, each deformation mode (εi, i= 1…6) is considered in turn. Depending on the system's space group, some deformations may be equivalent and thus fewer than 6 deformation modes must be considered. In the case of the cubic lattices studied here, only three deformations are needed. In particular, in cubic crystals $C_{11} = C_{22} = C_{33}$, $C_{12} = C_{21} = C_{23} = C_{32} = C_{13} = C_{31}$, $C_{44} = C_{55} = C_{66}$ due the fact that x, y, and z axes are identical by symmetry. Also, the off diagonal shear components are zero, i.e. $C_{45} = C_{54} = C_{56} = C_{46} = C_{64} = C_{65} = 0$, and mixed compression/shear coupling does not occur, i.e. $C_{14} = C_{41} = ... = 0$. For each deformation mode *i*, 2*n* strained structures are constructed with small deformations equal to εk = kδεi, with $-n \leqslant k \leqslant n$. δ, the increment of strain used, and *n* are parameters of this procedure. Each of the strained structures is geometry-optimised at fixed unit cell, and the converged crystal is used for an analytical calculation of the energy derivative with respect to unit cell parameters $\left.\frac{\partial E}{\partial \varepsilon_j}\right|_{\varepsilon_k} \forall \boldsymbol{j}$.

This series of derivatives along a single mode of deformation is then fitted as a function of *k*, which amounts to a finite difference calculation of the second derivatives $\frac{\partial^2 E}{\partial \varepsilon_i \partial \varepsilon_j}$. From these, the second-order elastic constants can be calculated by

$$C_{ij} = \frac{1}{V}\left(\frac{\partial^2 E}{\partial \varepsilon_i \partial \varepsilon_j}\right)$$

In this scheme using a mix of analytical derivatives and finite differences, each deformation mode ε_i allows the calculation of one row of the elastic constant matrix C. The size of deformations used (δ) and total number of points sampled for each deformation mode (n) were varied to check the robustness of the method, as well as the fact that the strains imposed were within the limits of the elastic region.

The second-order stiffness tensors obtained are (in units of GPa), for UiO-67:

25.78	13.20	13.20						
13.20	25.78	13.20						
13.20	13.20	25.78						
			9.50					
				9.50				
					9.50			

and for UiO-abdc:

19.94	11.15	10.99						
11.15	24.17	12.58						
10.99	12.58	23.97						
			9.153					
				7.82				
					8.05			

From the second-order elastic constants of each material calculated a full tensorial analysis was performed and key quantities were derived that characterise the mechanical behaviour of the structure in the elastic regime.

The first analysis is to check that the Born elastic stability criterion holds true. This requires that the elastic constant tensor C be positive definite, i.e., that its eigenvalues all be strictly positive.[68] This is the generalization of the well-known stability criteria for cubic crystals

$$C_{44} > 0\,;\; C_{11}-C_{12} > 0\,;\; C_{11} + 2C_{12} > 0$$

the compliance matrix S (and the related fourth-order tensor $\mathbf{S}$) is then calculated, which is the inverse of C (respectively, $\mathbf{C}$). From this, we can calculate the directional Young's modulus for the crystal. Young's modulus $E(\mathbf{u})$, also known as the tensile modulus, is defined as the ratio of the uniaxial stress over the uniaxial strain along unit vector $\mathbf{u}$ (it quantifies the deformation of the material in a direction, when it is compressed in that same direction).

$$E(\boldsymbol{u}) = \frac{1}{u_i\ u_j u_k u_l S_{ijkl}}$$

5.4 Results and discussion

5.4.1 Structure determination of UiO-67 and UiO-abdc.

Room temperature single-crystal X-ray diffraction data were collected on the cubic structures UiO-67 and UiO-abdc, to compare to our high-pressure data which was also collected at room temperature. For UiO-67, some libration was observed on the bpdc ligand, while much larger ellipsoids and more disorder is apparent in the abdc ligand in UiO-abdc (**Figures 5.5** and **5.6**). Phenyl rings in UiO-abdc were modelled over three positions (one ½ occupied, the other ¼ occupied over two positions), while the diazo moiety was modelled over four positions (**Figure 5.6**). Both libration and disorder are unsurprising, as the ligands in both cases are bisected by mirror planes, whilst occupational disorder in abdc is ascribed to the lack of ligand mirror symmetry. Whilst the average structure is cubic and isostructural with UiO-67, the local structure of the abdc ligand must break this symmetry. This type of disorder is common for molecular crystals containing *E*-stillbenes or azobenzenes, the motif creates a pedal wheel motion,[69] and is responsible for interesting properties in molecular crystals such as photochromism seen in salicylideneaniline.[70] Interestingly, the disorder we saw in UiO-abdc did not result in any observable diffuse scattering (**Figure 5.7**), which has been a point of great interest recently.[62, 71]

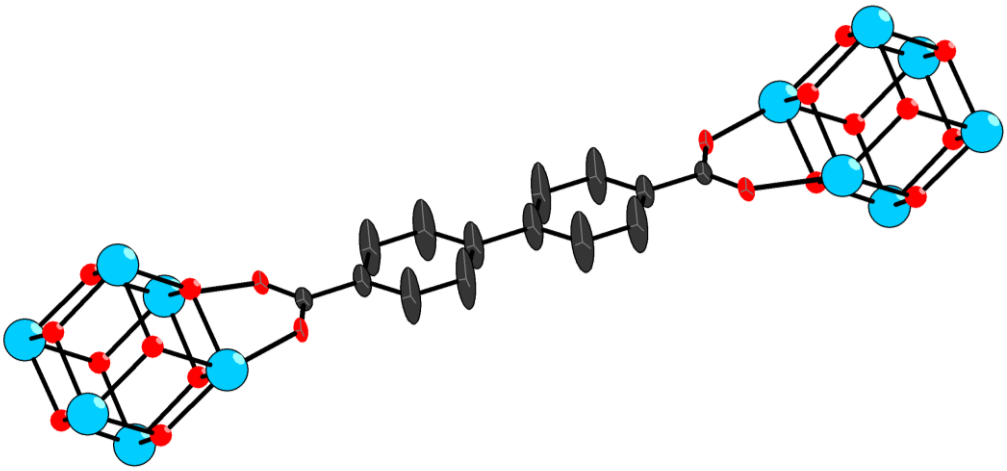

Figure 5.5 View of the BPDC ligand, showing the libration. Ellipsoids shown at 50 % probability for BPDC linker. Colour scheme as before.

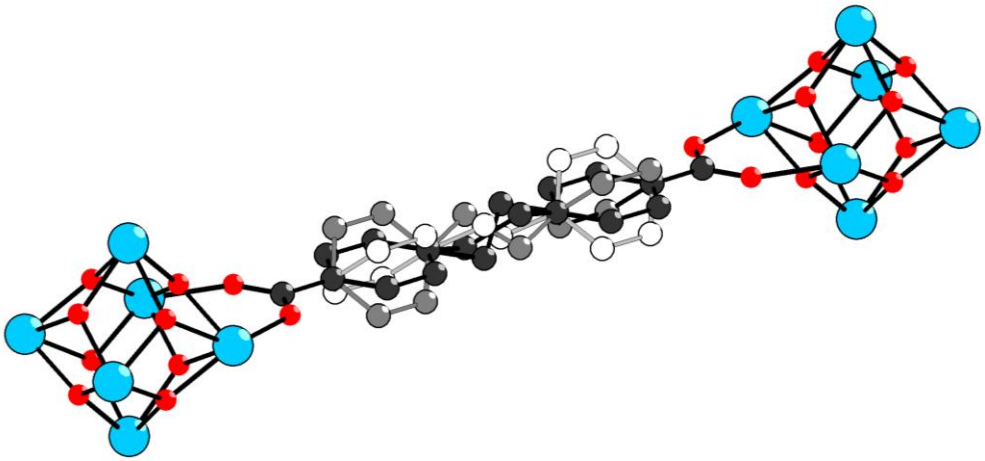

Figure 5.6: View of abdc linker, showing the three orientations of the phenyl ring. Ellipsoids shown at 50 % probability for abdc linker

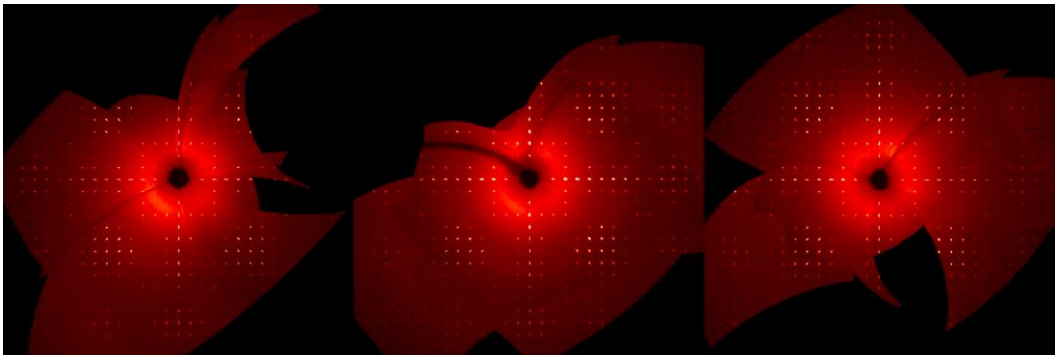

Figure 5.7: Precession images of the 0kl, h0l and hk0 layers of UiO-abdc. Note the lack of diffuse scattering.

5.4.2 Ab initio molecular dynamic simulations

Quantum mechanical simulations were performed on both UiO-67 and UiO-abdc using the crystallographic coordinates as starting models. Motion of the six independent linker arms was followed by MD simulations, which revealed highly dynamic behavior. Atomic probability density functions (PDFs), analogous to thermal ellipsoid models in crystallographic refinements, were derived for the $Zr_6O_4(OH)_4$ core, and each of the six linker units in each case (**Figure 5.8**), this involves mapping the coordinates of each time step of the NVT ensemble onto the equilibrium structure of the NPT ensemble.

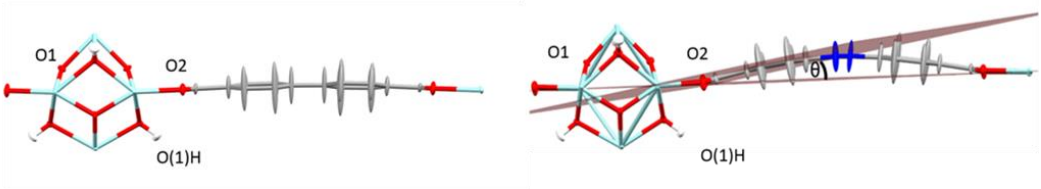

Figure 5.8: Probability density functions of UiO-67 (left) and UiO-abdc (right), where ellipsoids are shown at 50 %. Showing the bisecting planes to create the angle θ.

The resulting PDFs clearly demonstrate the extent of ligand movement observed across the horizontal mirror plane during the simulations. To define the degree of ligand flexibility observed in the molecular dynamics simulations a 'bowing' angle, θ was defined for each ligand (the angle which the benzene carboxylate makes with the Zr_4 metal cluster square plane) and an average magnitude defined for both frameworks was derived for each frame from the trajectories simulated for both UiO-abdc and UiO-67. Plots showing the variation in this parameter for each of the six ligands for both frameworks over the course of the NVT ensemble is shown in **Figure 5.9**. From this it is clear that UiO-abdc supports significantly more ligand flexibility, with half of the ligands flexing above and below the horizontal mirror plane (marked by the $\theta = 0°$ horizontal lines). The absence of such behaviour for the other three ligands is in all probability a sampling issue: If the dynamic trajectory was run for a longer time this behaviour would more than likely be observed for all ligands in UiO-abdc. The mean average value observed for UiO-abdc in this MD trajectory is 5(3)°. For UiO-67 ligand flexing was also observed but to a lesser degree, returning a mean average value of 3(2)°.

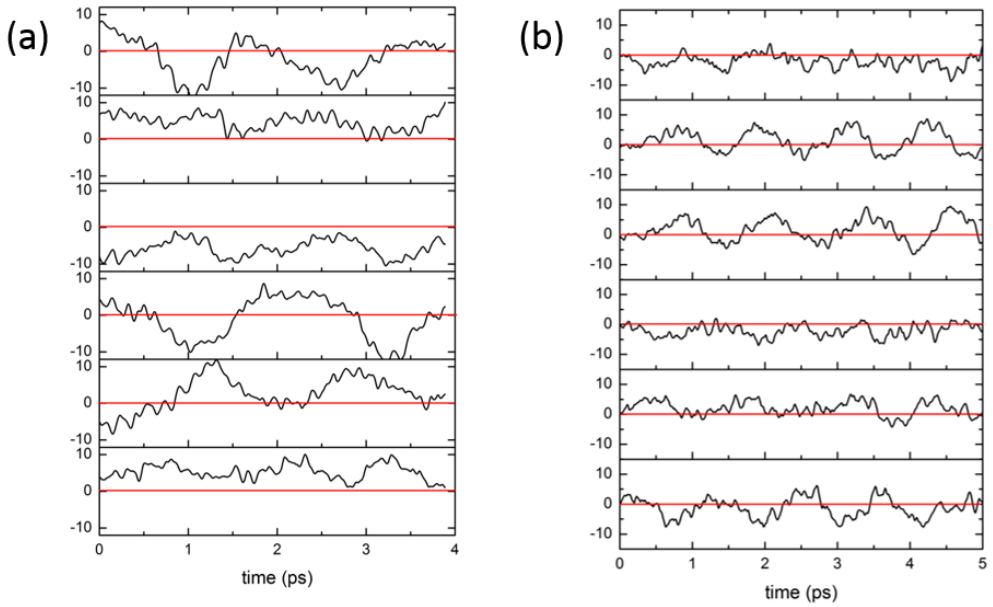

Figure 5.9: Plots showing the variation in θ against time for the six ligands in (a) UiO-abdc, (b) UiO-67.

Good agreement between bond distances in the time averaged MD and crystallographic models of UiO-abdc (**Table 5.4**) were observed. The cage Zr-Zr and Zr-O(2) simulated bond distances were also in excellent agreement (to within 0.05 Å) with work reported by Valenzano *et al.* for the structurally related UiO-66 using EPR spectroscopy and X-ray powder diffraction.[72] The time averaged MD structure returned noticeably different values for the Zr-O(1) cluster distances, depending whether or not the μ^3-O(1) atoms were capped with hydrogen. The simulation suggests that capping the μ^3-O(1) atoms with hydrogen introduces a significant distortion to the ZrO cluster, with the oxygen atoms being pulled out from the cage (**Figure 5.10**). While this finding could not be substantiated by the best-fit space group assigned from the crystallographic data in this work (*Fm*-3*m*, due to the inability to locate the hydroxyl hydrogen atoms, and thus rendering all Zr-O(1) distances equivalent

to one another), it is substantiated by simulation work by Valenzano *et al*, and their equivalent Zr-O(1)H and Zr-O(1) distances agree with ours to within 0.01 Å.

Table 0.1: Selected parameters from the experimentally derived crystal structures of UiO-abdc and UiO-67, at 0 and 1 GPa, compared with the time-averaged structures (at 1GPa) derived from ab initio molecular dynamics.

	UiO-abdc			UiO-67		
Parameters r/Å, ∠/°.	Exp (0 GPa)	Exp (1 GPa)	Time-averaged Calc[c]	Exp (0 GPa)	Exp (1 GPa)	Time-averaged calc
Av. Zr-Zr	3.473(3)	3.504(3)	3.572(6)	3.5056(2)	3.50(6)	3.583(3)
Av. Zr-O1H/	2.119	2.256(2)	2.296(5)	2.1369	2.2307	2.301(2
Zr-O1 (cluster)[a]		2.058(1)	2.092(3)		2.073(12)	2.098(1)
Av.Zr-O2 (ligand)[a]	2.208	2.192(43)	2.248(4)	2.2246	2.192(26)	2.262(3)
Av. O-C	1.268	1.272(3)	1.276(7)	1.2716	1.274(2)	1.280(1)
Av. C-C	1.505	1.4676(8)	1.473(10)	1.4623	1.4700(5)	1.46(4)
						1.489(3)
Av. C_{arom}-C_{arom}	1.388(7)	1.393(11)	1.371(15)	1.3639(17)	1.399(21)	1.36(3)
Av. C-N	1.429	1.3938(9)/	1.413(9)	n/a	n/a	n/a
Av. C-C	n/a	n/a	n/a	1.5116	1.4665(7)	1.487(21)
Av. N-N		1.2926(1)	1.219(16)	-	-	-
θ	0	6.99(2.6)	5(3)	0	0	3(2)

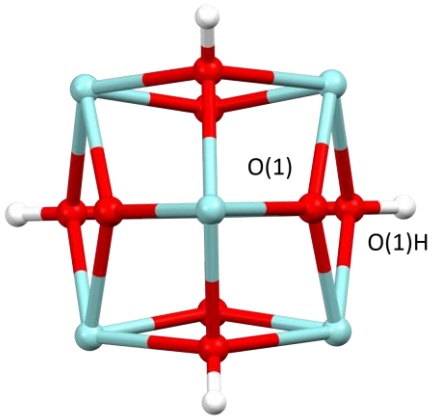

Figure 5.10: Time-averaged mean atomic positions for the $Zr_6O_4(OH)_4$ cluster derived from the MD trajectory highlighting two O(1) environments. Zr-O(1) and Zr-O(1)H distances are ~ 2.10 Å and 2.31 Å, respectively (C- grey, O – red, Zr –light blue, N – dark blue, H - white

The simulated/experimental overlay image of UiO-67 (**Figure 5.11a**) shows close alignment between the MD time-averaged and crystallographic models. In a stark contrast, bowing of the abdc ligand either side of the horizontal mirror plane is clearly observed in UiO-abdc (**Figure 5.11b**).

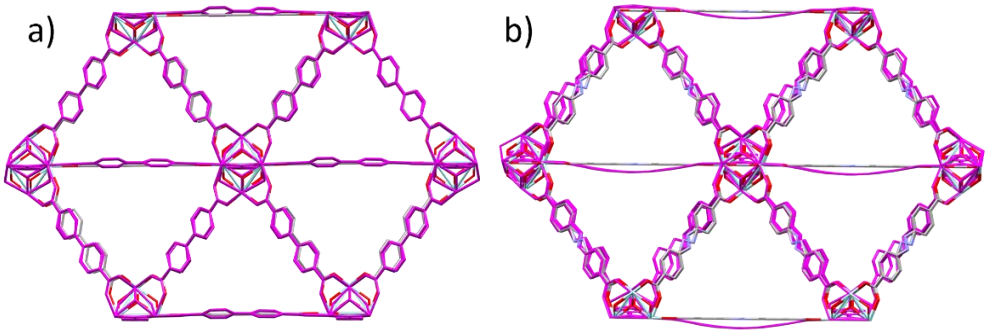

Figure 5.11:(a): Mean atomic positions model for UiO-67 (in magenta) superimposed on the crystallographic structure. (b) Mean atomic positions model for UiO-abdc (in magenta) superimposed on the crystallographically disordered structure

5.4.3 High-pressure crystallography

To investigate the effect of the higher flexibility and geometric frustration of abdc on the mechanical properties of the UiO framework, high-pressure experiments were performed on both UiO-67 and UiO-abdc, by loading suitable single-crystals into modified Merrill–Bassett DACs.[31] In separate experiments, the MOF crystal was then surrounded by either methanol (MeOH) or fluorinert FC-70 as the hydrostatic medium (**Figure 5.12**). Pore volume and content as a function of pressure were calculated using the SQUEEZE algorithm within PLATON **(Table 5.5**). The choice of hydrostatic media (or pressure transmitting media - PTM) is important, as these are microporous materials, if a PTM consisting of small molecules is used, like methanol, it can penetrate inside the crystal and cause transitions from within. Whereas if a PTM made up of bulky molecules, like fluorinert FC-70 – a large perflouroinated oil is used, the molecules are too large to fit into the windows of the framework and when compressed with the crystal, it will cause the crystal to be directly compressed, allowing us to measure the bulk compressibility of the materials.

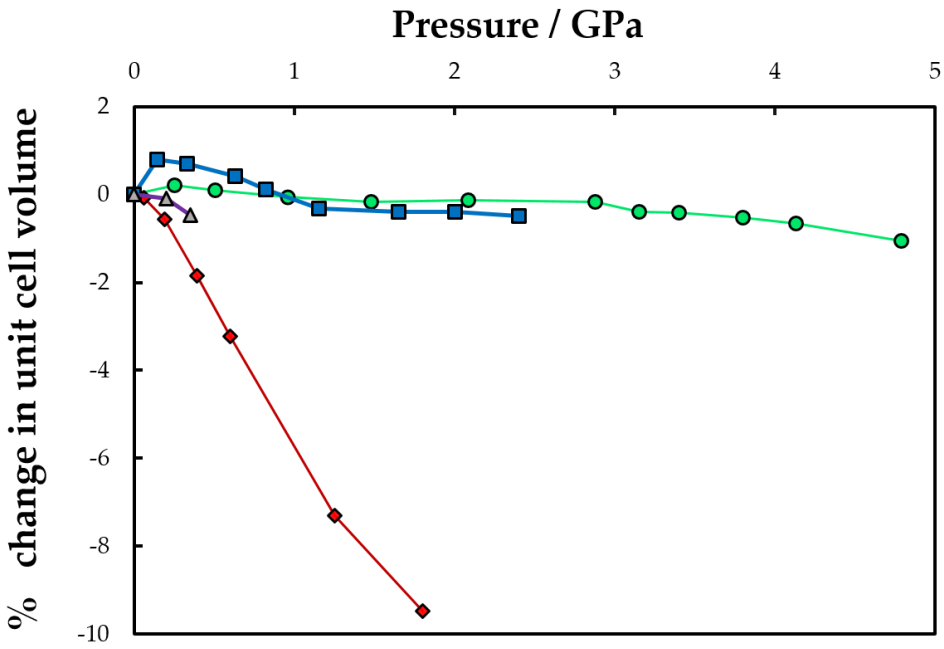

Figure 5.12 Graph of percentage change in volume vs pressure (GPa) for UiO-abdc in methanol (green circles), FC-70 (red diamonds) and UiO-67 in methanol (blue squares), FC-70 (grey triangles).

On increasing pressure using MeOH as a hydrostatic liquid, both UiO-67 and UiO-abdc expand initially at 0.16 and 0.19 GPa respectively (**Figure 5.12**). Such behaviour has been observed in other compression studies of porous MOFs, where MeOH molecules penetrate into the solid and cause the framework to expand.[73] On increasing pressure further, both frameworks begin to compress, before plateauing at 1.15 and 1.20 GPa in UiO-67 and UiO-abdc, respectively. UiO-67 then remains almost incompressible to 2.4 GPa, while UiO-abdc displays similar behavior to 4.8 GPa. The overall change in unit cell volume of the solvated UiO-abdc of less than 1.2% for such a large pressure regime is highly unusual. Experimental bulk moduli were extracted from the experimental cell volume-pressure relationships using EoS Fit (**Figure 5.13**).[74] Bulk moduli over a similar pressure range (~0-2 GPa) of 174 GPa and 580 GPa for UiO-67 and UiO-abdc in MeOH were determined from the experimental

data, although these numbers cannot be compared to existing literature data due to the over-solvated state of both frameworks. Nonetheless, the drastic change that inclusion of MeOH in the framework pores has on the compressibility is evident from these values, with the more porous MOF with the "flexible" abdc ligand being much more resilient to direct compression on inclusion of MeOH to much higher pressures than observed for the more rigid UiO-67.

On initial pressurization using FC-70 (a mixture of large perfluorinated hydrocarbons, usually considered a non-penetrating hydrostatic medium) indirect evidence of guest inclusion can be observed due to an increase in compressibility observed in UiO-67. On increasing pressure, further, direct compression takes place in both frameworks. Unlike with MeOH, further increases in pressure are not accompanied by a plateau in cell volume. In fact, Bragg diffraction is lost from UiO-67 at a relatively modest pressure of 0.3 GPa, yet UiO-abdc undergoes a large change in unit cell volume of almost 10 % to 1.8 GPa, while remaining crystalline. Above 1.8 GPa, the quality of data resolution for UiO-abdc was severely reduced, such that structural responses to increasing pressure could not be determined. The "flexibility" of the ligand in UiO-abdc would, however, appear to impart a greater degree of resistance to increasing pressure, whilst remaining crystalline.

Table 5.5: High pressure crystallographic data of UiO-67 and UiO-abdc in both methanol and FC-70 (including squeeze output where applicable.)

Sample	Pressure/ GPa	Cell Volume/ Å^3	Total Pore Volume/ Å^3	Electron Count/ e$^-$
UiO-67 in methanol	0.14	19511.463	13544	6116
	0.33	19505.404	13522	4640
	0.63	19450.166	13445	4997
	0.82	19391.545	13414	7239
	1.15	19309.584	13336	6986
	1.65	19296.057	13322	7423
	2.00	19293.104	13306	8330
	2.40	19277.396	13289	5914
UiO-67 in FC-70	0.2	19352.877	13444.1	3440
	0.35	19376.658	13375.6	3738
UiO-abdc in methanol	0.19	26302.416		
	0.40	25797.953		
	1.20	25787.715		
	1.75	25826.748		
	2.25	25824.207		
	2.45	25850.371		
	3.15	25773.561		
	3.40	25765.988		
	3.80	25728.357		
	4.80	25658.201		

UiO-abdc in FC-70	0.06	25853.721	19534	10203
	0.19	25727.857	19417	10008
	0.39	25395.09	19159	8818
	0.6	25036.865	n/a	n/a
	1.25	23984.266	n/a	n/a
	1.8	23421.395	n/a	n/a

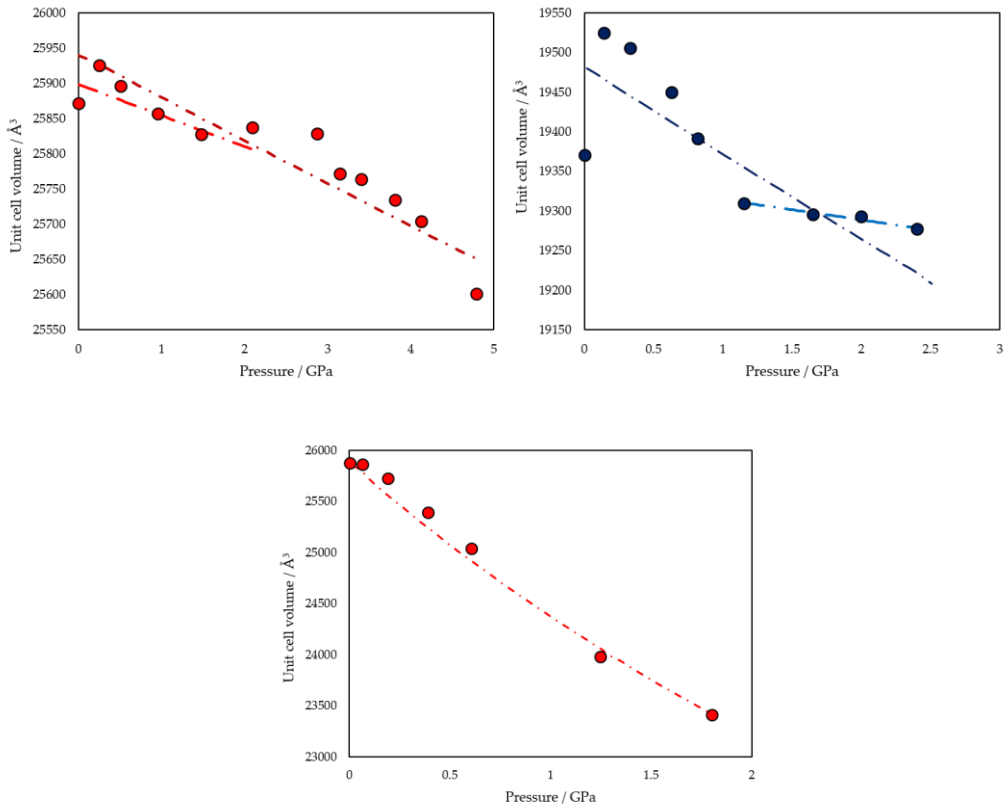

Figure 5.13: (Top left) UiO-abdc in methanol 2nd order B.M fits over pressure range 0 to 2.1 GPa to yield *K* of 580 GPa (light red line), fit of UiO-abdc in methanol over pressure range 0 to 4.8 GPa, to yield *K* of 412 GPa (dark red line). (Top right) Fit of UiO-67 over pressure range 1.15 GPa to 2.4 GPa, to yield K of 749 GPa (dark blue line) Fit of UiO-67 over pressure range 0 GPa to 2.4 GPa, to yield K of 174.67 GPa (light blue line). (Bottom) Fit of UiO-abdc in FC-70 2nd order B.M fits over pressure range 0 GPa to 1.8 GPa to yield K of 14.83 GPa.

5.4.4 DFT-D compression study

In order to determine the compressibility of both frameworks without inclusion of the hydrostatic media, the mean atomic position structures obtained from the MD simulations were geometrically optimised by periodic DFT calculations, and then used as starting models for simulated hydrostatic compression in 0.2 GPa steps up to 1 GPa, thereby simulating direct compression experiments on guest-free frameworks (**Figure 5.14**).

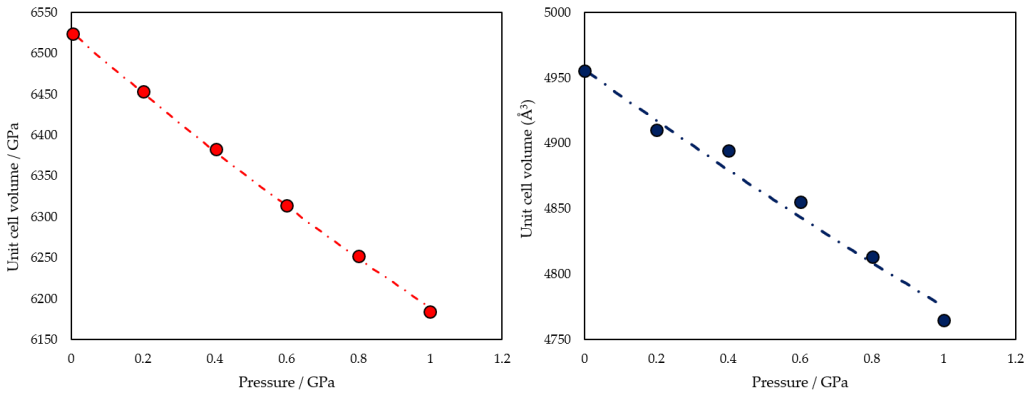

Figure 5.14: Graph of DFT simulated direct compression of UiO-abdc (left) and UiO-67 (right) and their respective 2nd order Birch Murnaghan fits.

Compressions in cell volume of *ca.* 4.0 % and 6.0 % were observed at 1 GPa, respectively for UiO-67 and UiO-abdc. While a 2nd order Birch–Murnaghan equation of state allowed the determination of a bulk modulus of 16.8 GPa for UiO-abdc, a step in the compression curve for UiO-67 in the 0.2–0.4 GPa range prevents us from making a similar calculation. This hint of a structural transition can be linked to the loss of crystallinity observed experimentally in the same pressure range. These results are similar to previous computational work performed on MOF-5, which reported ca. 5% compression to 1 GPa and a *K* of 16.52 GPa.[73] Consistent with the mechanical response of MIL-type

frameworks,[75] the largest structural responses to the external pressure are observed for the ∠C-O-Zr-Zr angle (ϕ) of the carboxylate functional group, which changes by 5° during compression of UiO-abdc (**Figure 5.15**).

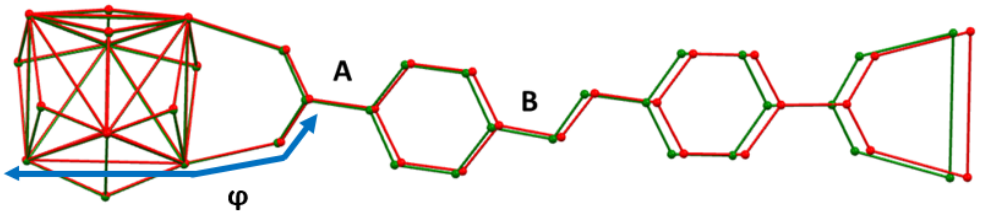

Figure 5.15: Overlay of part of the DFT optimised ambient (red) and 1 GPa (green) structures of UiO-abdc, highlighting the ∠C-O-Zr-Zr angle (ϕ), in addition points A and B which undergo the most compression in the system to allow for such linear compressibility.

Comparing the computational compression with the high-pressure FC-70 compression of UiO-abdc (**Figure 5.16**), we see that the computational models fit the experiment data well. At lower pressures (between 0-0.5 GPa), a slight difference is observed between the DFT study and the experimental compression of UiO-abdc in FC-70, however, we believe that this initial resistance to compression from the experimental FC-70 experiment could be caused by inclusion of FC-70 at low pressures which is then expelled at higher pressures.

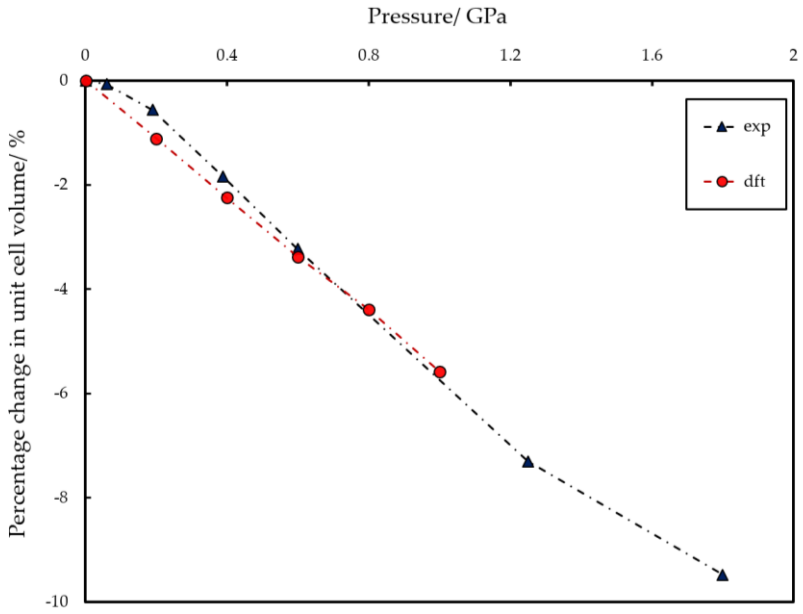

Figure 5.16: Graph of pressure vs change in unit cell volume for UiO-abdc. Red circles: DFT compression study and blue triangles are the experimental values in FC-70.

5.4.5 Elastic compressibility

In order to look at the response of the material under a different mechanical stimulation, we probed evacuated single crystals of UiO-67 and UiO-abdc by nanoindentation, to determine their Young's moduli, *E*, and hardness, *H*. Single crystal X-ray diffraction was performed to establish Miller indices of the crystal facets. Using the load-displacement data gained during the indentation, *E* and *H* as a function of depth. (**Figure 5.17**).

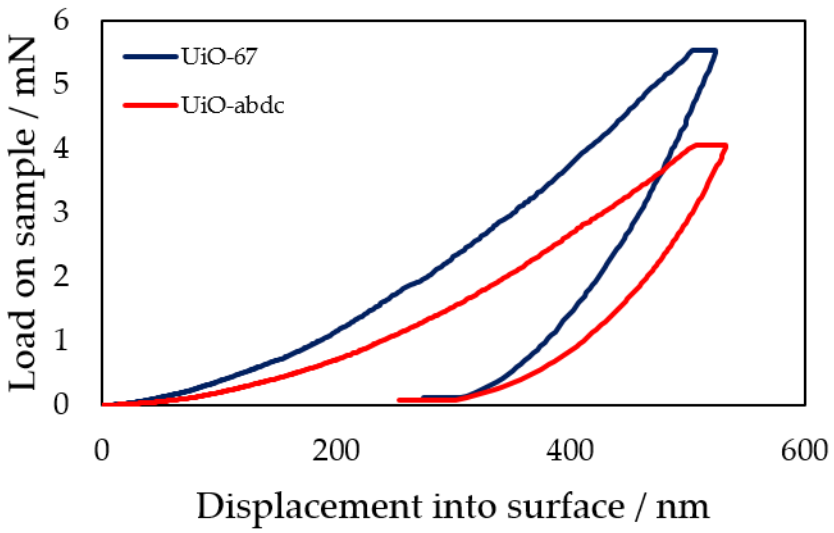

Figure 5.17: Average load-displacement data for UiO-67 (blue) and UiO-abdc (red).

The average values for each sample were calculated as E = 20.02 GPa and H = 1.27 GPa (UiO-67), and E = 13.24 GPa and H = 0.65 GPa (UiO-abdc) (**Figure 5.18**). The trend seen in Young's moduli is in agreement with values derived from DFT calculations of elastic stiffness tensors, with UiO-abdc again softer than UiO-67 under uniaxial compression (24.1 and 21.5 GPa, respectively). Although this good agreement with DFT values is seen for UiO-67, the results agree less well for UiO-abdc. The effect of temperature (simulations at 0 K *cf* experimental at 298 K) was not explored. Despite the higher maximum load which developed upon indentation of UiO-67, the degree of elastic recovery, indicated by the residual depth at P = 0, is broadly similar between the two frameworks. The H values are close to the upper limit for those expected for MOFs.[3]

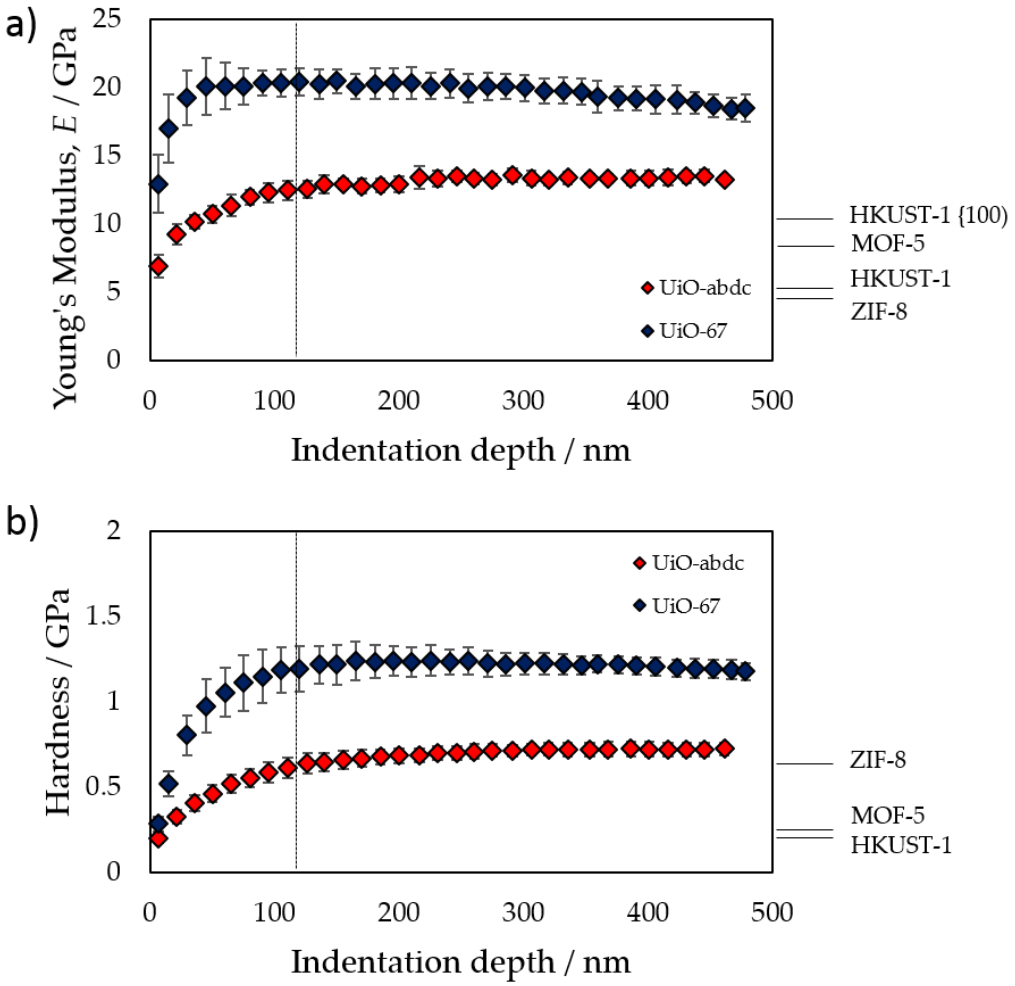

Figure 5.18: Elastic moduli as a function of indentation depth for UiO-67 (blue), and UiO-abdc (red). Indented faces were the [111] in each case. Error bars represent the standard deviation of the multiple measurements performed on crystals of UiO-67, and the 15 indents performed on crystal of UiO-abdc respectively. b) Hardness values as a function of indentation depth with associated errors as above. In each case, literature values for other MOFs of broadly comparable solvent accessible volume are supplied, alongside a large value for a preferentially oriented film of HKUST-1(along the 100 plane).[3-7] Elastic modulus and hardness calculations were performed using data from depths over 100 nm, due to the variance below this level.

The elastic modulus of UiO-67 is amongst the largest reported by nanoindentation for MOFs, and agrees with the low compressibility of the framework. The magnitude of this rigidity is however surprising, given the

empirical inverse relationship observed between *E* and framework solvent accessible volume (SAV). This intuitive relationship has been shown for many MOF systems, where the stiffness of the framework increases considerably as the structure turns dense. UiO-67 has a moderately high SAV(65.9%) for the large *E* value obtained, highlighting how important the choice of linker and metal node are to mechanical properties.[76] In comparison, HKUST-1 [$Cu_3(C_9O_6H_3)_2$], has a similar SAV of 64.3%, yet an elastic modulus of just 9.3 GPa.[7] The framework is also markedly stiffer than the prototypical frameworks ZIF-8 [$Zn(C_3H_3N_2)_2$] (*E* = 3.15 GPa) and MOF-5[$Zn_4O(C_8H_4O_4)_3$] (*E* = 9.5 GPa), having SAVs of 50.3% and 77.7%, respectively (**Figure 5.18**).[3, 5]

The elastic modulus of UiO-abdc is substantially lower than that of UiO-67, which is in agreement with its higher SAV (71.8 %). It is interesting to note that this large decrease in rigidity is accompanied by a relatively small increase in SAV, whereas previous work on a different family of MOFs, IRMOFs, noted that changes in SAV of *ca*. 20 % would be required to elicit decreases in mechanical response of a similar order (*ca*. 40 %).[3] This vastly more flexible nature is consistent with the observation of the frustrated, bowed nature of the abdc ligand in UiO-abdc.

5.5 Conclusions

To summarise, the different mechanical behaviour of two UiO-type frameworks has been fully characterised by computational and experimental methodologies. Bulk and elastic moduli for both UiO-67 and UiO-abdc demonstrate mechanical robustness.[77] The near-zero compressibility of UiO-67 and especially UiO-abdc when over-solvated in MeOH is unique amongst the MOF world, and provides yet another example of the rich physical diversity of these systems, in addition to their much heralded chemical versatility. *E* in each case (20.02 GPa and 13.24 GPa for UiO-67 and UiO-abdc respectively) lies above those of other highly porous MOFs (between 3-10 GPa), and indeed approach the mechanical response expected of 'dense' hybrid frameworks.[6] The large differences in elasticity with relatively small changes in SAV may allow 'fine-tuning' of mechanical response in these highly porous systems, though the effect of defects upon the properties of such materials remains an issue.[62, 63] The unexpected increase in resistance to pressure and the large decrease in the elastic modulus for UiO-abdc compared to UiO-67 are both ascribed to the presence of the azobenzene linker, which bows out of the horizontal plane. Similarly frustrated 'bowed' linkers cause significant disorder in other non-UiO MOF structures,[78, 79] and as such may be a general phenomenon which subsequently impacts on their mechanical behavior. These results are important for those looking to introduce flexibility and/or pressure-coping mechanisms in other hybrid MOF systems.

5.6 References

1. V. Bon, I. Senkovska, I. A. Baburin and S. Kaskel, *Cryst. Growth Des.*, 2013, **13**, 1231-1237.
2. S. J. Garibay and S. M. Cohen, *Chem. Commun.*, 2010, **46**, 7700-7702.
3. J. C. Tan and A. K. Cheetham, *Chem. Soc. Rev.*, 2011, **40**, 1059-1080.
4. B. Van de Voorde, R. Ameloot, I. Stassen, M. Everaert, D. De Vos and J. C. Tan, *J. Mater. Chem. C*, 2013, **1**, 7716-7724.
5. J. Y. Jung, F. Karadas, S. Zulfiqar, E. Deniz, S. Aparicio, M. Atilhan, C. T. Yavuz and S. M. Han, *Phys. Chem. Chem. Phys.*, 2013, **15**, 14319-14327.
6. T. D. Bennett, J. C. Tan, S. A. Moggach, R. Galvelis, C. Mellot-Draznieks, B. A. Reisner, A. Thirumurugan, D. R. Allan and A. K. Cheetham, *Chem. Eur. J.*, 2010, **16**, 10684-10690.
7. S. Bundschuh, O. Kraft, H. K. Arslan, H. Gliemann, P. G. Weidler and C. Woll, *Appl. Phys. Lett.*, 2012, **101**, 101910-101914.
8. H. Wu, T. Yildirim and W. Zhou, *J. Phys. Chem. Lett.*, 2013, **4**, 925-930.
9. J. H. Cavka, S. Jakobsen, U. Olsbye, N. Guillou, C. Lamberti, S. Bordiga and K. P. Lillerud, *J. Am. Chem. Soc.*, 2008, **130**, 13850-13851.
10. A. Schaate, S. Dühnen, G. Platz, S. Lilienthal, A. M. Schneider and P. Behrens, *Eur. J. Inorg. Chem.*, 2012, 790-796.
11. H. Furukawa, K. E. Cordova, M. O'Keeffe and O. M. Yaghi, *Science*, 2013, **341**, 974-986.
12. J. E. Mondloch, M. J. Katz, W. C. Isley, P. Ghosh, P. L. Liao, W. Bury, G. Wagner, M. G. Hall, J. B. DeCoste, G. W. Peterson, R. Q. Snurr, C. J. Cramer, J. T. Hupp and O. K. Farha, *Nat. Mater.*, 2015, **14**, 512-516.
13. M. Bosch, M. Zhang and H.-C. Zhou, *Adv. Chem.*, 2014, **2014**, 1-8.
14. T. D. Bennett and A. K. Cheetham, *Accounts of Chemical Research*, 2014, **47**, 1555-1562.
15. D. Bazer-Bachi, L. Assié, V. Lecocq, B. Harbuzaru and V. Falk, *Powder Technol.*, 2014, **255**, 52-59.
16. G. W. Peterson, J. B. DeCoste, T. G. Glover, Y. G. Huang, H. Jasuja and K. S. Walton, *Microporous Mesoporous Mater.*, 2013, **179**, 48-53.
17. Z. Li and H. C. Zeng, *J. Am. Chem. Soc.*, 2014, **136**, 5631-5639.
18. I. E. Collings, M. G. Tucker, D. A. Keen and A. L. Goodwin, *CrystEngComm*, 2014, **16**, 3498-3506.
19. F. X. Coudert, *Chem. Mater.*, 2015, **27**, 1905-1916.
20. K. J. Gagnon, C. M. Beavers and A. Clearfield, *J. Am. Chem. Soc.*, 2013, **135**, 1252-1255.
21. R. Matsuda, *Nature*, 2014, **509**, 434-435.
22. S. A. Moggach, T. D. Bennett and A. K. Cheetham, *Angew. Chem. Int. Ed.*, 2009, **48**, 7087-7089.

23. L. Sarkisov, R. L. Martin, M. Haranczyk and B. Smit, *J. Am. Chem. Soc.*, 2014, **136**, 2228-2231.

24. A. Schaate, P. Roy, A. Godt, J. Lippke, F. Waltz, M. Wiebcke and P. Behrens, *Chem. Eur. J.*, 2011, **17**, 6643-6651.

25. F. Vermoortele, B. Bueken, G. Le Bars, B. Van de Voorde, M. Vandichel, K. Houthoofd, A. Vimont, M. Daturi, M. Waroquier, V. Van Speybroeck, C. Kirschhock and D. E. De Vos, *J. Am. Chem. Soc.*, 2013, **135**, 11465-11468.

26. A. Schaate, P. Roy, T. Preusse, S. J. Lohmeier, A. Godt and P. Behrens, *Chem. Eur. J.*, 2011, **17**, 9320-9325.

27. R. J. Marshall, S. L. Griffin, C. Wilson and R. S. Forgan, *J. Am. Chem. Soc.*, 2015, **137**, 9527-9530.

28. B. Van de Voorde, I. Stassen, B. Bueken, F. Vermoortele, D. De Vos, R. Ameloot, J. C. Tan and T. D. Bennett, *J. Mater. Chem. A*, 2015, **3**, 1737-1742.

29. A. L. Spek, *J. Appl. Crystallogr.*, 2003, **36**, 7-13.

30. W. C. Oliver and G. M. Pharr, *J. Mater. Res.*, 2004, **19**, 3-20.

31. S. A. Moggach, D. R. Allan, S. Parsons and J. E. Warren, *J. Appl. Crystallogr.*, 2008, **41**, 249-251.

32. G. J. Piermarini, S. Block, J. D. Barnett and R. A. Forman, *J Appl Phys*, 1975, **46**, 2774-2780.

33. Bruker, ed. ECLIPSE, Madison, Wisconsin, USA, 2006.

34. Bruker, ed. SAINT, Madison, Wisconsin, USA, 2007.

35. S. Parsons, in *SHADE*, University of Edinburgh, Edinburgh, Scotland, 2004.

36. G. M. Sheldrick, University of Göttingen, Germany., 2008.

37. Bruker, ed. XPREP, Madison, Wisconsin, USA, 2004.

38. P. W. Betteridge, J. R. Carruthers, R. I. Cooper, K. Prout and D. J. Watkin, *J. Appl. Crystallogr.*, 2003, **36**, 1487-1487.

39. L. Palatinus and G. Chapuis, *J. Appl. Crystallogr.*, 2007, **40**, 786-790.

40. J. VandeVondele, M. Krack, F. Mohamed, M. Parrinello, T. Chassaing and J. Hutter, *Comput. Phys. Commun.*, 2005, **167**, 103-128.

41. A. D. Becke, *Phys. Rev. A*, 1988, **38**, 3098-3100.

42. C. T. Lee, W. T. Yang and R. G. Parr, *Phys. Rev. B*, 1988, **37**, 785-789.

43. S. Grimme, J. Antony, S. Ehrlich and H. Krieg, *J. Chem. Phys.*, 2010, **132**.

44. S. Goedecker, M. Teter and J. Hutter, *Phys. Rev. B*, 1996, **54**, 1703-1710.

45. C. Hartwigsen, S. Goedecker and J. Hutter, *Phys. Rev. B*, 1998, **58**, 3641-3662.

46. M. Krack, *Theor. Chem. Acc.*, 2005, **114**, 145-152.

47. J. VandeVondele and J. Hutter, *J. Chem. Phys.*, 2007, **127**, 114105-114110.

48. L. J. Chen, J. P. S. Mowat, D. Fairen-Jimenez, C. A. Morrison, S. P. Thompson, P. A. Wright and T. Duren, *J. Am. Chem. Soc.*, 2013, **135**, 15763-15773.

49. G. J. Martyna, M. L. Klein and M. Tuckerman, *J. Chem. Phys.*, 1992, **97**, 2635-2643.

50. M. J. McGrath, J. I. Siepmann, I. F. W. Kuo, C. J. Mundy, J. VandeVondele, J. Hutter, F. Mohamed and M. Krack, *ChemPhysChem*, 2005, **6**, 1894-1901.

51. J. Schmidt, J. VandeVondele, I. F. W. Kuo, D. Sebastiani, J. I. Siepmann, J. Hutter and C. J. Mundy, *J. Phys. Chem. B*, 2009, **113**, 11959-11964.

52. A. M. Reilly, D. A. Wann, C. A. Morrison and D. W. H. Rankin, *Chem. Phys. Lett.*, 2007, **448**, 61-64.

53. A. M. Reilly, S. Habershon, C. A. Morrison and D. W. H. Rankin, *J. Chem. Phys.*, 2010, **132**, 134511-134521.

54. A. M. Reilly, S. Habershon, C. A. Morrison and D. W. H. Rankin, *J. Chem. Phys.*, 2010, **132**, 094502-094512.

55. I. J. Bruno, J. C. Cole, P. R. Edgington, M. Kessler, C. F. Macrae, P. McCabe, J. Pearson and R. Taylor, *Acta Crystallogr. Sect. B-Struct. Sci.*, 2002, **58**, 389-397.

56. S. J. Clark, M. D. Segall, C. J. Pickard, P. J. Hasnip, M. I. J. Probert, K. Refson and M. C. Payne, *Z. Kristallogr.*, 2005, **220**, 567-570.

57. J. P. Perdew, K. Burke and M. Ernzerhof, *Phys Rev Lett*, 1996, **77**, 3865-3868.

58. A. Tkatchenko and M. Scheffler, *Phys. Rev. Lett.*, 2009, **102**, 073005.

59. D. F. Shanno, *Math. Comput.*, 1970, **24**, 647.

60. R. Dovesi, R. Orlando, B. Civalleri, C. Roetti, V. R. Saunders and C. M. Zicovich-Wilson, *Z. Kristallogr.*, 2005, **220**, 571-573.

61. J. P. Perdew, A. Ruzsinszky, G. I. Csonka, O. A. Vydrov, G. E. Scuseria, L. A. Constantin, X. L. Zhou and K. Burke, *Phys. Rev. Lett.*, 2008, **100**.

62. M. J. Cliffe, W. Wan, X. D. Zou, P. A. Chater, A. K. Kleppe, M. G. Tucker, H. Wilhelm, N. P. Funnell, F. X. Coudert and A. L. Goodwin, *Nat. Commun.*, 2014, **5**.

63. M. J. Cliffe, J. A. Hill, C. A. Murray, F. X. Coudert and A. L. Goodwin, *Phys. Chem. Chem. Phys.*, 2015, **17**, 11586-11592.

64. D. W. Lewis, A. R. Ruiz-Salvador, A. Gomez, L. M. Rodriguez-Albelo, F. X. Coudert, B. Slater, A. K. Cheetham and C. Mellot-Draznieks, *CrystEngComm*, 2009, **11**, 2272-2276.

65. A. M. Walker, B. Civalleri, B. Slater, C. Mellot-Draznieks, F. Cora, C. M. Zicovich-Wilson, G. Roman-Perez, J. M. Soler and J. D. Gale, *Angew. Chem. Int. Ed.*, 2010, **49**, 7501-7503.

66. W. F. Perger, J. Criswell, B. Civalleri and R. Dovesi, *Comput. Phys. Commun.*, 2009, **180**, 1753-1759.

67. J. C. Tan, B. Civalleri, C. C. Lin, L. Valenzano, R. Galvelis, P. F. Chen, T. D. Bennett, C. Mellot-Draznieks, C. M. Zicovich-Wilson and A. K. Cheetham, *Phys. Rev. Lett.*, 2012, **108**.

68. J. F. Nye, *Physical Properties of Crystals—Their Representation by Tensors and Matrices*, Clarendon, 1985.

69. J. Harada and K. Ogawa, *J. Am. Chem. Soc.*, 2001, **123**, 10884-10888.

70. J. Harada, H. Uekusa and Y. Ohashi, *J. Am. Chem. Soc.*, 1999, **121**, 5809-5810.

71. C. A. Trickett, K. J. Gagnon, S. Lee, F. Gándara, H.-B. Bürgi and O. M. Yaghi, *Angew. Chem. Int. Ed.*, 2015, **54**, 11162-11167.

72. L. Valenzano, B. Civalleri, S. Chavan, S. Bordiga, M. H. Nilsen, S. Jakobsen, K. P. Lillerud and C. Lamberti, *Chem. Mater.*, 2011, **23**, 1700-1718.

73. A. J. Graham, D. R. Allan, A. Muszkiewicz, C. A. Morrison and S. A. Moggach, *Angew. Chem. Int. Ed.*, 2011, **50**, 11138-11141.

74. R. A. Angel, J. Gonzalez-Platas and M. Alvaro, *Z. Kristallogr.*, 2014, **229**, 405-419.

75. C. Serre, S. Bourrelly, A. Vimont, N. A. Ramsahye, G. Maurin, P. L. Llewellyn, M. Daturi, Y. Filinchuk, O. Leynaud, P. Barnes and G. Ferey, *Adv. Mater.*, 2007, **19**, 2246-+.

76. M. W. Zhang, Y. P. Chen, M. Bosch, T. Gentle, K. C. Wang, D. W. Feng, Z. Y. U. Wang and H. C. Zhou, *Angew. Chem. Int. Ed.*, 2014, **53**, 815-818.

77. J. C. Tan, T. D. Bennett and A. K. Cheetham, *Proc. Natl. Acad. Sci. U.S.A.*, 2010, **107**, 9938-9943.

78. V. Bon, I. Senkovska, M. S. Weiss and S. Kaskel, *CrystEngComm*, 2013, **15**, 9572-9577.

79. H. Furukawa, Y. B. Go, N. Ko, Y. K. Park, F. J. Uribe-Romo, J. Kim, M. O'Keeffe and O. M. Yaghi, *Inorg. Chem.*, 2011, **50**, 9147-9152.

-Chapter Six-

The Effect of Ligand Length on Mechanical Properties of Zr-MOFs

6.1 Synopsis

This experimental chapter builds on the foundations of Chapter Five, investigating the series of Zr-containing MOFs with a view towards understanding how physical and mechanical properties are influenced by the choice of ligand. The ligands discussed in this chapter are 4,4′-stillbene dicarboxylate, 4,4′-ethynylenedibenzoate and 4,4′-(buta-1,3-diyne-1,4-diyl)dibenzoate (herein referred to as sdc, edb and bddb, respectively), which when combined with $Zr_6O_4(OH)_4$ clusters form the frameworks $[Zr_6O_4(OH)_4(sdc)_6]$, $[Zr_6O_4(OH)_4(edb)_6]$ and $[Zr_6O_4(OH)_4(bddb)_6]$, respectively. These frameworks were studied using a combined experimental and computational approach using single-crystal X-ray diffraction, single-crystal nanoindentation, *ab initio* molecular dynamics and density functional theory.

6.2 Introduction

The ligands 4,4′-stillbene dicarboxylate, 4,4′-ethynylenedibenzoate and 4,4′-(buta-1,3-diyne-1,4-diyl)dibenzoate, herein referred to sdc, edb and bddb, respectively were the dicarboxylate ligands chosen to extend the library of Zr – MOFs (**Figure 6.1**). The shortest ligand, sdc, is the carbon analogue of abdc (studied in **Chapter 5**), and is congruently a non-linear ligand. The two other ligands, edb and bddb, are linear, containing alkyne and butadiyne units respectively. All of these frameworks have been shown to be stereoselective bromination materials, due to the unsaturated C-C bonds present within the linker.[1, 2] This provides an attractive route to the synthesis of bromoalkanes. The stability of these frameworks were tested through the bromination reactions, as there was an inherent change in hybridisation and geometry of fundamental linker atoms upon addition of Br_2. In the case of UiO-sdc and UiO-edb, the frameworks were mechanically stable to the addition and

allowed the bromination to be characterised in a single-crystal to single-crystal (SCSC) manner. However, in the case of UiO-bddb, the resulting brominated sample had turned from a single-crystal to powder, and was characterised by XRPD and NMR.[1]

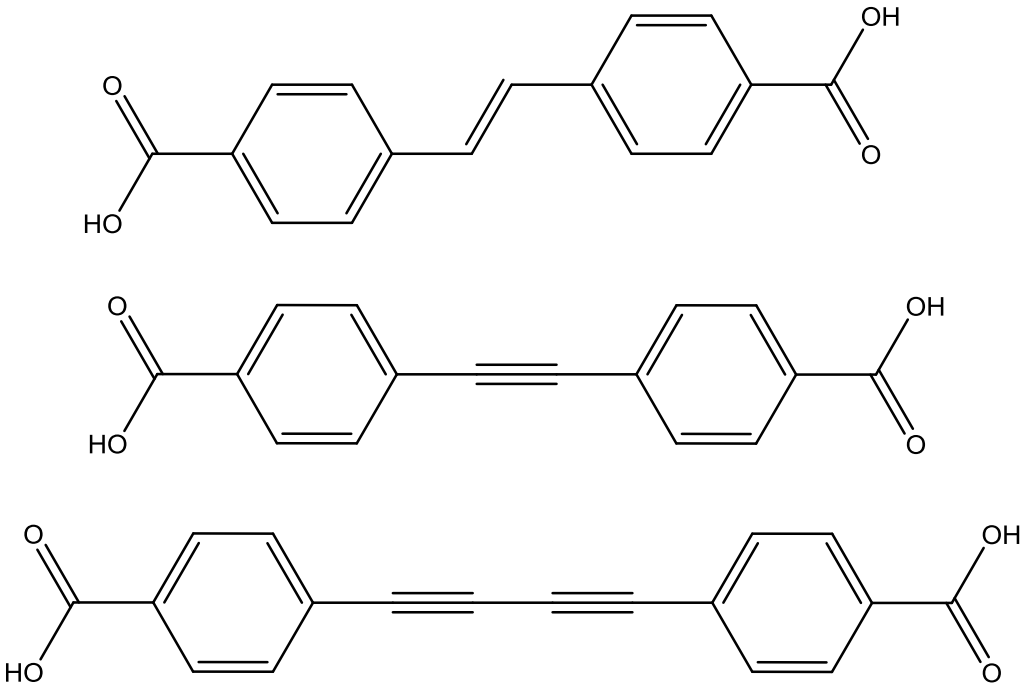

Figure 6.1: Chemical drawings of the three ligands that are investigated in this chapter. From top to bottom: 4,4′-stillbene dicarboxylate(sdc), 4,4′-ethynylenedibenzoate (edb) and 4,4′-(buta-1,3-diyne-1,4-diyl)dibenzoate (bddb).

This difference in behaviour between the frameworks is further investigated in this chapter. The elastic and bulk compressibility are determined by single-crystal nano-indentation, and *ab initio* molecular dynamics and DFT, respectively. High-pressure X-ray diffraction experiments were attempted on these materials to complement the theoretical work, however, the data were not of high enough quality, and were therefore omitted from this chapter.

6.3 Experimental

6.3.1 Synthesis

Note: the synthesis of materials was carried out by Mr Ross Marshall and Dr Ross Forgan of the University of Glasgow.

UiO-sdc: L-proline (0.104 g, 0.90 mmol, 4 eq.), 4,4′-stilbenedicarboxylic acid (0.060 g, 0.23 mmol, 1 eq) and zirconium tetrachloride (0.052 g, 0.23 mmol, 1 eq.) were added to a 50 mL PYREX reagent bottle. To the bottle 10 mL DMF was added, the mixture was sonicated and following addition of hydrochloric acid (0.02 mL) the bottle was sealed. The reaction vessel was then subject to sonication to aid homogeneous distribution of the reagents, followed by heating at 100 °C for 48 hours in the oven. The bottle was removed from the oven after this period, and allowed to cool to room temperature. The crystals were left to stand in their mother solution.

UiO-edb: L-proline (0.104 g, 0.90 mmol, 4 eq), 4,4′-ethynylenedibenzoic acid (0.060 g, 0.23 mmol, 1 eq.) and zirconium tetrachloride (0.052 g, 0.23 mmol, 1 eq.) were added to a 50 mL PYREX reagent bottle with screw cap. To the bottle 10 mL DMF was added, the mixture was sonicated and, following addition of hydrochloric acid (0.02 mL), the bottle was sealed. The reaction vessel was then subject to sonication to aid homogenous distribution of the reagents, followed by heating at 100 °C for 48 hours in the oven. The bottle was removed from the oven after this period, and allowed to cool to room temperature.

UiO-bddb: Benzoic acid (0.824 g, 6.75 mmol, 30 eq), zirconium tetrachloride (0.052 g, 0.22 mmol, 1 eq.) and 13 mL DMF were added to a 50 mL PYREX reagent bottle and sonicated. 4,4′-(buta-1,3-diyne-1,4-diyl)dibenzoic acid (0.065 g, 0.22 mmol, 1 eq.) and concentrated HCl (0.02 ml) were added and the suspension was sonicated, followed by heating at 120 °C for 24 hours in the oven. The bottle was removed from the oven after this period, and allowed to cool to room temperature. The crystals were left to stand in their mother solution.

6.3.2 Nanoindentation

Note: the nanoindentation experiments were carried out by Dr Tom Bennett at the University of Cambridge.

Nanoindentation experiments were performed using an MTS Nanoindenter XP, located in an isolation cabinet to shield against thermal fluctuations and acoustic interference. Samples were first mounted using an epoxy resin, which was then ground away using a silicon carbide disc, before being polished using increasingly fine diamond suspensions. Indentations were conducted under the dynamic displacement-controlled "continuous stiffness measurement" mode. *E* (Young's modulus) and *H* (hardness) were subsequently determined as a function of the surface penetration depth. A 2-nm sinusoidal displacement at 45 Hz was superimposed onto the system's primary loading signal, and the loading and unloading strain rates were set at 5×10^{-2} s^{-1}. All tests were performed to a maximum indentation depth of 500 nm (unless otherwise stated) using a Berkovich (i.e., three-sided pyramidal) diamond tip of radius ~ 100nm. The raw data (load-displacement curves) obtained were analysed using the Oliver and Pharr method.[3]

Face-indexing measurements used to determine the crystal faces being indented were performed at room temperature, using an Oxford diffraction SuperNova X-ray diffractometer with Cu K_α radiation (=1.540598 Å) with an Atlas CCD detector. Data were collected in ω-scans in four settings of 2θ and ϕ with a step size of 1°. Exposure times for UiO-sdc, Uio-edb and UiO-bddb were 20 s, 40 s and 60 s at low angle and 40 s, 60 s and 60 s at high angle, respectively. Data processing, unit cell determination and face indexing were carried out using the program CrysAlisPro. **Table 6.1-6.3** and **Figure 6.2-6.4** contain the main crystallographic parameters and different views of the indexed crystals.

Table 6.1: Summary of face indexing statistics for UiO-sdc

UiO-sdc		
Crystal system	Cubic	
Space group	*Fm*-3*m*	
Unit cell dimensions	a = 29.8884(3)	α= 90
(Å, °)	b = 29.8884(3)	β = 90
	c = 29.8884 (3)	γ = 90
Volume (Å^3)	26699.8(3)	
Crystal size (mm)	0.047 x 0.062 x 0.073	
Main crystal faces	(1 1 1), (-1 1 1)	
	(1 -1 1), (1 1 -1)	
	(1 -1 -1), (-1 1 -1)	
	(-1 -1 1) ,(-1 -1 -1)	

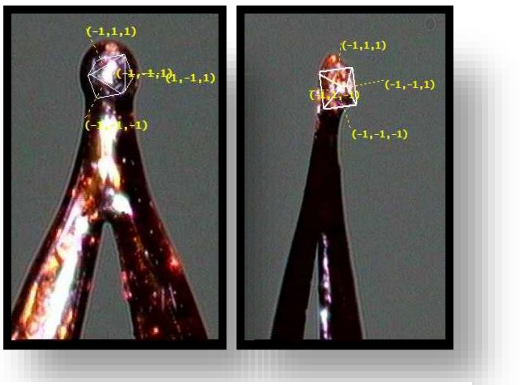

Figure 6.2: Face-normals of principal faces of the crystal, note the triangular shaped faces (1 1 1), (-1 1 1), (1 -1 1), (1 1 -1), (1 -1 -1), (-1 1 -1), (-1 -1 1) and (-1 -1 -1).

Table 6.2: Summary of face indexing statistics for UiO-edb

UiO-edb		
Crystal system	Cubic	
Space group	*Fm*-3*m*	
Unit cell dimensions	*a* = 30.4107(2)	$\alpha = 90$
(Å, °)	*b* = 30.4107(2)	$\beta = 90$
	c = 30.4107(2)	$\gamma = 90$
Volume (Å^3)	28124.1(2)	
Crystal size (mm)	0.049 x 0.1 x 0.125	
Main crystal faces	(1 1 1), (-1 1 1), (1 -1 1), (1 1 -1), (1 -1 -1), (-1 1 -1), (-1 -1 1) (-1 -1 -1)	

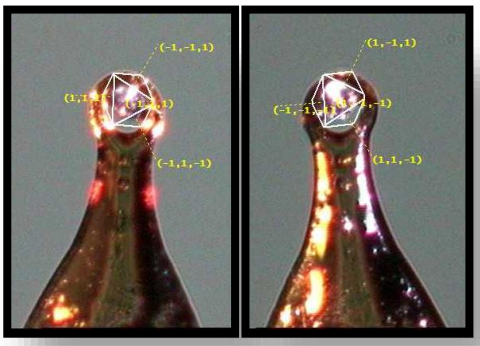

Figure 6.3: Face-normals of principal faces of the crystal, note the triangular shaped faces (1 1 1), (-1 1 1), (1 -1 1), (1 1 -1), (1 -1 -1), (-1 1 -1), (-1 -1 1) and (-1 -1 -1)

Table 6.3: Summary of face indexing statistics for UiO-bddb

UiO-bddb		
Crystal system	Cubic	
Space group	*Fm*-3*m*	
Unit cell dimensions	*a* = 34.0163(2)	$\alpha = 90$
(Å, °)	*b* = 34.0163(2)	$\beta = 90$
	c = 34.0163(2)	$\gamma = 90$
Volume (Å^3)	39360.7(2)	
Crystal size (mm)	0.119 x 0.158 x 0.188	
Main crystal faces	(1 1 1), (-1 1 1), (1 -1 1), (1 1 -1), (1 -1 -1), (-1 1 -1), (-1 -1 1) (-1 -1 -1)	

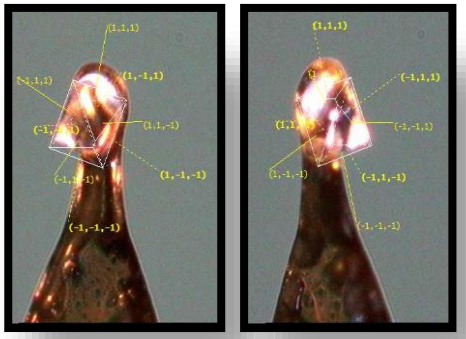

Figure 6.4: Face-normals of principal faces of the crystal, note the triangular shaped faces (1 1 1), (-1 1 1), (1 -1 1), (1 1 -1), (1 -1 -1), (-1 1 -1), (-1 -1 1) and (-1 -1 -1)

6.3.3 Ab initio molecular dynamics

All *ab initio* (Born-Oppenheimer) MD calculations were performed using the Quickstep module of the CP2K (version 2.6) simulation package.[4] The simulation set-up was carried out in a similar manner to those calculations carried out in Chapter 5. The BLYP[5, 6] exchange-correlation functional with semi-empirical dispersion corrections to the energies and gradients from the DFT-D3[7] method (cut-off radius 10 Å) where used throughout. Energies and forces were calculated utilizing the Gaussian plane-wave scheme, which is a dual basis set method wherein a linear combination of Gaussian-type orbitals is used to describe the Kohn-Sham molecular orbitals while the electron density is described by an auxiliary plane-wave basis set (expressed at an energy cut-off of 350 Ry, accompanied by the relative cut-off of 50 Ry for the Gaussian basis set collocation). The double-zeta quality MOLOPT basis set[8-11] was used for all elements, in conjunction with the relativistic, norm-conserving Goedecker-Teter-Hutter pseudopotentials, optimised for use against the BLYP functional. During each SCF cycle, the electronic structure was explicitly minimised to a tolerance of 10^{-7} Hartree. The equations of motion were integrated using a time step of 0.55 fs.

The crystallographic models of UiO-sdc, UiO-edb and UiO-bddb were transformed to their primitive cell settings, thereby reducing the volume of the crystallographic unit cells to a quarter of their conventional setting, and presenting a considerable cost-saving for the modelling work. However, this still resulted in relatively large unit cell models, especially for UiO-bddb ($a = b = c = ca.$ 24 Å, $\alpha = \beta = \gamma = 60°$), which by definition results in compact 1st Brillouin zones. Thus, the constraint that the QUICKSTEP module employs Γ-point sampling only of the Brillouin zone was not a concern in this work. An initial

geometry optimisation was carried out on the three frameworks, to allow for bond lengths, in particular C-H and O-H bond lengths, to increase from their crystallographically determined distances. For the crystallographically disordered UiO-sdc, equilibration of the model was initiated under the isobaric-isothermal ensemble regime (NPT; constant number of particles, pressure and temperature) for 6 ps. The temperature was set to 300 K and controlled by a chain of Nosé-Hoover thermostats[12] coupled to every degree of freedom (the so-called massive thermostat) with a frequency of 4000 cm^{-1}, which is high enough to properly sample the fast vibrational motion of the O-H bond in the ZrO cluster of the UiO-67-based MOFs. The barostat was set up with a coupling time constant of 300 fs and an external pressure of 1 bar. In addition, a reference unit cell of constant volume was defined alongside the model of UiO-sdc to fix the number of grid points used to compute the Coulomb and exchange-correlation energies. This was used to mitigate any effects of varying grid points due to potential volume fluctuations of the simulation box (due to large breathing motions of UiO-sdc). It has been shown previously that the use of such a reference cell avoids any discontinuities in the potential energy profile when the volume is permitted to vary.[13-15] The unit cell parameters were then fixed at the equilibrated values, and the ensemble switched to NVT for production run dynamics (3 ps). For UiO-edb, with rigid linker geometry but longer ligand than sdc, an equilibration run of 2.5 ps in the NPT ensemble was followed by production run of 7 ps performed in the NVT ensemble. In constrast, UiO-bddb, with an even longer ligand, was equilibrated in the NPT ensemble for 1 ps, and then the production run dynamics were ran for 6.5 ps in the NVT ensemble. Both were performed with the same settings as listed above for UiO-sdc. The resulting trajectories were then analysed numerically to determine the time-averaged mean atomic

positions (which are simply the coordinates for each atom averaged over all frames from the production run data set), and to calculate the atomic probability density functions (via numerical calculation of the variances and co-variances of each atom, using methods described previously).[16-18] The latter are analogous to the thermal ellipsoid model used in crystallographic refinements, and are displayed in in the main text at the standard 50% probability level. The output data were then processed graphically using Mercury CSD 3.3.1.[19] The time-average atomic positions were suitable models to use as starting points for the geometry optimization calculations reported in the following section.

6.3.4 DFT-D isotropic compression study

All calculations were performed using the CASTEP (version 5.11) simulation package.[20] The Hamiltonian operator was approximated using the Perdew-Burke-Ernzerhof (PBE) exchange-correlation functional, with the molecular wavefunction description provided by 'on-the-fly' pseudopotentials and a plane wave basis set operating at 650 eV, which gave convergence to within 4 meV per atom. In addition, the Tkatchenko-Scheffler dispersion correction was applied.[21, 22] The electronic structure was sampled at the gamma position only in the Brillouin zone due to the large size of the primitive unit cell (resulting in a k-point sampling grid of no greater than 0.06 $Å^{-1}$). The geometry optimisation calculations, which took the time-averaged mean atomic position models derived from the *ab initio* MD production trajectories as input, were run without any symmetry constraints, thus allowing for an independent variation of both the atomic positions and the primitive cell parameters. The potential energy surface was searched for energy minima by means of the Broyden-Fletcher-Goldfarb-Shanno (BFGS) algorithm.[23] Structures were

considered to be optimised when the energy per atom, maximum force, maximum stress, and maximum atomic displacement converged to the values of 0.02 meV $atom^{-1}$, 0.05 eV $Å^{-1}$, 0.1 GPa, and 0.002 Å, respectively. Once the first, ambient pressure, model was optimised, an external hydrostatic pressure of 0.2 GPa was applied and the system re-optimised; this process was repeated at 0.2 GPa steps until structure optimisation was no longer possible. This is usually due to the system reaching the limit of sensible bonding. These hydrostatic pressures reached were 0.60 GPa, 0.80 and 0.20 GPa for UiO-sdc, UiO-edb and UiO-bddb respectively.

6.4 Results and discussion

6.4.1 Structure determination of UiO-sdc, UiO-edb and UiO-bddb.

Room temperature single-crystal X-ray diffraction data were collected for UiO-sdc, UiO-edb and UiO-bddb and their structures were determined. UiO-sdc is the carbon analogue of UiO-abdc (Chapter 5), and as such similar occupational disorder and libration of the ligand as observed for that system was also observed here. The unit cell of UiO-sdc is slightly larger than observed for UiO-abdc, (a=b=c= 29.8884(3) Å, α=β=γ= 90° compared to a=b=c= 29.3248(8) Å, α=β=γ= 90°), which can be attributed to the difference in length of the carbon-carbon bond distance in UiO-sdc compared to the smaller nitrogen-nitrogen bond distance in UiO-abdc. The phenyl rings of UiO-sdc were modelled over three positions (one ½ occupied, the other ¼ occupied over two positions), while the carbon-carbon double bond was modelled over four positions (**Figure 6.5 and 6.6**). Both libration and disorder are unsurprising as the ligand is bisected by mirror planes, whilst the occupational disorder in sdc is ascribed to the lack of mirror symmetry in the ligand. Both ligands in UiO-edb (**Figure 6.7 and 6.8**) and UiO-bddb (**Figure 6.9** and **6.10**) possess mirror symmetry, however libration perpendicular to the mirror plane was observed. In both cases this libration increased in moving further from the $Zr_6O_4(OH)_4$ core. The bddb ligand is longer than the edb ligand by 2 Å, due to an additional alkyne group, this is reflected in the difference in cell parameters (UiO-edb = a=b=c= 30.41070(13), α=β=γ= 90° and UiO-bddb = a=b=c= 34.01634(13), α=β=γ= 90°), and therefore libration was observed to be even more accentuated in the case of UiO-bddb, in comparison to that observed in UiO-edb.

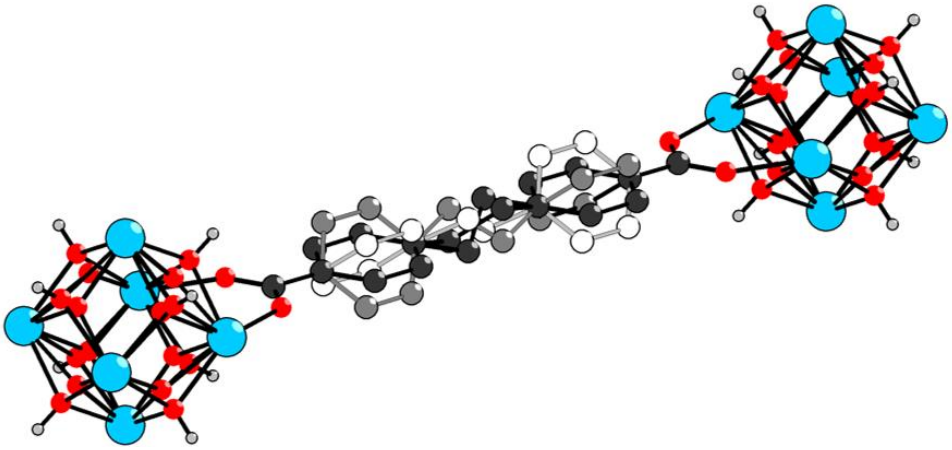

Figure 6.5: Main connectivity of UiO-sdc as determined by X-ray crystallography, showing both the hydroxide/oxide disorder on the $Zr_6O_4(OH)_4$ cores and the sdc linker. The disordered components of the linker are highlighted in black (50 % occupied), grey and white (each 25 % occupied). Zr – atoms - blue, H-atoms – white, O-atoms- red. H-atoms omitted from linker for clarity.

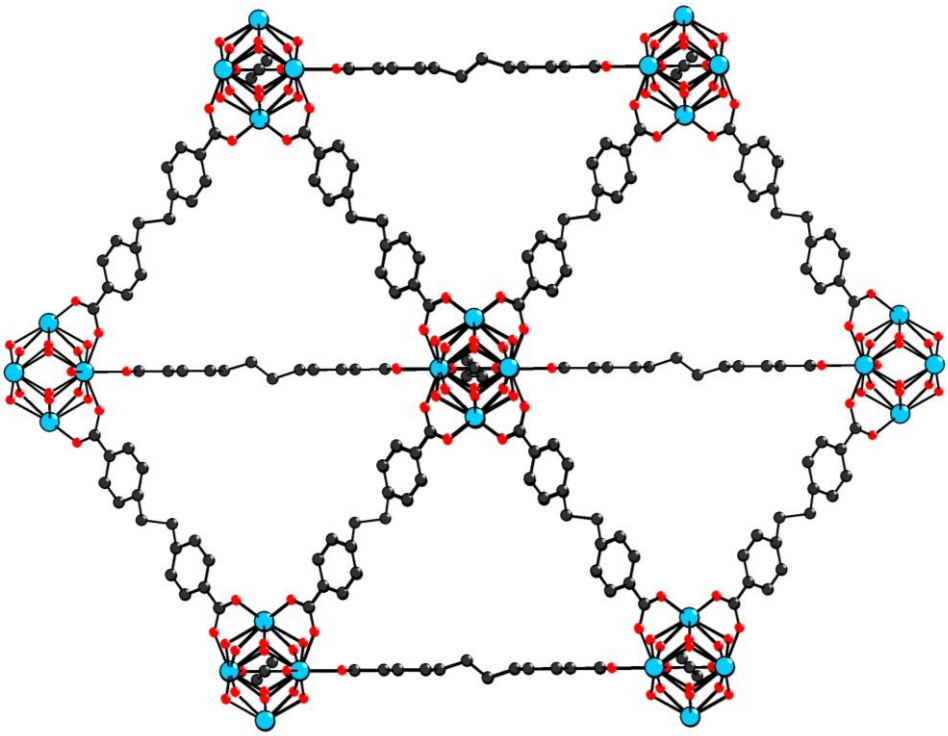

Figure 6.6: Unit cell of UiO-sdc as determined by X-ray crystallography viewed down the *a*-axis. Disorder and H-atoms have been removed for clarity. Colour scheme as above.

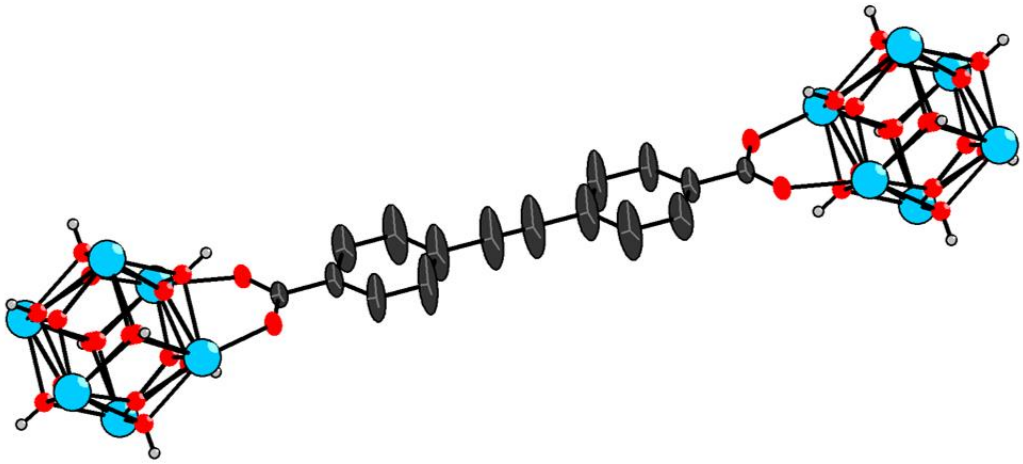

Figure 6.7: Main connectivity of UiO-edb as determined by X-ray crystallography, showing the hydroxide/oxide disorder on the $Zr_6O_4(OH)_4$ cores and the libration of the edb linker. Anisotropic displacement parameters shown at 50 % probability. Note the increasing thermal motion on edb on moving away from metal core. Colour scheme as above.

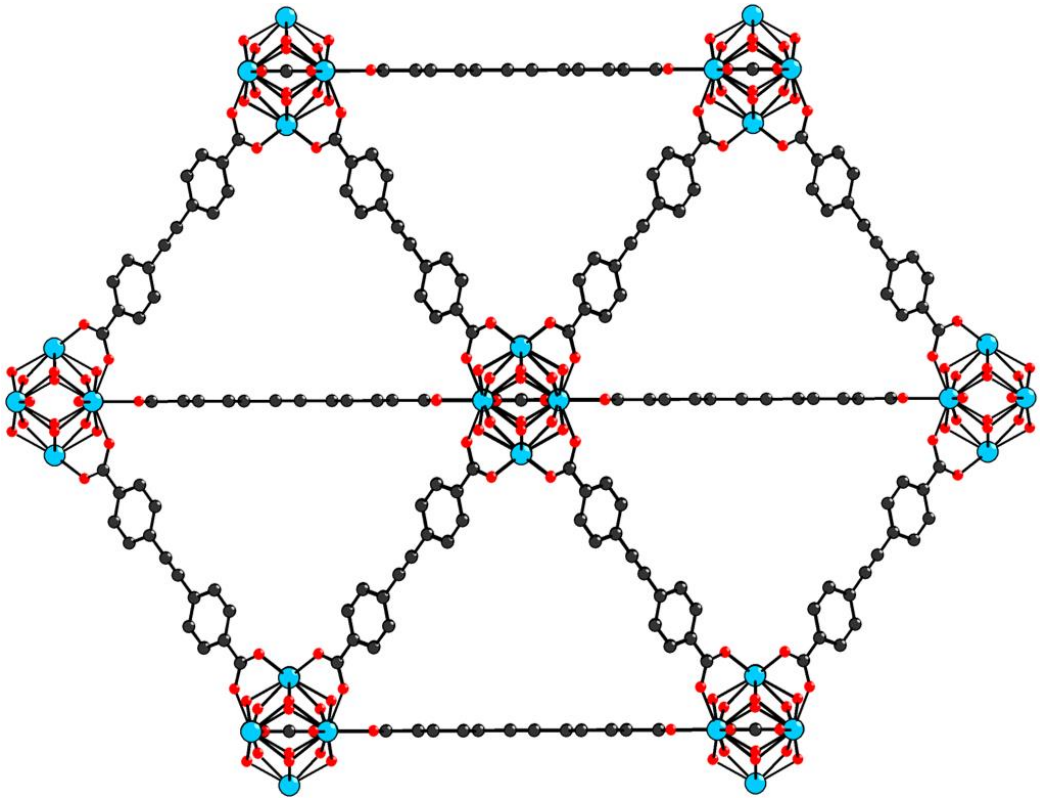

Figure 6.8: Unit cell of UiO-edb as determined by X-ray crystallography, viewed down the *a*-axis. Colour scheme as above. H-atoms omitted for clarity.

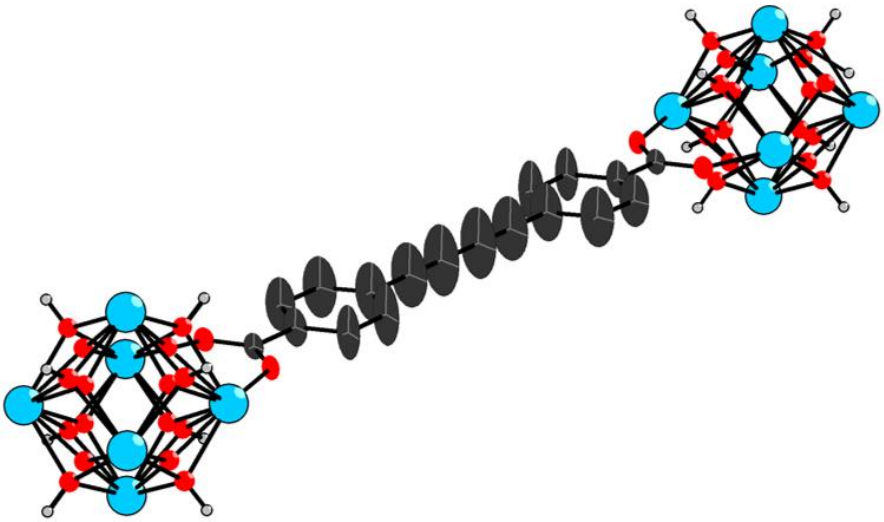

Figure 6.9: Main connectivity of UiO-bddb as determined by X-ray crystallography, showing the hydroxide/oxide disorder on the $Zr_6O_4(OH)_4$ cores and the libration of the bddb linker. Anisotropic displacement parameters shown at 50 % probability. Note the increasing thermal motion on edb on moving away from metal core. Colour scheme as above.

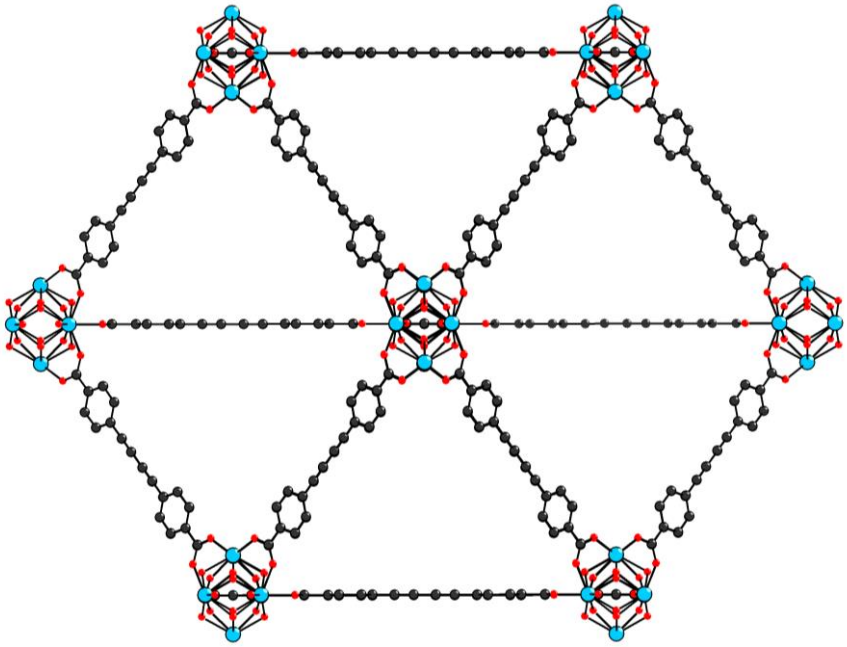

Figure 6.10: Unit cell of UiO-bddb as determined by X-ray crystallography viewed down the *a*-axis. Colour scheme as above. H-atoms omitted for clarity.

6.4.1 Ab initio molecular dynamic studies

Ab initio molecular dynamic (AIMD) simulations were employed to understand the dynamic behavior of the librating and disordered ligands. Firstly, ordered models of the crystal structures were made, which involved removing the disordered components of the ligands and the structures were cast into their primitive setting, where each unit cell contained one metal cluster and six half linkers. Before AIMD simulations were performed, the geometry of each model was then optimised without any symmetry constraints, allowing each half-ligand to optimise independently. For UiO-edb and UiO-bddb the ligands, which were constrained by the *Fm*-3*m* symmetry in the crystal structure, were optimised to configurations where each ligand was no longer constrained by the bisecting mirror planes. As a result, the ligands bowed out of the plane by an average of 0.34(24)° and 9.7(1.7)° for UiO-edb and UiO-bddb, respectively (**Figure 6.11).**

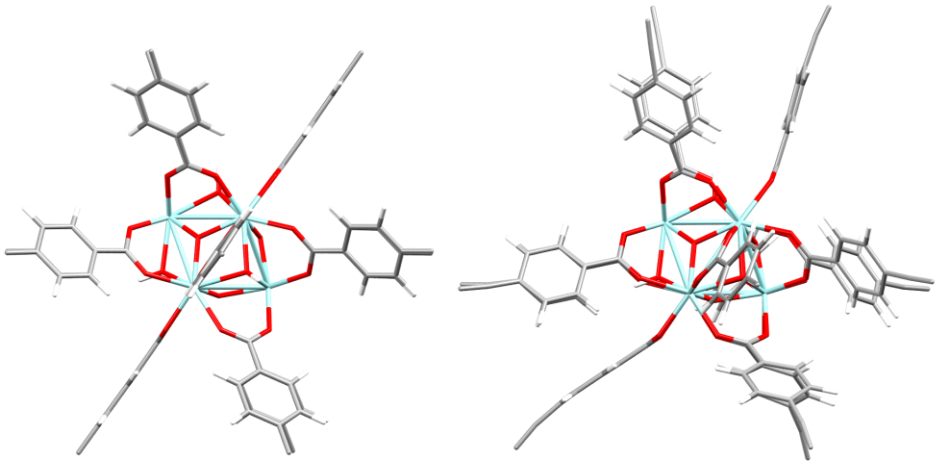

Figure 6.11: Viewed down the *a*-axis, geometry optimised structures of the primitive cell of (left) UiO-edb and (right) UiO-bddb. Note the puckering out of the plane for UiO-bddb.

This result is unsurprising as an alkyne sp hybridised bond is fairly rigid, so UiO-edb would not have the degrees of freedom to deviate much from the plane which the ligand sits on crystallography. However, UiO-bddb is a much longer ligand, and the additional 2 Å in length gives the ligand the degrees of freedom required to deviate from the plane. These deviations for UiO-bddb can be obtained through low energy torsion twisting and the energy difference between the crystal structure and optimised structure is small (0.2 kJ mol^{-1} per unit cell). If it were possible to complete simulations on a larger simulation cell, the average coordinates of a larger sampling of ligands would lie in the plane, which is what is recorded as the time and space average in the crystallographic structure. MOF structures obtained from $ZrO_4(OH)_4$ clusters and ligands longer than bddb, i.e. with the introduction of a phenyl ring between the two alkyne groups, penetration of the framework occurs. These family of frameworks which have been developed by Behrens *et al.* are known as the PIZOFs (Porous Interpenetrated Zirconium-Organic Frameworks). The resulting structures crystallise in space group *Fd*-3*m*, with the same connectivity and structure as UiO Zr-MOFs, however, because PIZOFs have two independent interpenetrating networks they have reduced solvent accessible volumes (SAVs).[24]

Once the AIMD simulations were performed, atomic probability density functions (PDFs), analogous to anisotropic displacement parameters in crystallographic refinements, were derived for the $Zr_6O_4(OH)_4$ core, and each of the six symmetry independent ligand units in each case (**Figure 6.12**), this involves mapping the coordinates of each time step of the NVT ensemble onto the equilibrium structure obtained from the NPT ensemble. The resulting

PDFs clearly demonstrate the extent of ligand movement observed during the simulations.

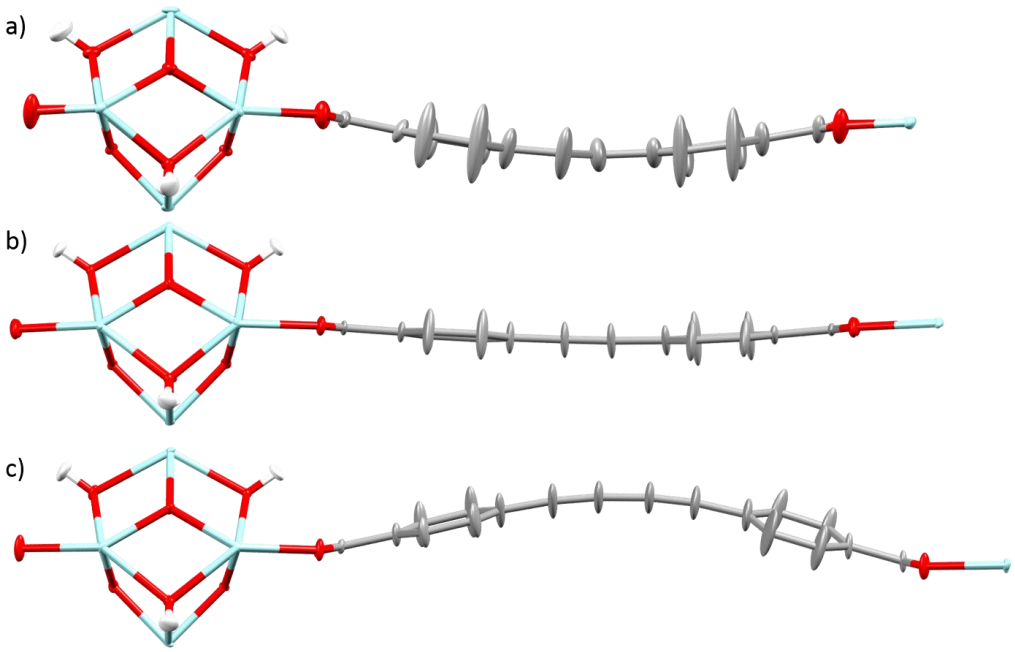

Figure 6.12: Probability density functions of (a) UiO-sdc, (b) UiO-edb and (c) UiO-bddb. Zr – light blue, O- red, C- grey, H- white. H atoms on linker removed for clarity.

In order to define the degree of ligand flexibility observed in the molecular dynamics simulations a 'bowing' angle, θ was defined for each ligand, as defined in **Chapter 5, Section 5.4.2**. Plots showing the variation in θ for each linker for all three frameworks over the course of the NVT ensemble are shown in **Figures 6.13**, **14** and **15**. As in the previous chapter, a mean θ value over the MD trajectory could be derived for each system, with UiO-sdc and UiO-edb having values of 5(3)° and 3(2)° respectively. The sdc ligand is isostructural to abdc (see **Chapter 5**), albeit the N-atoms are replaced with carbon. It is

unsurprising then, to note the θ values for both UiO-abdc and UiO-sdc are identical, both measuring 5(3)°. For UiO-edb, the linker ligand is longer, but due to the rigidity of the alkyne bond between the phenyl rings, it has a θ value that is equivalent to the shorter bpdc ligand in UiO-67, with θ measuring 3(2)° for both UiO-67 and UiO-edb.

For UiO-bddb, the average θ value is 7(2)°, however this does not truly represent the flexibility of the ligand, as unlike for some of the other systems, the bddb ligand never passes through the Zr_4 plane. Instead, the min/max values which were observed during the MD trajectory is a more appropriate quantitative measure of the range of motion the framework possesses. In **Figures 6.13,** 6.**14** and **6.15,** histograms of θ values for each linker are shown, which can be expressed as average values of 16(5)°, 10(2)° and 11(2)° for UiO-sdc, UiO-edb and UiO-bddb, respectively. The shorter, non-linear sdc ligand therefore shows the greatest degree of flexibility, whilst the longer linkers in UiO-bddb show a greater range of oscillation. This could potentially have implications when designing frameworks when mechanical stability of the crystalline material is important, as the UiO-frameworks which demonstrated higher θ values in **Chapter 5** were shown to be more resilient to becoming amorphous on direct compression.

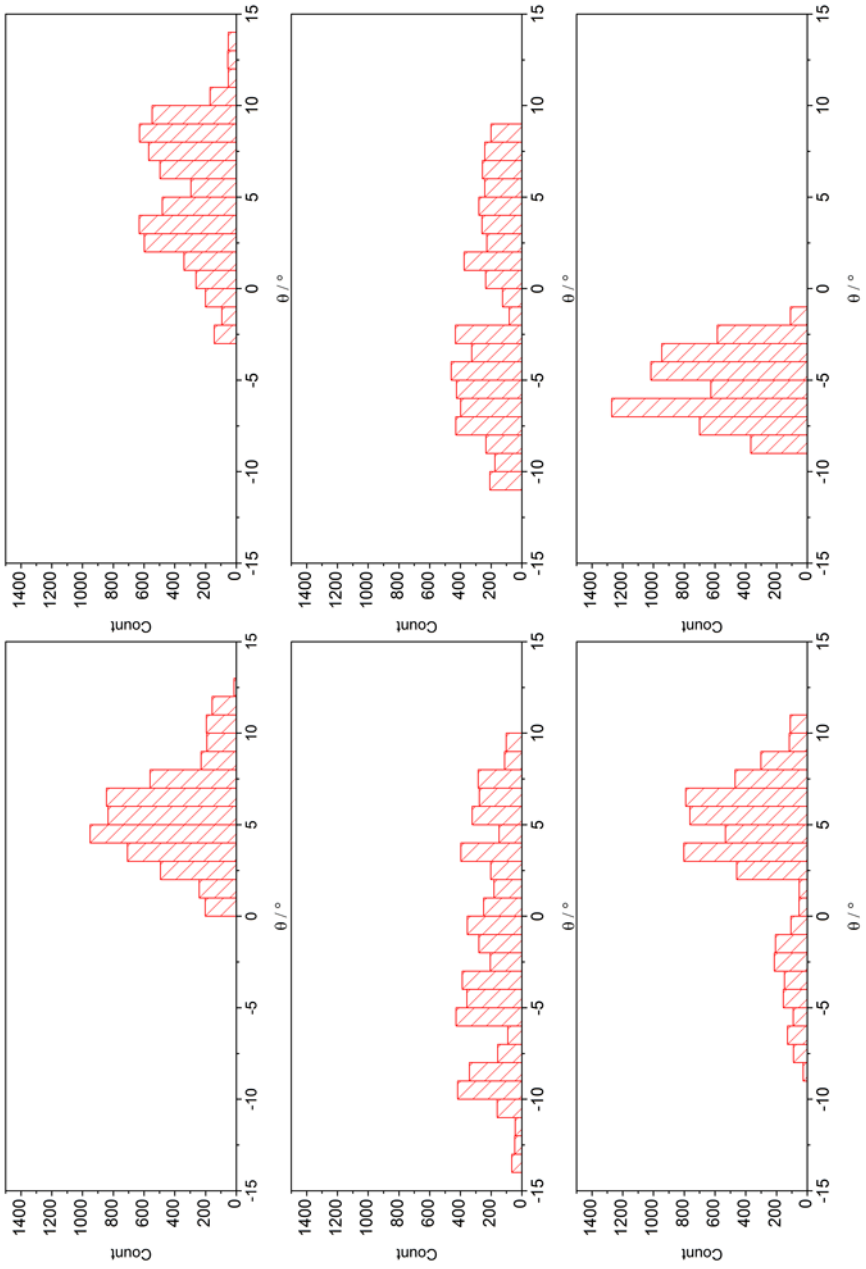

Figure 6.13: Histograms of θ for each of the six independent ligands of UiO-sdc obtained from the NVT AIMD simulations.

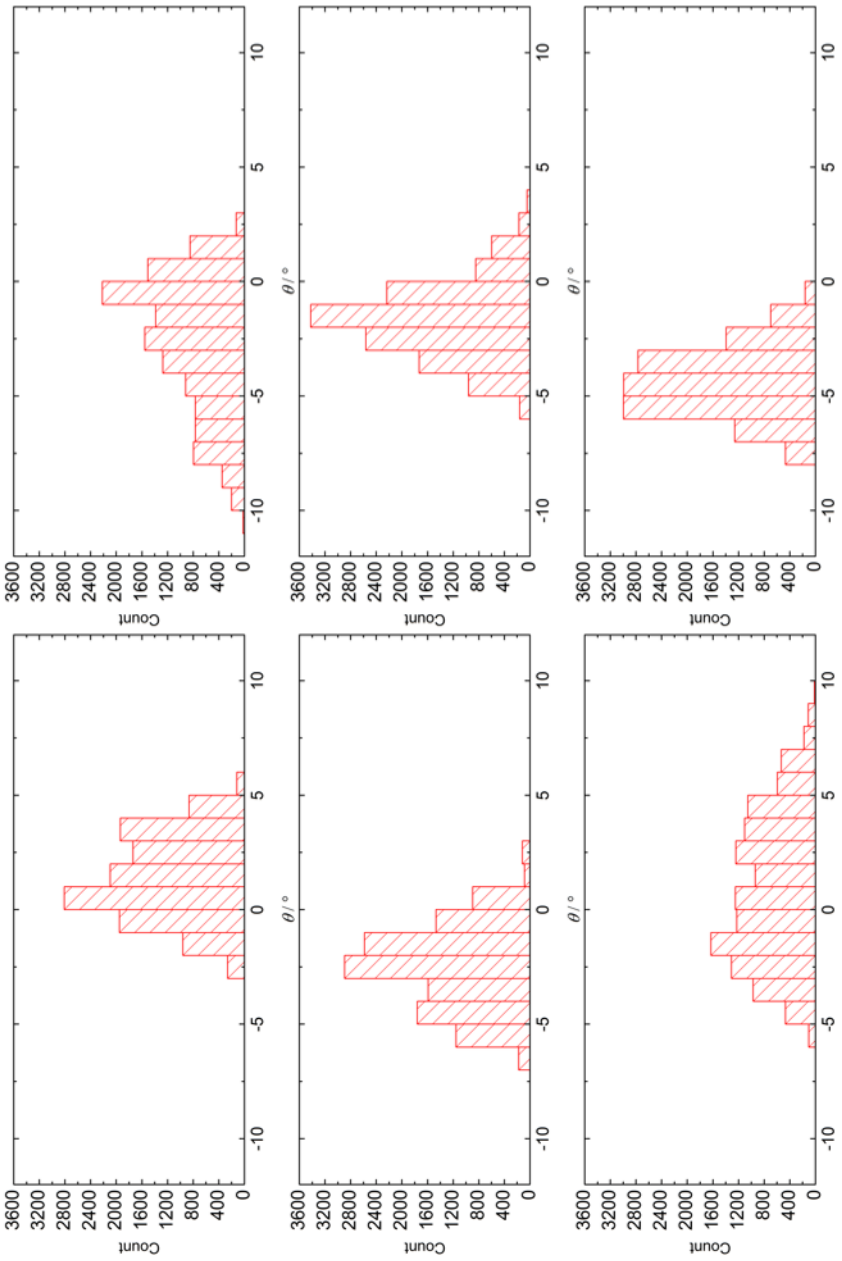

Figure 6.14: Histograms of θ for each of the six symmetry independent linkers in UiO-edb obtained from the NVT AIMD simulations.

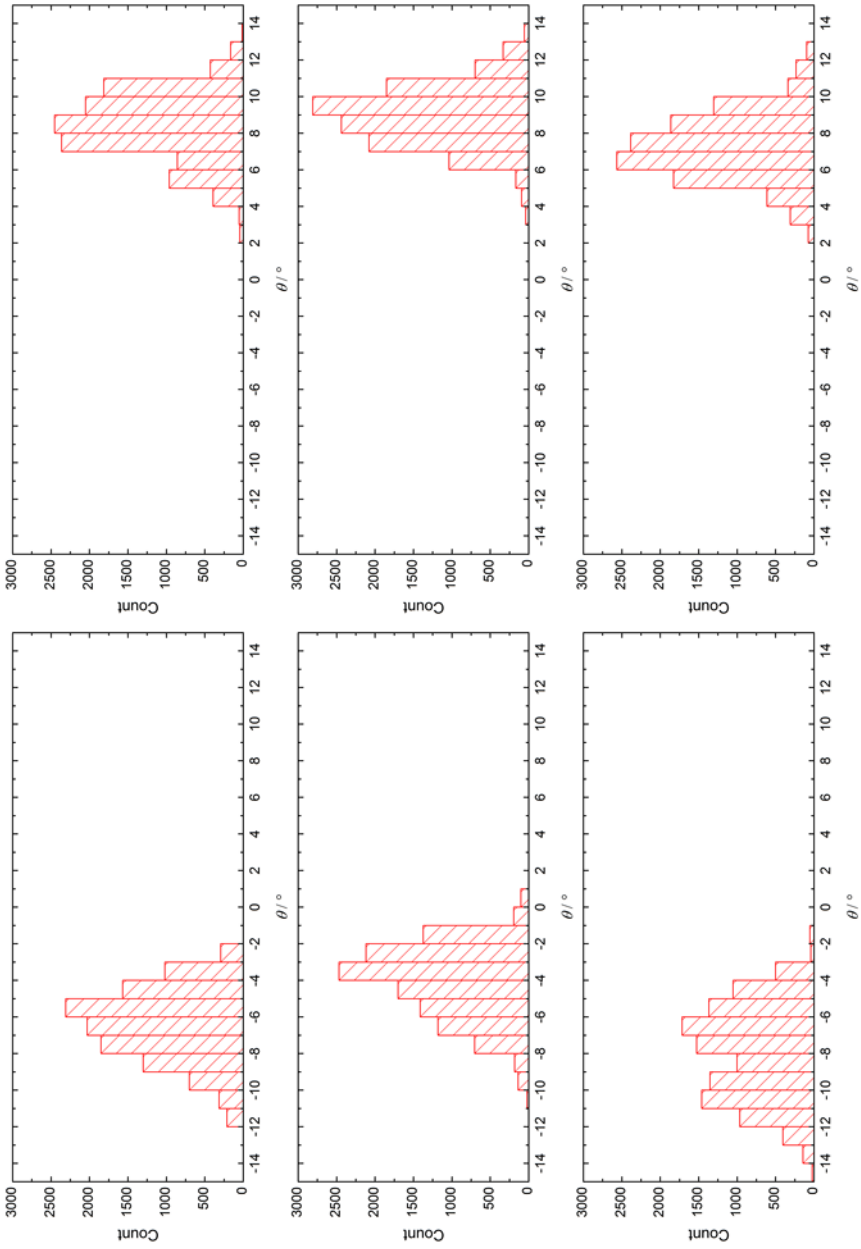

Figure 6.15: Histograms of θ for each the six symmetry independent linkers for UiO-bddb obtained from the NVT AIMD simulations. Note that no linkers pass through the plane (θ =0)

.

6.4.2 DFT-D compression study

In order to determine the compressibility of the frameworks *in silico*, to understand how lengthening linear ligands affects the compressibility of frameworks, the mean atomic position structures obtained from the MD simulations were geometrically optimised by periodic DFT-D calculations. These structures were then used as starting models for simulated hydrostatic compression in 0.2 GPa steps up to a maximum of 0.8 GPa, thereby simulating direct compression experiments on guest-free frameworks. Note the wavefunction was unable to converge after 0.6, 0.8 GPa and 0.2 GPa for UiO-sdc, UiO-edb and UiO-bddb, respectively, an observation which is characteristic of the structure going through a phase transition, and so data are only reported up to these pressures.

The unit cell volumes were observed to decrease by 3.0 %, 4.0 %, and 6.0 % on reaching the maximum pressures of 0.6 GPa, 0.8 GPa and 0.2 GPa for UiO-sdc, UiO-edb and UiO-bddb, respectively. A 2nd order Birch–Murnaghan equation of state allowed the determination of a bulk modulus (K) of 18 GPa for UiO-sdc and 17 GPa for UiO-edb (**Figure 6.16)**. There were too few data points for a bulk modulus determination of UiO-bddb.

K for UiO-sdc was higher than that of the azo analogue, UiO-abdc (c.f. K = 15 GPa); this difference can be attributed to the torsion angle Zr-Zr-O-C, ϕ, (defined in **Chapter Five, section 5.4.4**.) which for UiO-sdc only varied by 2° whereas in UiO-abdc could reach maxima of up to 5 °. In addition, the C-N bond of UiO-abdc compressed more than the C-C bond of UiO-sdc.

The *K* value for UiO-edb of 17 GPa is the first linear UiO-type MOF to have a bulk modulus calculated. *K* of the UiO-67 DFT pressure/volume data described in the previous chapter could not be determined due to a step in the compression curve which may be indicative of an approaching phase change. Experimentally, this structural transition is most likely to be amorphisation of the sample. This step was not observed for UiO-edb, the lack of a step in the compression curve for UiO-edb suggests that by increasing the linker length, the framework has more degrees of freedom to bear the isotropic load compared to the shorter bpdc linker in UiO-67. However, lengthening the linker to bddb had detrimental effects on the isotropic compression. The structure could not be optimised above 0.2 GPa, which suggests a large structural change has taken place to alleviate strain in the system. This is no surprise, as it is the largest MOF (and could therefore be the softest MOF) which has ever been optimised by high-pressure DFT.

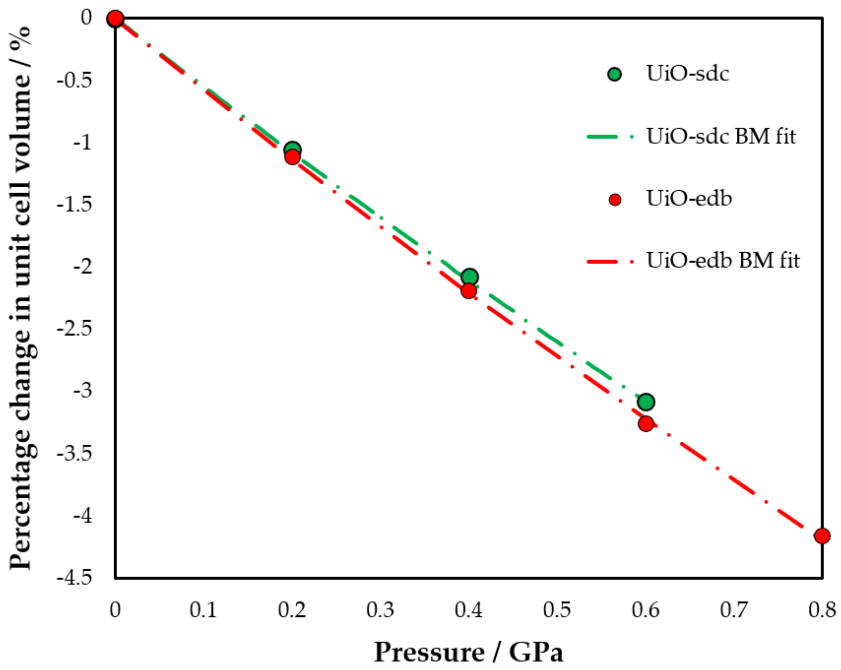

Figure 6.16: Graph of DFT simulated direct compression of UiO-sdc (green points) and UiO-edb (red points) and their respective 2nd order Birch Murnaghan fit shown in green and red dotted dash lines for UiO-sdc and UiO-edb, respectively.

6.4.3 Nanoindentation studies

With the intention of experimentally determining the mechanical response of each of the UiO-frameworks, evacuated single crystals of UiO-sdc, UiO-edb and UiO-bddb were probed by nanoindentation, to determine both their Young's moduli, *E*, and hardness, *H*. Using the load-displacement data gained during the indentation, *E* and *H* were calculated as a function of depth; indents were performed up to a maximum of 500 nm to prevent cracking (**Figure 6.17**).

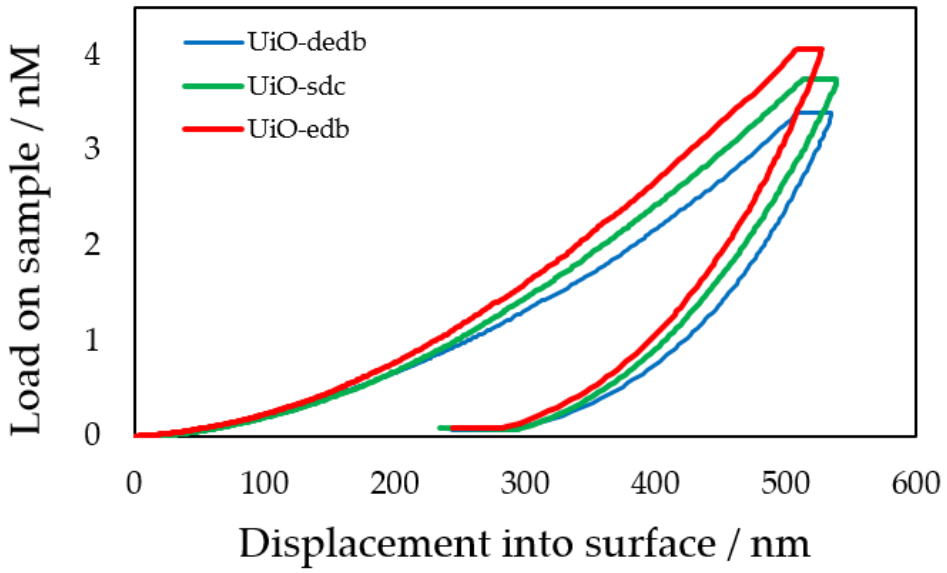

Figure 6.17: Load-displacement data for single crystals of UiO-sdc (red), UiO-edb and UiO- bddb with 17, 16 and 17 indents performed respectively.

The average values for each sample were calculated as *E* = 11.9(3) GPa and *H* = 0.80(1) GPa for UiO-sdc, *E* = 15(1) GPa and *H* = 1.1(1) GPa for UiO-edb and *E* = 13.3(7) GPa and *H* = 0.84(8) GPa for UiO-bddb (**Figure 6.18**). In continuation of the previous chapter, this series of Zr-containing MOFs possess *H* values that are close to the upper limit for those expected for MOFs, where the range of *H* spans over three orders of magnitude from soft materials like MOF-5 with

values of 0.04 GPa (similar to soft organic polymers), to 1.1 GPa for dense MOFs like ZIF-zni.[25]

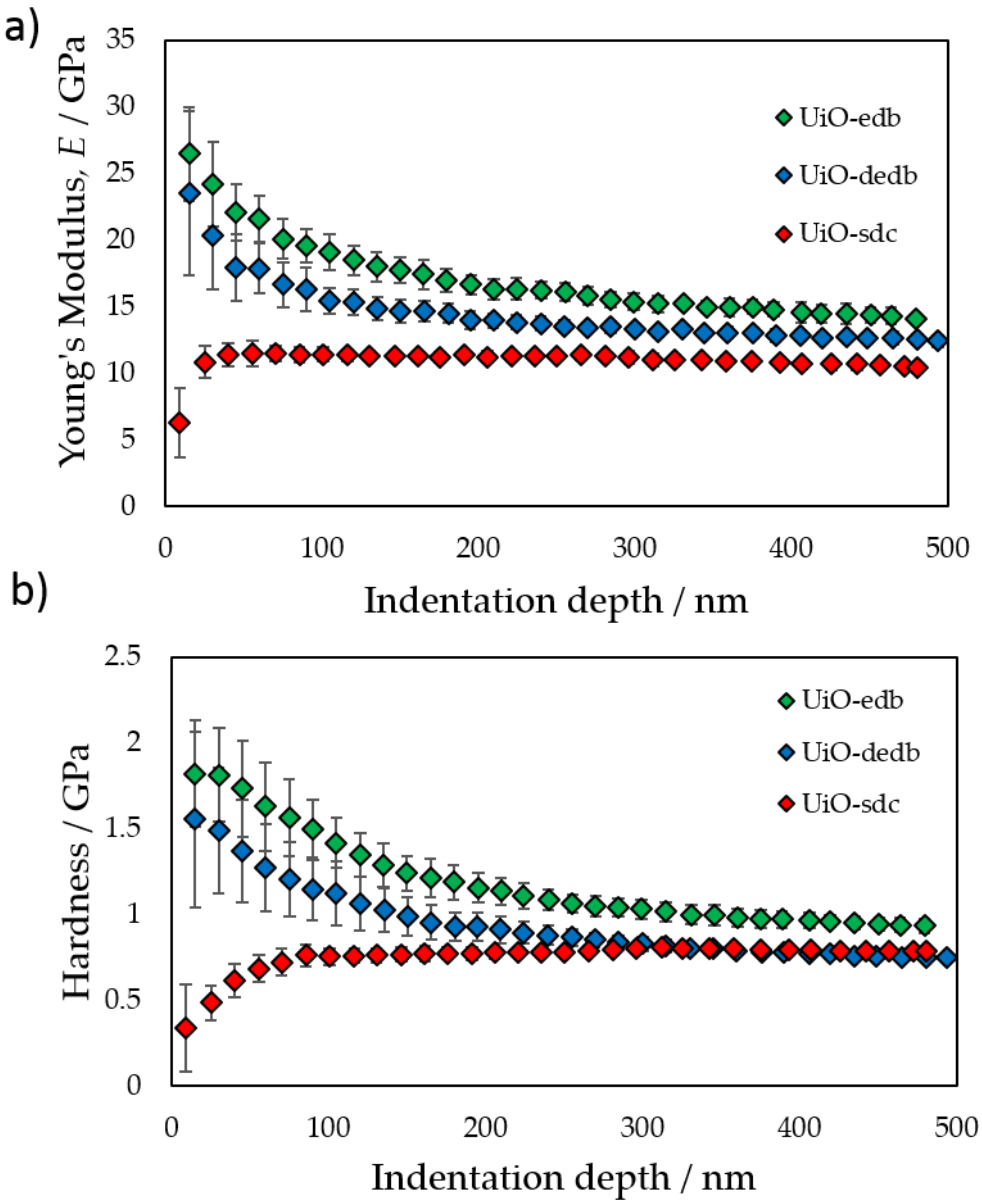

Figure 6.18: (a) Elastic moduli as a function of indentation depth for single crystal samples of UiO-sdc (red), UiO-edb (green) and UiO-bddb (blue). Indented faces were the [111] in all case. Error bars represent the standard deviation of the measurements performed on crystals. b) Hardness values as a function of indentation depth with associated errors as above.

The elastic modulus of UiO-sdc is slightly lower than that of UiO-abdc (*c.f.* E = 13.24 GPa, solvent accessible volume (SAV) = 66.9%). It has been shown previously that there is an empirical inverse relationship observed between E and framework SAV, so because UiO-sdc has a SAV of 64.6%, it would be expected to have a higher E. However, somewhat surprisingly this is not the case, as the experimentally determined E for UiO-sdc is lower. The difference between the two E values of UiO-abdc and UiO-sdc is 3.3σ and is only just statistically significant. This again confirms what was seen in the direct compression study, where in changing from an azobenzene to a stilbene linker the mechanical properties are not drastically changed.

In contrast, the elastic moduli of UiO-edb and UiO-bddb do follow the empirical inverse relationship between SAV (increased linker length) and E,[25] where upon increasing the length of the original sp^2 hybridised ligand bpdc, to edb and further to bddb, E decreases in a linear fashion. UiO-67 is the smallest MOF in the series with a bpdc ligand, with a corresponding SAV = 66.1 % and E =20.0(6) GPa; upon increasing the linker to edb and bddb SAV increases to 74.0 % and 77.7 %, respectively, and so E decreases by 12 % and 17.5 %, respectively (**Figure 6.19**).

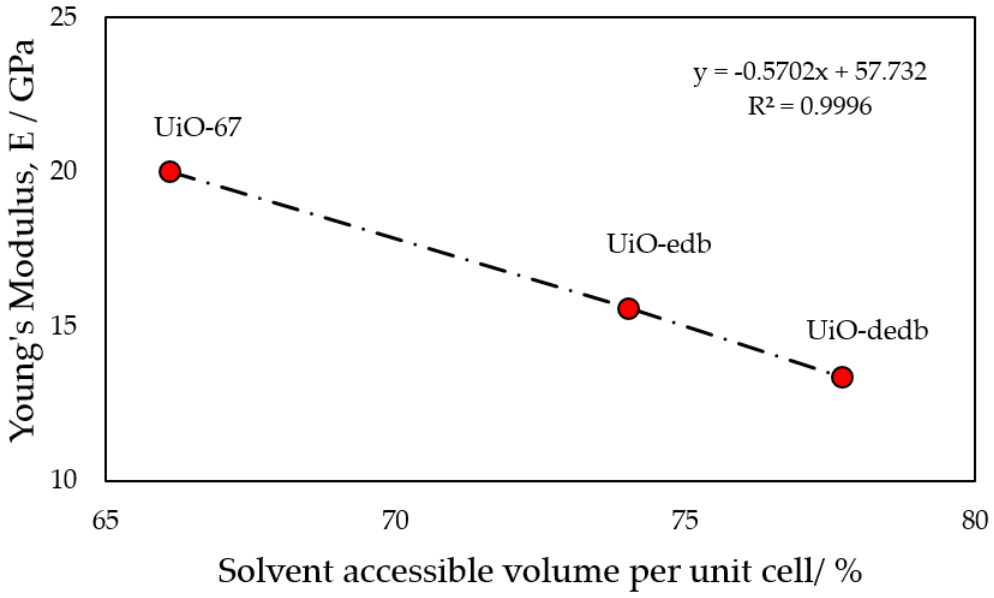

Figure 6.19: Relationship of SAV and *E* of linear linker containing UiO-MOFs

6.5 Conclusions

In summary, the different mechanical behaviour of three UiO-type frameworks, UiO-sdc, UiO-edb and UiO-bddb, have been characterised by computational and experimental methodologies. The calculated bulk modulus of UiO-sdc is in line with the azo analogue, UiO-adbc, demonstrating that non-linear ligands in UiO-MOFs results in an increase in mechanical robustness.[26, 27] The experimentally determined Young's modulus of UiO-sdc lies above those of other highly porous MOFs, such as MOF-5 and ZIF-8 and indeed approaches the mechanical response expected of 'dense' hybrid frameworks, such as lanthanum pyridinedicarboxylate.[28] However, inclusion of the bowed linker, sdc, lowers the *E* value compared to linear analogues such as UiO-edb. A trend in *E* values based on the SAV of linear UiO-type frameworks was clearly demonstrated by UiO-67, UiO-edb and UiO-bddb, and this

understanding of modifying the framework to tune *E* could help with designing new frameworks with specific mechanical responses.

6.6 References

1. R. J. Marshall, S. L. Griffin, C. Wilson and R. S. Forgan, *Chem. Eur. J.*, 2016, **22**, 4870-4877.
2. R. J. Marshall, T. Richards, C. L. Hobday, C. F. Murphie, C. Wilson, S. A. Moggach, T. D. Bennett and R. S. Forgan, *Dalton Trans.*, 2016, **45**, 4132-4135.
3. W. C. Oliver and G. M. Pharr, *J. Mater. Res.*, 2004, **19**, 3-20.
4. J. VandeVondele, M. Krack, F. Mohamed, M. Parrinello, T. Chassaing and J. Hutter, *Comput. Phys. Commun.*, 2005, **167**, 103-128.
5. A. D. Becke, *Phys. Rev. A*, 1988, **38**, 3098-3100.
6. C. T. Lee, W. T. Yang and R. G. Parr, *Phys. Rev. B*, 1988, **37**, 785-789.
7. S. Grimme, J. Antony, S. Ehrlich and H. Krieg, *J. Chem. Phys.*, 2010, **132**.
8. S. Goedecker, M. Teter and J. Hutter, *Phys. Rev. B*, 1996, **54**, 1703-1710.
9. C. Hartwigsen, S. Goedecker and J. Hutter, *Phys. Rev. B*, 1998, **58**, 3641-3662.
10. M. Krack, *Theor. Chem. Acc.*, 2005, **114**, 145-152.
11. J. VandeVondele and J. Hutter, *J. Chem. Phys.*, 2007, **127**, 114105-114110.
12. G. J. Martyna, M. L. Klein and M. Tuckerman, *J. Chem. Phys.*, 1992, **97**, 2635-2643.
13. L. J. Chen, J. P. S. Mowat, D. Fairen-Jienez, C. A. Morrison, S. P. Thompson, P. A. Wright and T. Duren, *J. Am. Chem. Soc.*, 2013, **135**, 15763-15773.
14. M. J. McGrath, J. I. Siepmann, I. F. W. Kuo, C. J. Mundy, J. VandeVondele, J. Hutter, F. Mohamed and M. Krack, *ChemPhysChem*, 2005, **6**, 1894-1901.
15. J. Schmidt, J. VandeVondele, I. F. W. Kuo, D. Sebastiani, J. I. Siepmann, J. Hutter and C. J. Mundy, *J. Phys. Chem. B*, 2009, **113**, 11959-11964.
16. A. M. Reilly, D. A. Wann, C. A. Morrison and D. W. H. Rankin, *Chem. Phys. Lett.*, 2007, **448**, 61-64.
17. A. M. Reilly, S. Habershon, C. A. Morrison and D. W. H. Rankin, *J. Chem. Phys.*, 2010, **132**, 134511-134521.
18. A. M. Reilly, S. Habershon, C. A. Morrison and D. W. H. Rankin, *J. Chem. Phys.*, 2010, **132**, 094502-094512.
19. I. J. Bruno, J. C. Cole, P. R. Edgington, M. Kessler, C. F. Macrae, P. McCabe, J. Pearson and R. Taylor, *Acta Crystallogr. Sect. B-Struct. Sci.*, 2002, **58**, 389-397.
20. S. J. Clark, M. D. Segall, C. J. Pickard, P. J. Hasnip, M. I. J. Probert, K. Refson and M. C. Payne, *Z. Kristallogr.*, 2005, **220**, 567-570.
21. J. P. Perdew, K. Burke and M. Ernzerhof, *Phys Rev Lett*, 1996, **77**, 3865-3868.
22. A. Tkatchenko and M. Scheffler, *Phys. Rev. Lett.*, 2009, **102**, 073005.
23. D. F. Shanno, *Math. Comput.*, 1970, **24**, 647.
24. A. Schaate, P. Roy, T. Preusse, S. J. Lohmeier, A. Godt and P. Behrens, *Chem. Eur. J.*, 2011, **17**, 9320-9325.

25. J. C. Tan and A. K. Cheetham, *Chem. Soc. Rev.*, 2011, **40**, 1059-1080.

26. J. C. Tan, T. D. Bennett and A. K. Cheetham, *Proc. Natl. Acad. Sci. U.S.A.*, 2010, **107**, 9938-9943.

27. C. L. Hobday, R. J. Marshall, C. F. Murphie, J. Sotelo, T. Richards, D. R. Allan, T. Duren, F. X. Coudert, R. S. Forgan, C. A. Morrison, S. A. Moggach and T. D. Bennett, *Angew. Chem. Int. Ed.*, 2016, **55**, 2401-2405.

28. T. D. Bennett, J. C. Tan, S. A. Moggach, R. Galvelis, C. Mellot-Draznieks, B. A. Reisner, A. Thirumurugan, D. R. Allan and A. K. Cheetham, *Chem. Eur. J.*, 2010, **16**, 10684-10690.

-Chapter Seven-

Concluding Remarks and Further Work

Concluding Remarks and Further Work

Looking at the main body of this thesis, the main achievements can be summarised by sub-dividing the successes of each of the experimental chapters.

Chapter Three, involved using a combination of high-pressure crystallography with both DFT and GCMC simulations to understand the gating mechanism of ZIFs upon adsorption. Building on previous work on ZIF-8, this chapter viewed to understand how the functional group on the imidazole ring affected the frameworks response to the incoming guest (methanol). It was found that ZIF-90 behaved in a much similar manner to ZIF-8, rotating to a high-pressure phase which maximised framework-guest interactions. However, ZIF-65, which had a more closed ambient structure was found to rotate in the opposite direction, upon adsorption of methanol, to create a gate-closed structure. The direction of rotation was investigated by GCMC simulations and rationalised by the increased energies of adsorption for the guests. For future work, it would be of interest to investigate what effect the nature of the guest molecules have on rotation of the linkers in high-pressure experiments. For example, if a non-polar solvent, such as pentane, was used as the penetrating pressure transmitting medium, it would be interesting to see how this would affect the adsorption properties of the framework and the gate-opening phenomena.

The work carried out in Chapter Four is an extension of the gate-opening work in the previous chapter, however, instead of using standard pressure transmitting media, small gaseous molecules (O_2, N_2, Ar and CH_4) were

cryogenically loaded within a DAC along with ZIF-8. These types of experiments, whilst standard within geosciences, are a novel way of exploring gas inclusion within microporous materials. One of the advantages of such an approach is the possibility of locating and being able to model accurately adsorption sites that can be hard to find using current gas cell methodologies. In addition it provides a new way of exploring the structural flexibility of MOFs by bringing the possibility of performing high-pressure crystallography with a host of different gases as pressure transmitting media. In addition to the high-pressure experiments, GCMC simulation were applied to understand the gating transition for each gas, and to determine the energy each adsorption site.

The Fifth Chapter involves the study of the mechanical properties of Zr-based MOFs by computational and experimental methodologies, including the evaluation of their hardness, elastic modulus and bulk modulus. By using a range of pressure transmitting media the mechanical robustness of these frameworks could be tested. UiO-67 and UiO-abdc showed near-zero compressibility when solvated with methanol at pressure, however, upon direct compression in FC-70 UiO-67 amorphised at 0.3 GPa and UiO-abdc remained crystalline until 2 GPa and exhibited a 10 % reduction in volume. By using *ab initio* molecular dynamics, the difference in behaviour of these materials could be attributed to the azobenzene linker which was found to bow in and out of the horizontal plane. This discovery could help us to design more mechanically strong MOFs, to help them keep their chemical properties upon shaping into devices, as well as being applied to pressure-coping mechanisms in other MOF systems.

The final chapter provides a more extensive study of the mechanical properties of Zr-based MOFs. In this chapter, the effect of linker length and hybridisation had on the mechanical properties of hardness, elastic modulus and bulk modulus, was studied by *ab initio* molecular dynamics, density functional theory and nano-indentation. The carbon analogue of UiO-abdc, UiO-sdc had both a very similar bulk modulus and elastic modulus, demonstrating that non-linear ligands in UiO-MOFs result in increased mechanical properties. Extending the linker by the inclusion of alkyne and diyne units, a correlation could be drawn between solvent accessible volume and the elastic modulus. The trend shows that upon increasing SAV the elastic modulus linearly decreases. This trend has also been shown in other families of frameworks, for example, ZIFs, but small changes in SAV result in much greater changes in *E.* This understanding of modifying the framework to tune *E* could help with designing new frameworks with specific mechanical responses.

In conclusion, this thesis has involved using a combination of experimental and theoretical methods to understand the adsorption and mechanical properties of metal-organic frameworks. The work has focused on Zn- based frameworks, ZIFs, to fully characterise the response on uptake of different guests and Zr- based frameworks to understand their mechanical response to hydrostatic and uniaxial pressure. The combinatorial method of experiment and theory to fully understand the properties of metal-organic frameworks is something that resonates within this thesis. With further use of these combined methods, the improvement and understanding of adsorption processes within microporous materials will grow.